

Instituto Tecnológico y de Estudios Superiores de Monterrey

Campus Monterrey

School of Engineering and Sciences



Numerical Analysis of Heat and Mass Transfer in Emerging Technologies
of Cooling Systems

A thesis presented by

Enrique Mitz Hernández

Submitted to the
School of Engineering and Sciences
in partial fulfillment of the requirements for the degree of

Master of Science

In

Energetic Engineering

Monterrey Nuevo León, June 15th, 2020

Dedication

To my family.

Acknowledgements

I am deeply grateful with my advisors: PhD. Carlos Rivera and PhD. Miguel Gijon whose guidance and knowledge has been very helpful in the development of this work.

Thank you to my classmates and friends. Thank you for the time spent and the laughs shared. Especially for my friends in CEDES, those days would not be forgotten.

Thank you for all the teachers from which I learned about life, science, and engineering. All the knowledge shared would always be present in my day by day. I am especially thankful with PhD. Ignacio Huertas for receiving me in this journey and been an excellent professor.

Finally, I want to express my grateful with Tecnológico de Monterrey to cover part of my tuition. I will always be in debt with all the administrative staff who enable this process and make it easier. I am special thankful with all the authorities who contribute to my tuition.

Finally, thanks to CONACYT and the support for living received.

Numerical Analysis of Heat and Mass Transfer in Emerging Technologies of Cooling Systems

by

Enrique Mitz Hernández

Abstract

We numerically analyze two distinct technologies for air cooling systems: (1) Dew-Point Evaporative Cooling (DPEC) Systems, and (2) Nanofluids in Helical Coils Heat Exchangers (HCHE). For the first technology, we developed a 1D model with thermophysical properties dependent on the temperature, humidity ratio and atmospheric pressure. The model was evaluated under different conditions in a parametric analysis. Then, a regression maintaining the same atmospheric pressure and channel length was found for the DPEC model. The regression shows a good fit with modeled data, having a RMSE of 1.4 and R^2_{adj} of 93%. Also, the model was evaluated in 4 climates (Very arid, arid, warm, and mild). On the other hand, the Nanofluids in HCHE model was implemented in the commercial software Fluent. The optimal mesh consists of 3.529 Million of elements using a structured mesh. The model implemented was set in a turbulent regime, with thermophysical properties dependent on temperature and constant wall temperature and uniform inlet velocity and temperature. The thermophysical properties for the nanofluids were set from thermophysical properties dependent on the temperature of the base fluid and constant thermophysical properties of the nanoparticle. Then, a case analysis varying the geometry, Dean number, nanofluid (base fluid and nanoparticle) and nanoparticle volume concentration was developed. Finally, from the data modeled we found a correlation for Nusselt number of the Water / Alumina nanofluid.

List of Figures

Figure 1. World energy consumption from 1965 to 2018 (BP, 2019).....	11
Figure 2. Mexico energy consumption matrix (SENER, 2018).	12
Figure 3. Mexico and World relative energy consumption (BP, 2019; SENER, 2018).	13
Figure 4. Electricity generation in Mexico by primary fuel (SENER, 2020).....	14
Figure 5. Total electricity consumption and relative by sector (SENER, 2020).....	15
Figure 6. Emission Factor of indirect GHG emissions by the electricity consumption.	16
Figure 7. Diagrams of conventional cooling systems: a) mechanical equipment of a vapor compression (VC) (conventional) system; b) simple LiBr absorption cycle, to the left of the dashed line, the system represent the VC cycle (Kreider et al., 2010).	18
Figure 8. Strategies to improve energy efficiency in HVAC systems (Vakiloroaya et al., 2014).	19
Figure 9. Energy savings, development status and geographic applicability of non-vapor compression technologies.	20
Figure 10. Main evaporative cooling cycles.....	22
Figure 11. Helical coordinate system (Germano, 1982; C. Y. Wang, 1981).	23
Figure 12. General methodology to assess each technology. The correlation process does not apply for the DPEC model.	37
Figure 13. Components of the model definition which are considered in Validation and Simulations processes.....	38
Figure 14. (a) Perspective view of the DPEC device and view of three stacked channel pairs for showing counter-flow, (b) schematic view of the DPEC device and psychrometric chart process. Twb and DP represent the wet-bulb temperature and dewpoint temperature of inlet air (Pakari & Ghani, 2019).	41
Figure 15. Schematic of a cross-section of the DPEC system.	42
Figure 16. Physical DPEC model.	43
Figure 17. Schematic of differential volume of the control volume.	44
Figure 18. Map of main climates (García, 1998) in México and the location of met stations.	52
Figure 19. Helical coil physical model.	55
Figure 20. Geometries studied in different studies (Aly, 2014; Bizhaem & Abbassi, 2017; Jamshidi et al., 2012; Kahani et al., 2013a; Pawar & Sunnapwar, 2014; Wu et al., 2013; Zonouzi et al., 2014).	62
Figure 21. Mesh independency results for the outlet temperature using the Model 2.	65
Figure 22. Comparison of outlet temperature of numerical models with experimental data (exp) and numerical model (num) from Pakari & Ghani (2019). a) Developed models (T_{M1} and T_{M2}) and numerical model against experimental data. b) Developed numerical models (T_{M1} and T_{M2}) against numerical reference model.	66
Figure 23. Coefficient of determination (R^2), RMSE and slope of the linear regression of numerical models with experimental data and numerical reference model.	67

Figure 24. Resulting parameters with a variation the setting variables to modify. Right charts, series 1, show the parameters: outlet temperature (T_{out}), wet-bulb effectiveness (ϵ_{wb}) and dew-point effectiveness (ϵ_{DP}). Left charts, series 2, show the parameters: conditioning cooling capacity (Q_{ref}) and environmental cooling capacity (Q_{cool}). In each row formed by two charts, the variables modified are: 1) inlet airflow, 2) extraction ratio, 3) inlet temperature, 4) channel length, 5) inlet relative humidity and 6) atmospheric pressure. Base values of the runs presented were: $md = 0.15$ CFM, $ER = 0.33$, $T_{in} = 30$ °C, $L = 0.5$ m, $RH = 50\%$, $P = 100$ kPa.

.....	69
Figure 25. Conditioning cooling capacity versus inlet airflow for different channel lengths for inlet conditions $T_{in} = 30^{\circ}\text{C}$ and $RH = 50\%$	72
Figure 26. Optimal airflows in function of wet-bulb temperature for different channel lengths.....	73
Figure 27. Maximum wet-bulb temperature for the devices studied.	74
Figure 28. Regressions found to estimate the outlet temperature.	75
Figure 29. Parameters of the regressions found.	76
Figure 30. Ambient (inlet) temperature and outlet temperature of the DPEC system simulated. $T_{ref} = 25^{\circ}\text{C}$	77
Figure 31. Sum of hourly necessary cooling capacity to reach the reference temperature ($Q_{cool}-Q_{ref}$) when cooling is needed ($T_{amb} > 25^{\circ}\text{C}$) and mean ambient temperature for each city per month.....	77
Figure 32. Sum of hourly environmental cooling capacity (Q_{cool}) provided by the system when cooling is needed ($T_{amb} > 25^{\circ}\text{C}$) and mean outlet temperature for each city per month.	78
Figure 33. Sum of hourly conditioning cooling capacity (Q_{ref}) provided by the system when cooling is needed ($T_{amb} > 25^{\circ}\text{C}$) and relative humidity for each city per month.	78
Figure 34. Sum of annual cooling capacities for each city.....	79
Figure 35. Mesh sizing controls used to create the different structured meshes. ...	82
Figure 36. Relative differences of the meshes compared to the immediate coarser mesh.	83
Figure 37. Calculated error parameters of the mesh with the immediate coarser mesh,	84
Figure 38. Validation of the convective heat transfer coefficient with experimental and numerical values (Rakhsha et al., 2015).	85
Figure 39. Validation of the pressure drop with experimental and numerical values (Rakhsha et al., 2015).	85
Figure 40. Contours of dimensionless temperature and velocity at different axial positions. $T_w = 370$ K, $T_{in} = 300$ K, $Re = 32.5$ k.....	86
Figure 41. Contours of kinetic energy at different axial positions. $T_w = 370$ K, $T_{in} = 300$ K, $Re = 32.5$ k.	87
Figure 42. Average Nusselt number for the seven geometries. The nanofluid is the same: $\text{H}_2\text{O}/\text{Al}_2\text{O}_3$, $\alpha = 1\%$	88
Figure 43. Nusselt number for 9 different Nanofluids.	89
Figure 44. Nusselt number for a variation in Dean number.	89
Figure 45. Nusselt number for a variation of nanoparticle concentration.....	90

Figure 46. Correlation for Water / Alumina.	91
Figure 47. General correlation found for the nanofluids studied.	92
Figure 48. Coefficients and exponents of the correlations (66), (67) and (68).	92
Figure 49. Structure of the code developed for the DPEC model.	103

List of Tables

Table 1. Statistical indicators of fuels evolution in electricity generation in Mexico.	14
Table 2. Estimation of relative consumption by air-cooling.	16
Table 3. Research topics investigated.	20
Table 4. Dimensions of the physical model.	43
Table 5. Assumption for the two DPEC models developed.	45
Table 6. Differential analysis for DPEC model.	45
Table 7. Governing equations for the DPEC model.	47
Table 8. Boundary conditions for the DPEC model.	48
Table 9. Thermophysical properties of air in the two DPEC models developed. ...	49
Table 10. Base values and range of the different values for the parametric analysis.	50
Table 11. Cities (stations) characteristics.	52
Table 12. Assumptions made in Nanofluid model.	55
Table 13. Boundary conditions for the Nanofluid model.	58
Table 14. Coefficients of equation (47) for thermophysical properties of base fluids.	59
Table 15. Nanoparticles thermophysical properties.	59
Table 16. Values and input values for equation (50).	60
Table 17. Coefficients of equation (47) for thermophysical properties of Water/Alumina at 1% vc.	60
Table 18. Different values for each variable for the case analysis.	61
Table 19. Dimensions of the seven geometries studied.	61
Table 20. Summary of different values used in simulations.	63
Table 21. Validation values from experimental work (Pakari & Ghani, 2019).	64
Table 22. Summary of relationships between input variables and parameters from the parametric analysis.	71
Table 23. Mesh sizing controls used in the mesh independency analysis.	82

Contents

Abstract.....	1
List of Figures	2
List of Tables.....	4
Acronyms and abbreviations	7
Nomenclature: Variables and Greek Letters.....	8
Subscripts.....	9
Chapter 1 Introduction	10
1.1 Background	10
1.2 HVAC systems description	17
1.2.1 Conventional systems	17
1.2.2 Strategies for HVAC energy saving	18
1.2.3 Technologies investigated	21
1.2.4 Computation Fluid Dynamics.....	23
1.3 Problem definition.....	24
1.4 Literature review	24
1.4.1 Dew-Point Evaporative Cooling	24
1.4.2 Nanofluids and helical coils	28
1.4.3 Remarks	35
1.5 Objective	36
1.5.1 Specific objectives	36
1.6 Scope research	37
1.7 Methodology description.....	37
1.8 Thesis structure	39
Chapter 2 DPEC model	41
2.1 Model description	41
2.1.1 Physical model	42
2.1.2 Assumptions	44
2.1.3 Mathematical model	45
2.2 Analysis description.....	50
2.2.1 Parametric analysis	50
2.2.2 Cases of study.....	51
Chapter 3 Nanofluids model	54

3.1	Model description	54
3.1.1	Physical model	54
3.1.2	Assumptions	55
3.1.3	Mathematical model	56
3.2	Case analysis description	60
Chapter 4	Results analysis	64
4.1	DPEC model.....	64
4.1.1	Mesh independency	65
4.1.2	Validation.....	65
4.1.3	Parametric analysis	67
4.1.4	Model performance for different climates	76
4.2	Nanofluids in helical coils	81
4.2.1	Mesh independency	81
4.2.2	Validation.....	84
4.2.3	Qualitative analysis.....	86
4.2.4	Case analysis	87
4.2.5	Correlation by nanofluids	90
Chapter 5	Conclusions	93
5.1	DPEC Model.....	93
5.2	Nanofluids in helical coils	93
5.3	Future work	94
5.3.1	DPEC systems	94
5.3.2	Nanofluids in helical coils.....	94
Appendix A	– Humid air thermophysical properties	95
Appendix B	– Dimensionless analysis	97
	DPEC model.....	97
	Nanofluids model.....	98
Appendix C	– Coefficients for nanofluid thermophysical properties	101
Appendix D	– DPEC model codes	103
Bibliography	107

Acronyms and abbreviations

1D,2D,3D	One dimension, two dimensions and three dimensions
AC	Air Conditioning
AC	Amorphous Carbonic
Al ₂ O ₃	Alumina (chemical formula)
ANSYS	Engineering Simulation and 3D Design (software package) or ANSYS, Inc. (company)
ASHRAE	American Society of Heating, Refrigerating and Air-Conditioning Engineers
BARC	Bhabha Atomic Research Centre in Bombay
BP	British Petroleum (company)
CEPAL	<i>From the spanish</i> , Comisión Económica para América Latina y el Caribe
CFD	Computational Fluid Dynamics
CFE	<i>From the spanish</i> , Comisión Federal de Electricidad
COMSOL	COMSOL Multiphysics® (software)
CuO	Cupric oxide or Copper (II) oxide (chemical formula)
DEC	Direct Evaporative Cooling
DOE	Department of Energy (from US)
DPEC	Dew-Point Evaporative Cooling
EF	Emission Factor
EWT	Enhanced Wall Treatment
FD	Finite Differences
FEM	Finite Element Method
FM	Finite Methods (FDM, FEM, FVM)
FVM	Finite Volume Method
GDP	Gross Domestic Product
GHG	Greenhouse Gas
H ₂ O	Water (chemical formula)
HC	Helical Coil
HCHE	Heat Exchanger Helical Coil
HCTHE	Helical Coiled Tube Heat Exchanger
HVAC	Heating, Ventilation and Air Conditioning
IEC	Indirect Evaporative Cooling
IEI	<i>From Spanish</i> , Ingeniería Energética Integral
IPY	Increments per Year
MAE	Mean Average Error
M-Cycle	Masiotsenko Cycle
MAE	Mean Absolute Error
MARE	Mean Absolute Relative Error
MWCNT	Multi-Walled Carbon Nanotubes
NF	Nanofluids
NTU	Number of Transfer Units

ODE	Ordinary Differential Equation
OHTC	Overall Heat Transfer Coefficient
PD	Pressure Drop
R&D	Research and Development
R^2	Term for Pearson coefficient
REC	Regenerative Evaporative Cooling
RENE	<i>From the spanish</i> , Registro Nacional de Emisiones
RMSE	Root Mean Squared Error
RIPY	Relative Increments per Year
RSD	Relative Standard Deviation
SA	Sodium Alginate
SCMC	Sodium Carboxymethyl Cellulose
SD	Standard Deviation
SEMARNAT	<i>From the spanish</i> , Secretaría de Medio Ambiente y Recursos Naturales
SENER	<i>From the spanish</i> , Secretaría de Energía
St.	Straight
tCO ₂ eq	Tons of carbon dioxide equivalent (units)
TiO ₂	Titanium dioxide (chemical formula)
US	United States (country)
VC	Vapor Compression
ZnO	Zinc oxide (chemical formula)

Nomenclature: Variables and Greek Letters

α	Volume concentration (-)
Br	Brinkman number
c_p	Specific heat, J kg ⁻¹ K ⁻¹
D	Binary diffusion coefficient, m ² s ⁻¹
dn,dr,ds	Mesh control parameters
De	Dean number
D _t	Tube diameter, m
D _c	Coil diameter, m
d _f	Equivalent diameter of a fluid molecule
d _p	Diameter nanoparticle (m)
f	Friction factor
g	Gravity, 9.806 m s ⁻²
h	Heat transfer coefficient, W m ⁻² K ⁻¹ , or Mass transfer coefficient, m s ⁻¹
H	Channel height, m
h _{fg}	Latent heat of vaporization of water, J kg ⁻¹
h _m	Mass transfer coefficient, m s ⁻¹
I	Turbulence intensity

k	Kinetic energy, $\text{m}^2 \text{s}^{-2}$
m	Mass flow rate, kg s^{-1}
M	Molar mass, kg mol^{-1}
N	Avogadro Number, $6.022 \times 10^{23} \text{ mol}^{-1}$
Nu	Nusselt number
P	Pressure, Pa
P_c	Pitch coil, m
Pr	Prandtl number
R	Universal Gas Constant, $8.314472 \text{ J mol}^{-1} \text{ K}^{-1}$
Re	Reynolds number
Sh	Sherwood number
T	Temperature, K or $^{\circ}\text{C}$
U	Overall heat transfer, $\text{W m}^{-2} \text{ K}^{-1}$
u	Velocity vector (x-direction), m s^{-1}
W	Heat Exchanger Width, m
w	width channel, m
x,y,z	Cartesian coordinates
δ	Curvature ratio
ε	Turbulent dissipation rate, $\text{m}^2 \text{s}^{-3}$
ε	Effectiveness
λ	Dimensionless pitch
μ	Viscosity, Pa s
φ	Thermophysical properties
ρ	Density, kg m^{-3}
θ	Thermal conductivity, $\text{W m}^{-1} \text{ K}^{-1}$

Subscripts

a	air	np	Nanoparticle
atm	Atmospheric	out	Outlet
b	bulk	p	Plate
CS	Cross section	R	Regression
d	Dry-channel	v	Vapor
g	Saturated vapor	w	Wet channel / water
in	Inlet	w-a	Water to vapor
m	Mixture air-vapor	wb	Wet bulb
n	Normal	wf	Water film
nf	Nanofluids		

Chapter 1 Introduction

Life and energy are two concepts which define the world nature. Both are strongly related one towards each other. So, as a first approach to study the relation of life and energy, we start to define each one. Regarding the first term, we can define individual life or living being as “*any autonomous system with open-ended evolutionary capacities*” (Anisimov et al., 2014)(Ruiz-Mirazo et al., 2010). In regard to the second term, we can define energy¹, from the mechanical approach, as the ability to do work (Doménech et al., 2007). In an attempt to relate both terms in a brief and exact definition, we quote the definition of living systems² stated by Miller in 1975: “*living systems exist in space and are made of matter and energy organized by information*” (Miller, 1975). So, from a broader perspective life and energy are intrinsically related and have a codependent relation. Thereby, this general and integral relation could be analyzed as from many angles as a circle can divide. In this study, we will analyze two new technologies which improve the efficiency on the energy consumption to provide air cooling for humans (living system).

1.1 Background

Despite the intrinsic relation between human life and energy from a broader perspective. The implications between this relation have arising a major environmental concern due to the need of fossil fuels combustion to provide energy for human purposes (Barbir et al., 1990). These world widespread environmental issues has been compiled into one concept known as “climate change” (Lu et al., 2017). If we look for the origins on this environmental concern, we could find different origins in the world. By means of the economical perspective, public concern is mainly driven by local environmental problems and healthy risks in poorer countries; and a seek for maintain and improve life quality in richer countries (Diekmann & Franzen, 2019). Regardless of the environmental concern of the general public population, governments are aware of the importance of energy due to its direct proportional relation with gross domestic product³ (GDP) as a means of economic development in countries (Burke & Cserekyei, 2016).

Consequently, we have reached an important conflict in the consumption of energy for human beings: its directly proportional relation with GDP (economic development) and the environmental issues related to the combustion of fossil fuels. Which are the foremost fuels to provide heat or electricity (BP, 2019). Nevertheless, energy implications do not stop here. We must consider that the neediness of energy

¹ Energy definition is a very interesting topic in education science due to its implications in other sciences and how concepts and theories evolved (Doménech et al., 2007).

² There exist 7 living systems according to Miller: cell, organ, organism, group, organization, society and supranational (Miller, 1975).

³ This relationship between energy and GDP has taken the name of *energy elasticity* which is the percentage of change in energy use associated with a 1% change in GDP. In Mexico, the energy elasticity is 1 ($R^2=1$) with data from 2009 to 2018 (SENER, 2020).

is continuously growing, and it is pushed by two key growing factors: population and per capita energy use (Holdren, 1991).

Growing of population and per capita energy use have pushed humans to group in cities, a process known as urbanization. In spite of the alterations of cities to the natural environment, cities are an important center of energy consumption, representing approximate 80% of the greenhouse gas (GHG) emissions (Heymans et al., 2019). Also, buildings, after the industrial revolution, have become the icon of modernity, prosperity and development in cities (Mir M & Aksamija, 2008) and the growth on the construction of buildings implies more energy consumed. For example, energy consumption in buildings grew approximately 6 exajoules (EJ) from 117 EJ in 2010 to 123 EJ in 2016 (UN Environment and International Energy Agency, 2017).

Currently, world energy consumption is predominantly generated by the combustion of fossil fuels as coal (27.2%), oil (33.6%) and natural gas (23.9%) for a total share of 84.7% of the total world energy consumption from fossil fuels in 2018 (BP, 2019). The total amount of energy consumed in 2018 was 13,865 Mtoe which has been triplicated in 49 years as can be seen in Figure 1. It is worth to observe that the growth has being practically steady from the begin of the data set (BP, 2019) until nowadays.

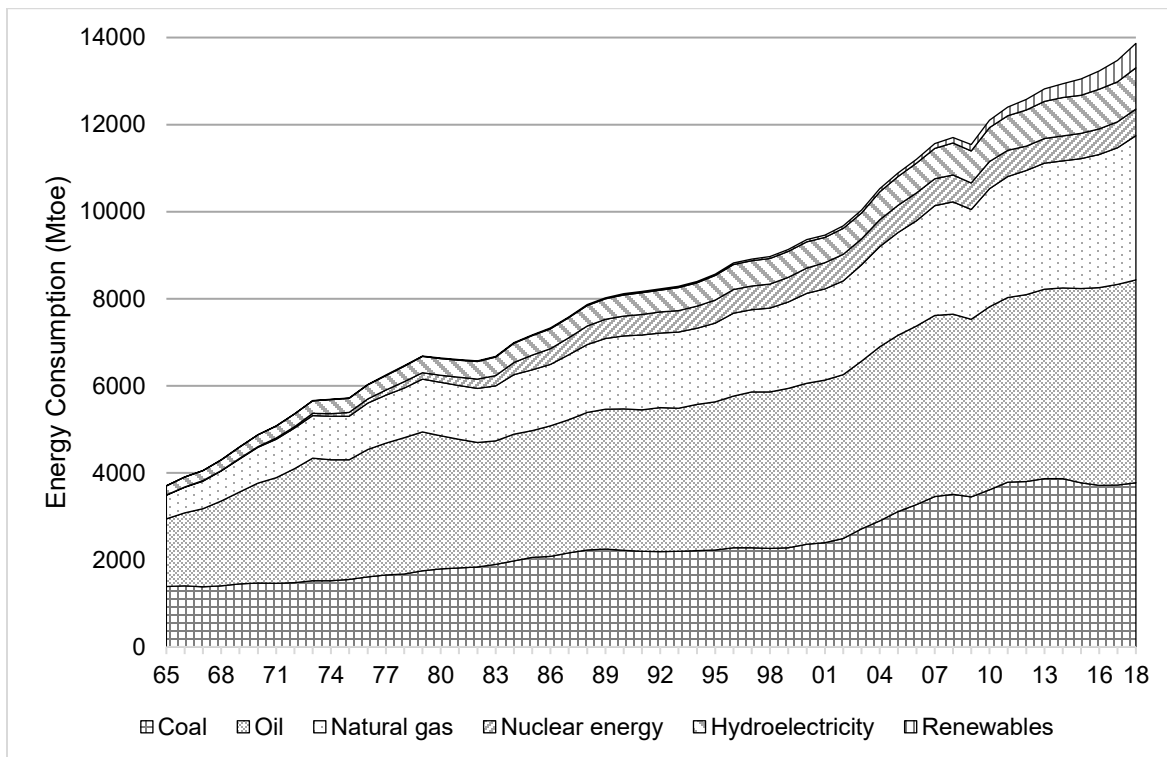


Figure 1. World energy consumption from 1965 to 2018 (BP, 2019).

In the case of Mexico, we have a different energy matrix than the rest of the world (see Figure 2). Energy consumption has been growing in a rate of 1.876 Mtoe per year from 1990 until 2018 ($R^2=0.97$). However, the increase per year has not been regular and had a maximum of 6.7% (in 2002), a minimum of -5.2% (in 2009) and an average of 1.83% of variation in the range of the plot shown.

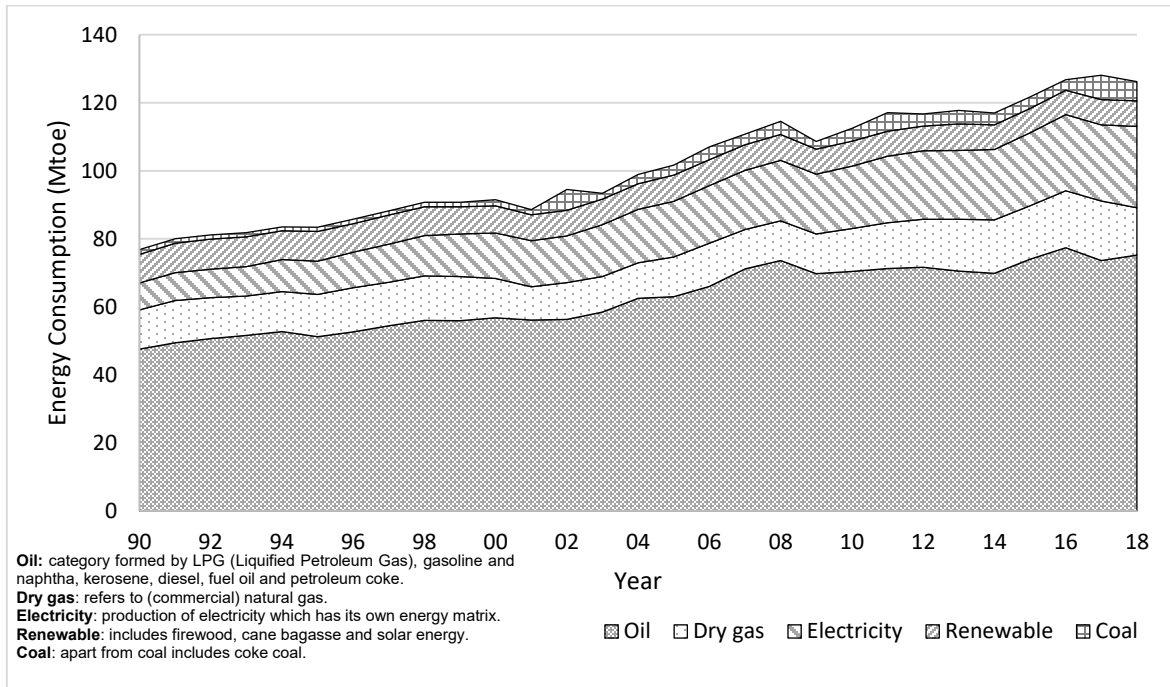


Figure 2. Mexico energy consumption matrix (SENER, 2018).

Also, a comparison of energy matrixes from Mexico with the rest of the world at different years can be seen in Figure 3. Left stacked columns represent Mexico fuels consumption and right stacked columns represent the world fuels consumption for each year. From the data, we observe the high dependency of oil as Mexico principal fuel with 62% in average since 1990 to 2018, and 59.6% in the last year of data (2018). In contrast, the world also has a strong dependency on oil being 37% in average in the same period since 1990 to 2018, and 33.6% in the last year of data (2018). However, the comparison between energy consumptions have a bias due to the different categories for reporting data from BP and SENER. The main difference comes from the definition of Electricity⁴ between datasets. Thereby, by disaggregating data from Mexico's electricity dataset and calculating fossil fuels

⁴ SENER (2018) reports electricity generation independently from the primary fuel (i.e. coal, natural gas, etc.). In contrast, BP (2019) reports hydroelectricity and nuclear energy as different categories. For the comparison made (Figure 3), data of hydroelectricity and nuclear energy categories from BP were compiled into a new Electricity category. The last process was made due to those categories from BP are embedded in the Electricity category from SENER.

share. We observe that in Mexico we consume an average of 89% from fossil fuels while in the world (average) 87% of the energy consumption comes from fossil fuels.

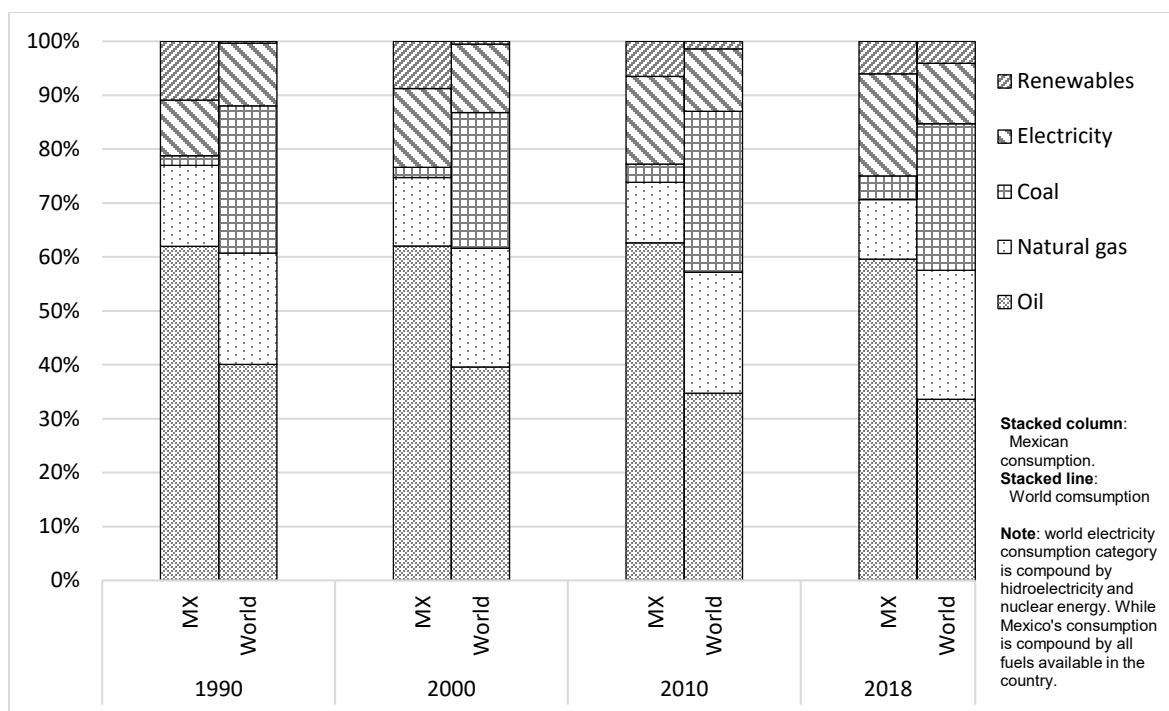


Figure 3. Mexico and World relative energy consumption (BP, 2019; SENER, 2018).

Furthermore, we are interested in electricity as a primary fuel. In this regard, the information reported from CFE (*Comisión Federal de Electricidad*, by its acronym in Spanish) shows a steady increase in power generation of 4.522 TWh per year. The evolution in electricity generation by primary fuel is shown in Figure 4.

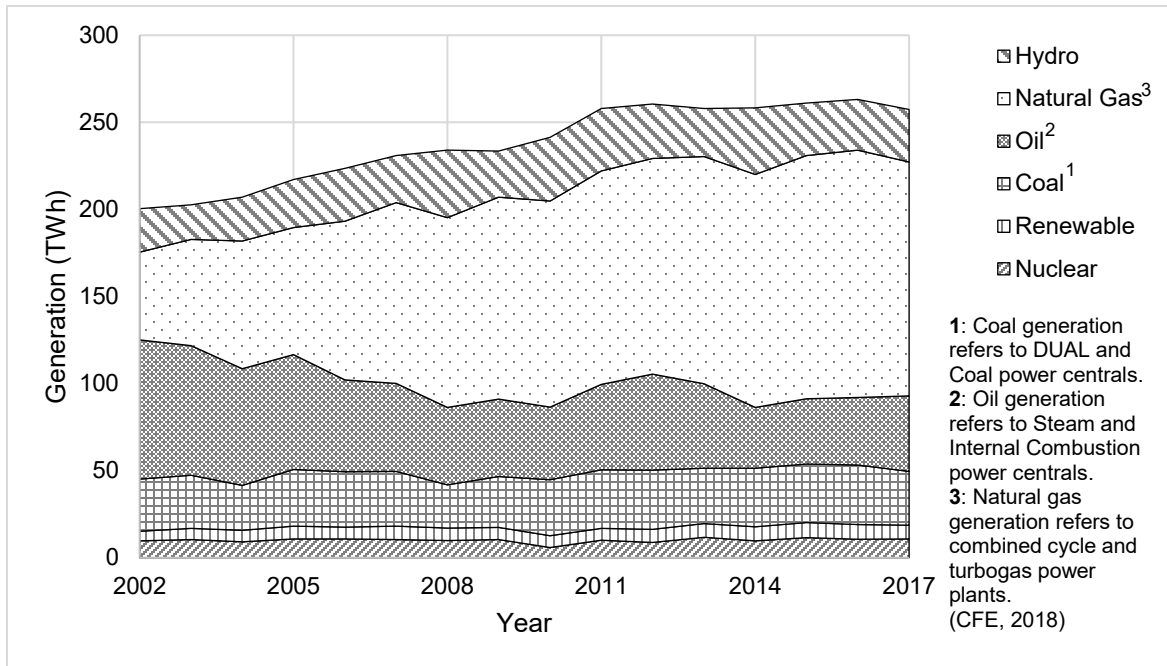


Figure 4. Electricity generation in Mexico by primary fuel (SENER, 2020).

Figure 4 shows different trends by primary fuels along the period of the dataset. From the data, we calculate some indicators to distinguish those trends. The values of the statistical indicators calculated are shown in Table 1.

Table 1. Statistical indicators of fuels evolution in electricity generation in Mexico.

Primary fuel	AVG	SD	RSD	IPY	RIPY	R ²
Nuclear	10.1	1.33	13%	0.042	0.42%	2.1%
Renewable	7.3	0.83	11%	0.151	2.08%	71.1%
Coal	31.2	2.68	9%	0.285	0.91%	23.9%
Oil	51.8	12.99	25%	-2.370	-4.58%	70.7%
Natural Gas	107.7	28.41	26%	5.896	5.48%	91.5%
Hydro	29.9	5.10	17%	0.518	1.73%	21.9%
Total	237.9	21.82	9%	4.522	1.90%	91.2%

** All the statistical indicators refer to the period of the dataset (2002 to 2017).

AVG: Average; SD: Standard Deviation; IPY: increase per year (slope of linear regression of values).

RSD and RIPY refer to relative values of SD and IPY. Equations are $RSD = SD/AVG$ and $RIPY = IPY/AVG$.

R² is the square of the Pearson product moment correlation coefficient (considering linear relation).

From Table 1 we observe that electricity generation is made primarily by natural gas and oil which has the maximum values on average (107.7 and 58.8 TWh per year respectively). However, those same fuels, natural gas, and oil show the greatest increments and reductions per year, in nominal (IPY) and relative (RIPY) terms. Hence, we observe that natural gas has covered the decrease in oil and the

necessary increase by electricity demand. Also, from the statistical indicators, we use the standard deviation in nominal (SD) and relative (RSD) terms as measures to analyze the stability in generation by fuels. In this regard, fuels as nuclear, renewable and coal show a relative steady behavior. Finally, the value of the Pearson coefficient (R^2) shows the linearity behavior of total and natural gas generation. From the information above, we could conclude that electricity generation is currently driven by natural gas which is a fossil fuel.

Also, we need information about how electricity is consumed to estimate air cooling electricity consumption. Figure 5 show total electricity consumption (line and data values) and relative consumption (bars) by sector. The discrepancy between data from Figure 4 and Figure 5 is due to technical and non-technical losses in the transmission and distribution of electricity.

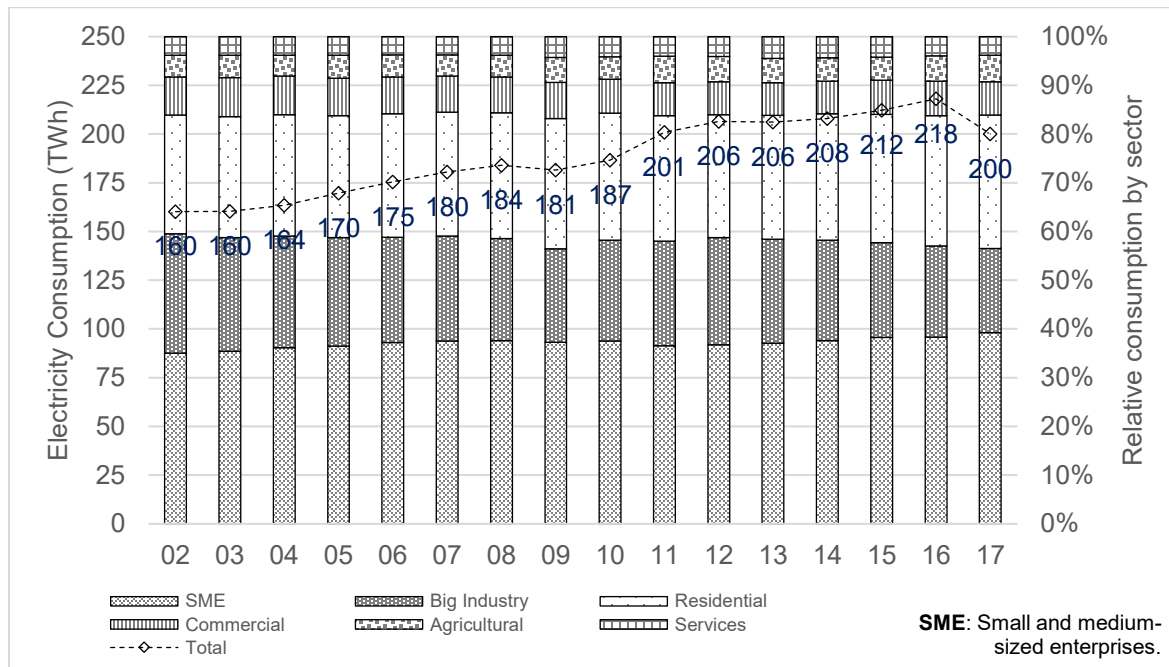


Figure 5. Total electricity consumption and relative by sector (SENER, 2020).

From the data above, we can estimate the national consumption by air cooling in 11.91% of the national electricity consumption as shown in Table 1. The data used to estimate the previous values is given on one side from the relative consumption by sector (Figure 5); and, on the other side, the relative AC consumption by economical sector is given by a study of electricity consumption in Mexico (IEI, 2012) and the value for the residential sector is given from a study made by a group of institutions under the name CEPAL (*Comisión Económica para América Latina y el Caribe*, by its acronym in Spanish). From this raw analysis, we observe that relative AC consumption is in the range from 12% to 14%. The value estimated agrees with information from Lepure (2018). Additionally, we must consider that the AC consumption could increase due to the direct proportional relation with population

and the constant increase in it. Also, AC consumption varies according to climate. For example, in arid climates, the residential consumption of AC could reach 44% of the total electricity consumption (Avila, 2018).

Table 2. Estimation of relative consumption by air-cooling.

Sector	Sector consumption (%) [*]	AC consumption (%)	Reference AC consumption
Industry	56.5%	6.50%	(IEI, 2012)
Residential	27.4%	21.20%	(CEPAL, 2018)
Commercial	6.9%	19.4%	(IEI, 2012)
Services	3.8%	29.0%	(IEI, 2012)
Weighted average^{**}		11.91%	-

^{*} Relative values from 2017.

^{**}The Weighted average represents the relative AC consumption respect the total electricity consumption.

Furthermore, electricity consumption, because of the way that electricity is generated based on fossil fuels, liberates greenhouse gases (GHG). In Mexico, the regulation of the general law in climate change (published on October 28th, 2014) creates the National Registry of Emissions which is known in Mexico by the acronym RENE (*Registro Nacional de Emisiones* in Spanish). Due to the cited regulation, since 2014⁵, the Ministry of Environmental and Natural Resources (SEMARNAT by its acronym in Spanish, *Secretaría de Medio Ambiente y Recursos Naturales*) publishes an emission factor which estimates the indirect GHG emissions by the consumption of electricity. The data of emissions factor since 2014 is presented in Figure 6.

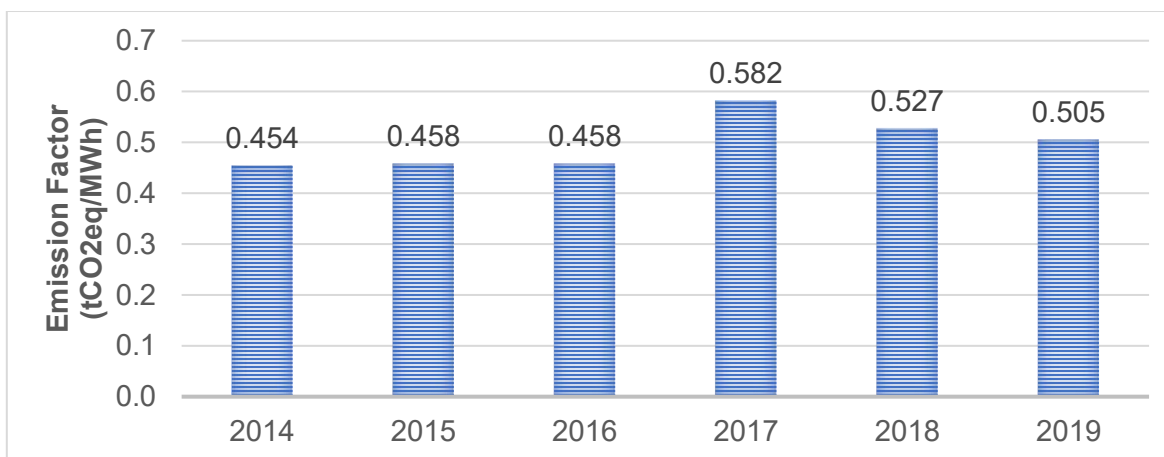


Figure 6. Emission Factor of indirect GHG emissions by the electricity consumption.

⁵ Prior to 2014, Program GEI (<https://www.geimexico.org/>) estimates the emission factor by electricity industry with the voluntary information from the power facilities.

In this study, we will use the last emission factor (EF) published (from 2019) to convert from consumption of electricity to GHG emissions. And the emission factor will be used to evaluate the reduction in tons of equivalent carbon dioxide (tCO₂eq) by the reduction of electricity consumption (e.g. increase in electrical efficiency).

1.2 HVAC systems description

Heating, Ventilation and Air Conditioning (HVAC) Systems purpose as defined by ASHRAE (2016) is “maintain desired environmental conditions in a space”. As the acronym is formed, it consists in three main systems: (1) Heating, (2) Ventilation and (3) Air conditioning. From these 3 systems, we will study only the last system: air conditioning which includes air cooling.

1.2.1 Conventional systems

Among HVAC systems, there are two main types: decentralized and centralized systems. The first type, decentralized systems, can be composed of one or more individual HVAC units. Each unit includes an integral refrigeration cycle, heating source, and direct or indirect outdoor air ventilation. The second type, centralized systems, consists of a single unit for multiple locations and/or big size installations. Although, the design and installation of a centralized system requires more coordination, it is not necessarily less expensive than a decentralized system. The benefits of centralized systems are suited for maximizing equipment service life (life cycle) and energy use, and a more efficiently operational workforce than its counterpart (ASHRAE, 2016).

As we established, we will focus on cooling devices which are part of the air conditioning in HVAC systems. In cooling systems, there are basically two conventional systems in which differences arise from the thermodynamic cycle approach. The two systems are (i) vapor compression (VC) and (ii) absorption cycles. The first type of system (VC) is based on a Rankine cycle which is a closed thermodynamic cycle. And the second type of system replaces the compressor from the VC cycle by a heat pump⁶ (Kreider et al., 2010). Diagrams of the two different systems are shown in Figure 7.

Additionally, vapor compression systems are the dominant HVAC technology. At least, in US⁷ 99% of the electricity consumption used in the US building sector for refrigeration purposes is from vapor compression systems (Goetzler, Zogg, et al., 2014).

⁶ In the absorption stage (absorber) heat is released from the system by an exothermic reaction of the absorption of refrigerant.

⁷ In countries where regulations encourage to use non-electric HVAC systems (e.g. Japan), absorption systems are popular.

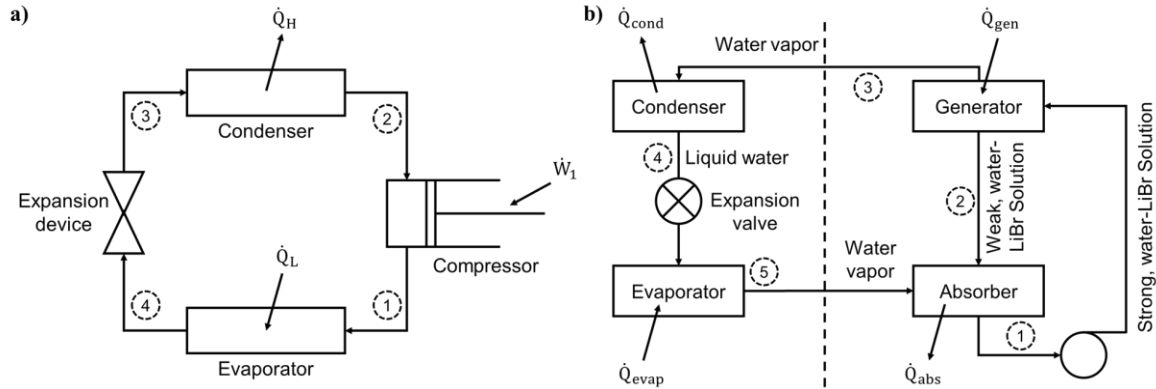


Figure 7. Diagrams of conventional cooling systems: a) mechanical equipment of a vapor compression (VC) (conventional) system; b) simple LiBr absorption cycle, to the left of the dashed line, the system represent the VC cycle (Kreider et al., 2010).

1.2.2 Strategies for HVAC energy saving

Despite the current conventional technologies for refrigeration. There are different emerging strategies for HVAC energy saving. The strategies for HVAC energy saving described are classified into three categories (Vakiloroaya et al., 2014): (1) Evaporative cooling systems, (2) different HVAC configurations, and (3) internal strategies for vapor compression system. The first category refers to replace the refrigeration system by one based on the evaporative cooling process. The second category regards to modify the configuration of HVAC systems by implementing an additional stage and thereby an increase in capital cost and maintenance. The third classification refers to strategies applied to additional stages (thermal storage, heat recovery⁸) or new strategies (liquid pressure amplification, evaporative-cooled condenser) on the different types of cooling systems (air-cooled, water-cooled and ground-coupled). Figure 8 shows a schematic diagram of HVAC energy-saving strategies.

⁸ Heat recovery stage for HVAC systems is a widely used strategy to improve energy efficiency as is included in ASHRAE Handbook—HVAC Systems and Equipment (ASHRAE, 2016).

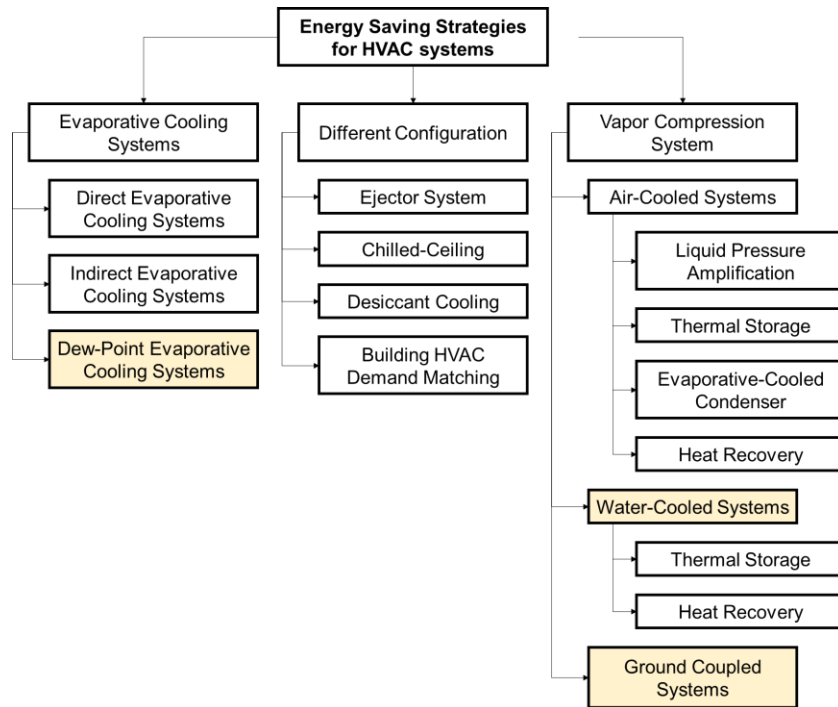


Figure 8. Strategies to improve energy efficiency in HVAC systems (Vakiloroaya et al., 2014).

A study from US Energy Department (DOE) characterizes the development status and reported energy savings from different non-vapor compression technologies (Goetzler, Zogg, et al., 2014). The study also classified the technologies based on the climate regions recommended to implementation. Evaporative Cooling was classified as a commercially available and applicable to Hot-Dry regions only. Figure 9 shows the information discussed above.

Additionally, the DOE engages the development of the Research and Development (R&D) roadmap for HVAC technologies (Goetzler, Guernsey, et al., 2014). The roadmap had the objective to provide guidelines from which DOE achieves the goal of reducing HVAC-related building energy consumption. The report identified and prioritized R&D initiative technologies. Initiatives research in evaporative cooling and nanofluids were classified as number 25 and 26, respectively. The initiatives were part of Tier 2 Direct-Impact Initiatives. Those initiatives, though not were articulated in depth as Tier 1 initiatives discussed in the report, were defined as valuable opportunities to save energy.

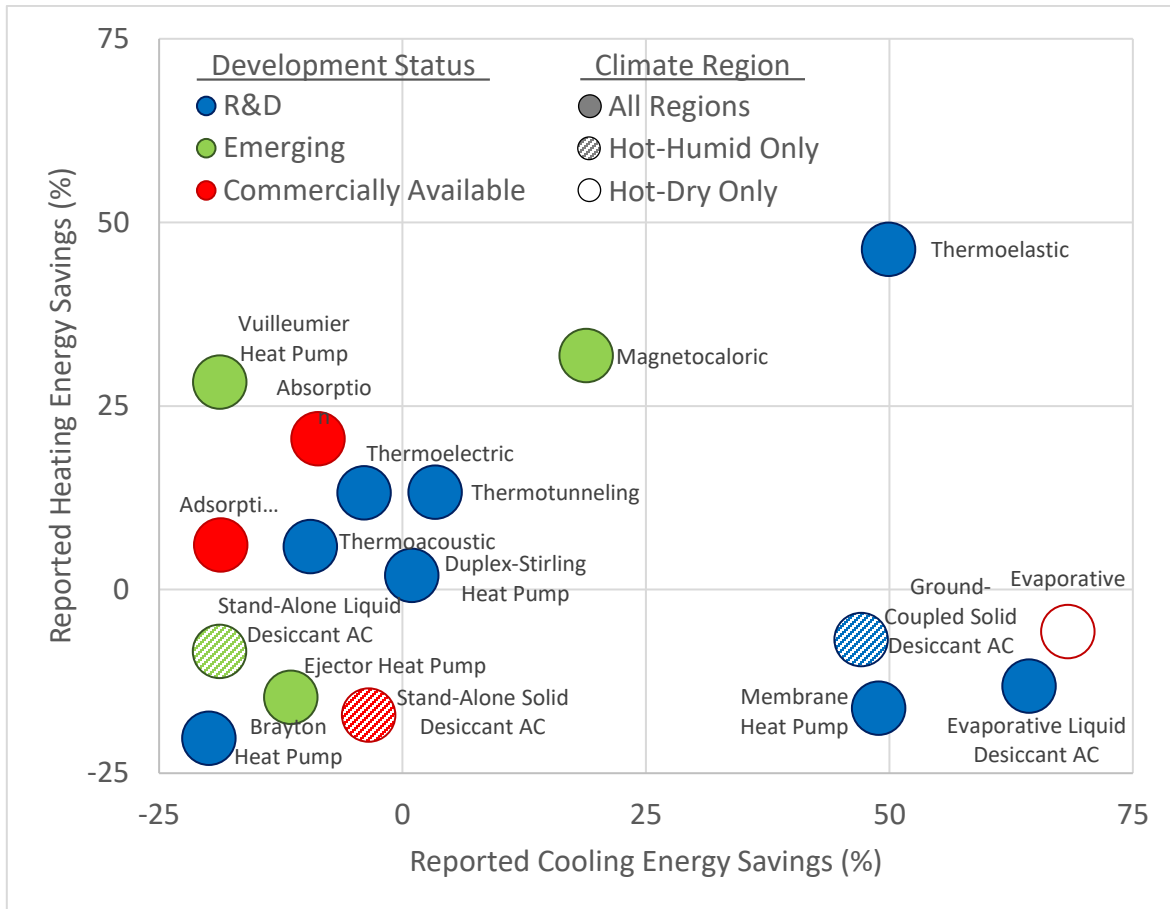


Figure 9. Energy savings, development status and geographic applicability of 17 non-vapor compression technologies.

Based on the strategies reviewed, the development status of technology and initiatives recommended, this study will investigate two research topics. These topics are showed in Table 3.

Table 3. Research topics investigated.

ID	Research topic	Initiative*
1	Demonstration of Dew-Point Evaporative Cooling Systems as High-Performance packaged HVAC Systems	25
2	Nanofluid impact on HVAC systems	26

* Initiative number in the Development and research Roadmap (Goetzler, Guernsey, et al., 2014)

While the first strategy regards to a complete cooling system. The second strategy refers to the working fluid on heat exchangers of HVAC systems. The heat exchanger used in this study is a helical coil because of its information available for validation.

1.2.3 Technologies investigated

1.2.3.1 Dew-Point Evaporative Cooling Systems

Before defining a Dew-Point Evaporative Cooling System (DPEC). We must define the evaporative cooling phenomenon. Evaporative cooling works from the natural interaction between dry air and water. The result of the interaction of an airflow and water is the decrease of sensible heat and the increase of latent heat in the airflow. In other words, the air decreases its temperature by the expense of gaining moisture in the process. It exploits a natural phenomenon to cool air and reduce electricity consumption when is compared with the VC cycle.

The three main evaporative cooling cycles are: (i) direct evaporative cooling (DEC), (ii) indirect evaporative cooling (IEC) and (iii) dew-point evaporative cooling (DPEC) (Sadighi-Dizaji et al., 2018). Figure 10 shows diagrams of the three cycles. Although some authors consider five cycles (Porumb et al., 2016), we consider Masiotsenko Cycle (M-Cycle) and Regenerative cycle (REC) as part of DPEC cycle. The 3 cycles (DPEC, REC and Masiotsenko) shares the feature that part of the airflow in the dry-channel is used as the airflow in the wet-channel. This feature allows that the air outlet temperature of the dry-channel could reach temperatures below the wet-bulb temperature. Hence, the theoretical lowest airflow temperature is the dew-point temperature of the airflow at the inlet conditions. In contrast, the lowest temperature that could reach conventional⁹ direct and indirect evaporative cooling systems is the wet-bulb temperature of the airflow at the inlet conditions. DPEC systems could reach temperatures below the inlet wet-bulb temperature because the wet-bulb temperature of the airflow at the beginning of the wet-channel is lower than the wet-bulb temperature of the airflow at the entrance of the dry-channel. The 3 cycles are showed in Figure 10.

⁹ There are systems which are named multi-stage IEC cycles which implement 2 or more IEC pair of channels consecutives. We are not considering multi-stage cycles as a different cycle because the physical basis is the same of REC and Masiotsenko cycles.

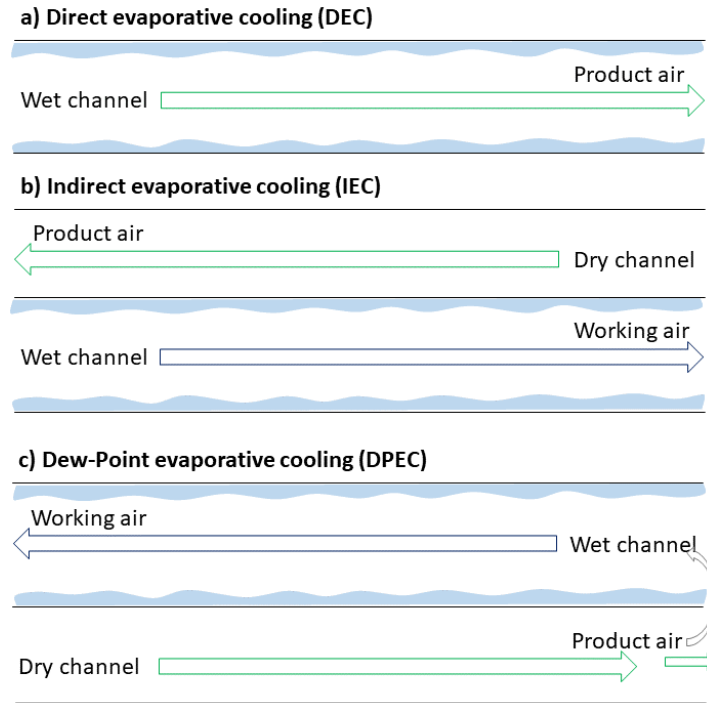


Figure 10. Main evaporative cooling cycles.

In evaporative coolers, the flows of air involved can be divided into two types: product and working air. On one hand, the product air is the refrigerated airflow, which passed through the dry-channel, and it is delivered in the volume of interest. On the other hand, it could be an auxiliary airflow named working air, which is cooled to remove heat from the product air and gain moisture in the process. Regarding the flow types, in the DEC cycle, it only exists a product air which is in contact with water; in the second cycle (IEC), the working air is in contact with water and the product air is not; and, in the third cycle (DPEC), part of the product air converts into working air reaching lower temperatures than the other cycles (Mahmood et al., 2016) due to reasons established above.

1.2.3.2 Nanofluids and helical coils

Nanofluids (NF) are a promising technology of heat-transfer fluids as they offer enhancement on heat transfer performance (X.-Q. Wang & Mujumdar, 2008). The nanofluid term was coined by Choi and Eastman in a study prepared for US DOE, Basic Energy Sciences-Materials Sciences Division (Choi & Eastman, 1995). Nanofluids are defined as a colloidal mixture that results from adding particles of nanometric scale ($<100^{-9}$ m) to a base fluid (Bretado de los Rios et al., 2018). The new fluid shows an enhancement of their thermophysical properties and therefore a more efficient heat transfer in various applications (Menni et al., 2019).

Regarding the heat exchanger, helical coils were initially investigated from curved pipes (Williams et al., 1902). Then remarkable advances were made on the

flow in curved pipes by investigating a similar “critical velocity”¹⁰ for helical coils (Eustice, 1910) and showing the modification in stream-lines for the same configuration (Eustice, 1910). The first appearing of a theoretical approach to helical coils shown the existence of a secondary flow (Dean, 1927). Finally, a more recent theoretical formulation of helical flow give us the following orthogonal coordinate system based on helical flow named Helical coordinate system (Germano, 1982).

ξ_i	s	r	θ
h_i	$1 + \kappa r \sin(\theta + \phi)$	1	r
v_i	u	v	w

where ξ_i represent the i -th orthogonal coordinate; h_i is the i -th scale factor; and v_i is the i -th velocity component from a Cartesian coordinate system. The relation between the Helical coordinate system and the orthogonal coordinate system for helical flow is shown in Figure 11.

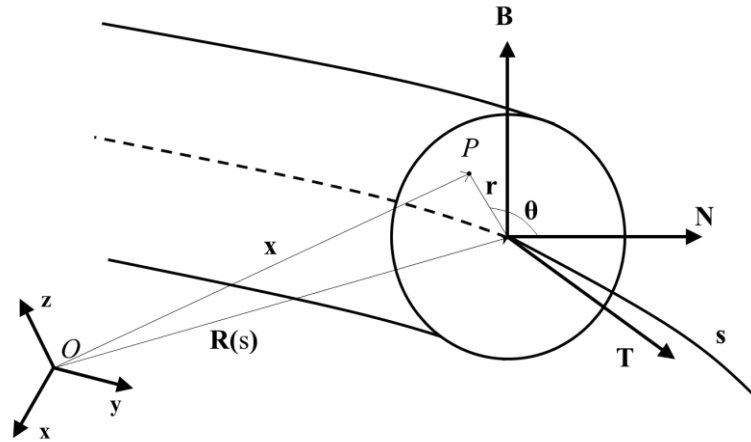


Figure 11. Helical coordinate system (Germano, 1982; C. Y. Wang, 1981).

1.2.4 Computation Fluid Dynamics

Over the last century, there were two common approaches for attacking complex problems in fluid mechanics and heat transfer: analytical and experimental procedures. However, due to the increase in speed and capacity of computers during the last half of the twentieth century, a third approach had been consolidated as a new methodology for tackling these problems (Anderson et al., 1997). This third methodology is known as Computational Fluid Dynamics (CFD by its acronym). CFD solves (usually) partial differential equations that govern a process of interest (governing equations). Moreover, CFD had been proved as an effective

¹⁰ In 1883 Reynolds Osborn defined a General Law of Resistance before the appearing of sinusoidal waves (eddy's) in internal flow by the means of resistance on tubes (Reynolds, 1883). This appearing of eddy's was later defined as Turbulent flow.

methodology, which reduces the time and cost of developing experiments¹¹ and with sufficient precision in their results as the analytical approach.

The two common methods to solve fluid-related problems from a CFD approach are: Finite Volume Method (FVM) and Finite Element Method (FEM). Although FEM code is widely established for structural mechanic problems, it is not reliable for fluid problems. The lag can be explained because fluid problems are generally more complex to solve (Ferziger & Peric, 2002). Additionally, in recent years commercially available codes using CFD and specifically Finite Volume Method have become easy to use (Andersson et al., 2012).

1.3 Problem definition

The importance of improving the efficiency of electricity consumption has increased over the years. One of the major sectors of electricity consumption has been HVAC systems. Which continuously increase is expected in the following years due to the increase in population. In this regard, two technologies have been selected to simulate and assess their impact as part of HVAC systems. These technologies are: (1) Dew-Point Evaporative Cooling Systems and (2) Helical Coils Heat Exchanger (HCHE) using Nanofluids. In the following section, we show the literature review made.

1.4 Literature review

1.4.1 Dew-Point Evaporative Cooling

Maclaine-cross & Banks (1981) developed a numerical model of a wet surface and its interaction with a fluid. For the construction of their model, they use the assumptions enunciated by Sadighi et al. (2018). For solving the mathematical model, they use finite differences (named algebraic equations). The model considered that wet-bulb temperature was reached which allows a simplification of it. They found that wetting the surface of the plate between dry- and wet-channels improve the heat transfer between both channels. They conclude that the prediction of the outlet temperature was based on the correct estimation of heat exchanger in the plate between dry- and wet-channels.

Riangvilaikul & Kumar (2010b) developed a numerical model for the heat and mass transfer of the DPEC based on a previous experimental work (Riangvilaikul & Kumar, 2010a). The model results were validated and compared with their experimental work mentioned above. The assumptions for the model were (a) that the system was adiabatic (no heat loss with the exterior), (b) the wet surface is always wetted (entirely saturated), (c) neglect the thermal conductivity of water and wall between dry- and wet-channel due to the relatively low thickness (0.5 mm).

¹¹ Experimentation is still very important because most of the practical problems in the common-life or industry involve complex geometries and/or complex flows which require very precise results not accomplished neither analytical nor numerical approach.

Some remarks of the model developed is the use of relation for heat and mass transfer coefficients with Lewis number in the wet channel. The results of the model were within a 5% for the outlet temperature and within 10% for wet- and dew point-effectiveness.

Zhan et al. (2011) built their own DPEC system and developed a mathematical model to represent the phenomenon. The main assumption of their model was to consider that both airflows on the dry- and wet- channels were at the same temperature. The consideration of equal temperature on both channels relies on the tiny thickness of the plate which separates them. They continue its study by developing a sensitivity analysis and assessing the performance of the model in 11 European cities. They conclude that a necessary dryness of the climate is necessary for the reliability of the DPEC systems.

Lee & Lee (2013) built a DPEC device to run experiments and developed a numerical model to predict more results. The developed model considered the flow hydraulically and thermally fully developed, constant properties regardless temperature, a unity Lewis number, and neglect the very low thermal resistance of water film and wall between channels. The system built considered thermal characteristics of materials such as using aluminum and brazing connections for the plate and a special hydrophilic treatment on the wetted porous layer. Remarks about their mathematical model were the use of enthalpy for the energy balance in the wet channel, a mass balance in the wet layer, and the use of finite differences to solve the ordinary differential equations. They found an optimal extraction ratio of 0.3 for their model. Finally, they compare the physical model and results achieved with other studies.

Anisimov and Pandelidis developed a series of studies regarding Masiotsenko cycle. From 2014 to 2015 they publish several studies regarding numerical models, experiment work and analytical comparisons of M-Cycle with other cycles or by varying conditions and geometry (Anisimov et al., 2014; Anisimov & Pandelidis, 2014, 2015; Pandelidis et al., 2016; Pandelidis & Anisimov, 2015, 2016b, 2016a). In 2014, they developed mathematical models for four airflow patterns: parallel-flow, counter-flow, crossflow and regenerative based on NTU-balances. They found an optimal extraction ratio of 0.3-0.45 for their model and this range agrees with other models (Anisimov & Pandelidis, 2014). Also, in 2014, they compare their results of the numerical model with experimental data from a testing bench at The National Snow and Ice Data Center, USA. They made an extensive sensitivity analysis on the factors that most influence the performance of M-cycles. They conclude that dew-point effectiveness (or wet-bulb effectiveness) should not be the unique indicator on the performance on this devices due to the inverse relation with cooling capacity (Anisimov et al., 2014). In 2015, their mathematical models for the four different flow patterns was compared against experimental published data of an indirect evaporative cooler (Rey-Martinez et al., 2004). The results showed that Lewis Unity is not applicable under some air-flow conditions when return air in the wet-channel is significantly greater than product air in the dry-channel. They also recommend climate conditions using the psychrometric chart for each airflow. They conclude their study by presenting modifications to the air flow patterns studied with the goal

to take advantage on the strengths of each airflow pattern (Anisimov & Pandelidis, 2015). The same year, in 2015, they developed another study with the consultation of Coolerado company, where they vary the holes arrangement on the heat exchanger of HMX device. The holes were part of a Masiotsenko cycle where the airflow in the dry-channel passed to the wet-channel. The different arrangements consist of placing the holes at different patterns and number of holes along the dry channel. And, by varying the size of channels and number of channels of HMX device. They found that the dry channel should be from 3 to 7 times higher than the wet channel and that holes should be evenly distributed along dry-channel (Pandelidis & Anisimov, 2015). Finally, in 2016 they studied other features of M-cycle such as the use of desiccant (Pandelidis et al., 2016), an statistical regression model to predict the performance of their system (Pandelidis & Anisimov, 2016a) and the optimization of the performance of their device and the applicability in selected world cities (Pandelidis & Anisimov, 2016b).

Lin et al. (2016) developed a numerical model of a counter-flow DPEC device. They compared their numerical results with experimental data from other studies and found good agreement between them. Their mathematical model considered the flow in both transient and steady states. To solve the numerical model, they use the finite differences method. They found that a mesh increased from 50 to 150 represents a variation of 0.03°C or 0.13% in the outlet temperature. The final mesh was selected of 100 cells. Their device had a length of 1 meter, and it was found that the airflow in the wet-channel reached saturation at 0.68m from the inlet of the wet-channel. They found that extraction ratios above 0.5 and channel lengths longer than 1.8 meters, the wet-bulb effective remains constant at a value of 1. Finally, it was remarked in the study that they modeled evaporative cooling based on the phenomenon driven by a difference of partial pressures in the water (saturated) and in the air.

Sadighi et al. (2018) compared and explained the mathematical model of 7 different analytical models based on 14 assumptions applied or not in their models. They all share 4 assumptions: (i) no thermal and moisture diffusivity in the flow direction, (ii) adiabatic system (no heat transfer to the surroundings), (iii) impervious walls, and (iv) pressure and mass flow rates constant and uniform in both streams. They also present results of studies made from 3 different numerical methods applied: (i) ϵ -NTU, (ii) finite methods (FM), and (iii) statistical design methods. Among the effects on parameters found by the ϵ -NTU method, increment of air inlet temperature and the increment of secondary to primary air flow ratio highlight. For finite methods, they explain the main characteristics of 7 studies. From statistical design methods, 2 types are described: (i) Response surface methodology, and (ii) group method of data handling (neural network type). The results from these statistical design methods are fast mathematical models, which may be more properly for engineers. From the experimental investigations, they compared arrangements, inlet flow characteristics, geometry, and results (outlet temperature, wet-bulb efficiency and dew-point efficiency). They contribute with comments about the industrial status of the M-cycle air coolers. They highlight that there are more than 200 patents of M-cycle and that this kind of technology has been more

applicable in big halls rather than for the residential sector. Finally, they state that the future research should be directed to the exergetic analysis of the M-cycles, determine how can be applied for the residential sector, the best way to use perforations to reduce the pressure drop and the best operational conditions, geometry and relevant aspects of M-cycle air conditioning systems.

Liu et al. (2019) made a 2D simulation in which they analyze the heat and mass transfer between the dry and wet channel in a dew point evaporative cooling device. They assume a 2D geometry due to the small height of the channels compared to the length and width on both channels. Assumptions made in the analysis were steady-state, no heat losses to the surroundings, totally wetted wet-channel, constant thermophysical properties, and constant temperature in the water of the wet channel. Its control volume was half of the dry channel and half of the wet channel. Then, the control volume was divided into 3 zones: dry channel, wet channel, and water film. They developed a model with equations of momentum, energy, and mass transfer which are different for each zone. For the equation of energy in the water film, energy losses due to mass vaporization were considered. In contrast with the other zones. In the wet channel, they add mass equation applied to the transport of humidity (water vapor). To verify its model, different Nusselt relations were compared among them and with experimental data. The model was implemented in COMSOL software, which used Finite Element Method (FEM) and they validate mesh independence with change in the product air temperature. The results shown that the model developed was within 3% of error regarding experimental data. Finally, they run a sensitivity analysis of inlet velocity, extraction ratio, water inlet temperature, volumetric flow rate, inlet air temperature, and inlet humidity. The performance parameters were the product air temperature and cooling capacity. They found that both product air temperature and cooling capacity increase with inlet velocity and inlet dry-bulb temperature. They found an optimal extraction ratio dependent of the flow conditions. They assess an impact of less than 1°C in the product air temperature for an increase of 10°C of the water. Finally, they conclude that product air temperature could be controlled through regulating wet-bulb temperature of the inlet airflow.

Pakari & Ghani (2019) performed experiments on a DPEC system and developed mathematical models of it. Their numerical models were in a 1D and 3D dimensions approach. Among their interesting assumptions, they considered the Lewis unity and a longitudinal conduction of heat in the water film. They also considered that the water and the plate between channels were at the same temperatures as discussed in various studies above. They found that 1D and 3D models agreed within a 3% of error, considering 3D model as the reference base case. Both models were compared with experimental data, obtaining an error of 10% and 8%, respectively. From this study, it was taken that using the 1D model for a DPEC system is a reliable and efficient option to simulate with a large set of data. This model was taken as the base model to simulate the DPEC system.

1.4.2 Nanofluids and helical coils

We present studies of conventional fluids and nanofluids in helical coils heat exchangers with the purpose of further discussion in this study.

1.4.2.1 Conventional fluids

Gnielinski (2009) developed a correlation for the annulus region of a double tube heat exchanger. His study also reviewed results from different experimental works and found a good agreement with the correlation developed. Also, they observed that an empirical correlation from Prandtl obtained good agreement with most of the available experimental data.

Jayakumar et al. (2008) run an experimental and numerical study on the flow of water in a helical coil for a specific geometry. The numerical results were validated with experimental data. Also, the heat transfer coefficient was in good agreement with Dittus-Boelter equation. The experimental set-up consists of a shell and coil heat exchanger, while the numerical study run experiments for constant wall temperature, heat flux and convective heat transfer coefficient. The simulations were performed with the realizable k- ϵ turbulence model with standard wall functions. The results shown that using thermal dependent properties were in better agreement rather than using constant values. Also, it was found that for shell and coil geometries is essential to couple wall heat transfer to simulate the experiment appropriately.

Jayakumar et al. (2010) analyzed 12 different configurations of helically coiled tubes. They modified the coil diameter, pipe diameter, and coil pitch. They obtained four Nusselt number correlations: average Nusselt number for fully developed flow as a function of Reynolds, Prandtl and, curvature ratio for two kinds of boundary conditions (temperature and heat flux wall constant); and also the local Nusselt number as a function of Reynolds, Prandtl, Nusselt number average and, angular position. They use Gambit software for meshing, Fluent software for solving the model, AnuVi (software developed by BARC – Bhabha Atomic Research Centre in Bombay) for post-processsing, and Matlab® and C++ codes were used to automate creation of planes and lines. Finally, its physical model consists of a mesh density of 9.963×10^8 cells/m³ ~ 393,324 cells.

Pawar & Sunnapwar (2013) run 138 tests for Newtonian fluids of water and glycerol water mixture (10-20 vol%) and 276 tests for non-Newtonian fluids such as dilute aqueous polymer solutions of sodium carboxymethyl cellulose (SCMC) and, sodium alginate (SA). The geometries under analysis were three, in which the coil curvature ratio varied (0.055, 0.064 and 0.0757). The experiments were at isothermal steady-state and non-isothermal unsteady state boundary conditions. They used a dimensionless number, named M in their correlations. This dimensionless number represents the ratio of inertia force to viscous force. In helical coils the M number replaces the Reynolds number. The Isothermal condition was applied at $65 \pm 0.2^\circ\text{C}$ by an on-off control of electrical resistances. The non-isothermal unsteady condition was applied by reaching the maximum power of the

electrical resistances. The results showed that M number is found to be sufficient to characterize the hydrodynamic flow in helical coils. Also, the overall heat transfer coefficient is higher for lower pitch coil diameters due to the increased effect of centrifugal force on secondary flow. Additionally, it was found that water showed higher heat transfer coefficients than mixture water-glycol and non-Newtonian fluids.

Pawar & Sunnapwar (2014) conducted 216 tests to obtain correlations for Newtonian and Non-Newtonian fluids in helical coils. These numerical experiments were in the same conditions such as the experimental work made in a previous study from them (Pawar & Sunnapwar, 2013). Regarding the CFD simulation, there were two approaches: temperature dependent and constant thermophysical properties. Besides typical governing equations (continuity, momentum, and energy), there were considered Boussinesq hypothesis and $k - \varepsilon$ turbulence model. The mesh was unstructured and non-uniform. They found several correlations for Nusselt number dependent on various dimensionless numbers such as: Reynolds, Dean, Prandtl, curvature ratio and the M number. Four correlations were found based on experimental data, one was obtained for laminar flow in CFD simulations and three applied for non-Newtonian fluids based on CFD simulations. They found new correlations for Nusselt number and friction factor at any practical curvature ratio based on the previous experimental work and CFD simulations.

1.4.2.2 Nanofluids

Kim et al. (2009) experimentally studied the convective heat transfer using water as base fluid with alumina (Al_2O_3) and amorphous carbonic (AC) nanoparticles. They run one the first experimental studies of nanofluids and their results are present validation data in a variety of studies. The investigation was performed under laminar and turbulent flow regimes. The experimental results showed that heat transfer at 3 vol% concentration of Al_2O_3 increased to 15% and 20% for laminar and turbulent flow regimes, respectively. For AC nanoparticle, the increase in heat transfer at 3.5 vol% was of 8% for laminar flow, while a negligible increase was observed for turbulent flow regime. Also, they found that Al_2O_3 showed an increase of 8% in its thermal conductivity at 3 vol%, while no detected increased in thermal conductivity was measured for AC nanoparticle.

Huminic & Huminic (2011) carried on numerical analysis on a double tube helical (coil-in-coil) for laminar flow conditions. They used CuO and TiO_2 nanoparticles in water base fluid. They assumed thermophysical properties from particles with 24 nm diameter. Nanofluids were in the inner tube at hotter temperature, while in the annulus circulated cold water. They found that varying flow rate in the annulus has a great impact in the heat transfer rate, as well as the concentration nanoparticles in the water outlet temperature. The results showed that for the same mass flow rate in both tube parts, the enhancement of NF in heat transfer was 14% for CuO at 2 vol%. The simulations were validated for Nusselt numbers in the annulus for nanofluids.

Mohammed & Narrein (2012) performed a numerical analysis in a double tube (or helically coiled tube heat exchanger - HCTHE). In the inner tube a nanofluid was flowing at 323 K, and in the annulus tube water was flowing at 273 K. The flow was

laminar and variable in the inner tube, and laminar and constant in the annulus tube. The fluid was water with CuO nanoparticle at 4% volume concentration. The numerical model assumed temperature-independent thermophysical properties. In their simulation, they varied helix radius, helix pitch, flow (parallel or counter), and annulus/inner diameters for four different laminar mass flow rates. Their results showed that heat transfer can be enhanced by reducing the helix radius, increasing the inner tube diameter, and decreasing the annulus diameter. Also, pressure drop increased as the helix radius decreased, and it decreased as the inner tube diameter is increased.

Jamshidi et al. (2012) performed a numerical study on the optimum design parameters of nanofluids flowing inside helical coils. They tried nine different geometries using three different coil diameters, three coil pitch and the same diameter. The restriction in the geometry was that geometries should fit into the same length. The fluid was alumina (Al_2O_3) with water at 0.5%, 1%, 2% and 3% volume concentrations. The model was implemented in ANSYS CFX-12 which uses the Finite Volume Method. The models considered single-phase nanofluids and used temperature-dependent and constant thermophysical properties. The boundary condition was a first-class constant wall temperature. They found that the most important parameters were coil diameter, coil pitch, and the correlations used for estimating fluid thermophysical properties. Finally, the optimum design was the one with the highest coil diameter, the lowest pitch coil, and the lowest Reynolds number (~ 1780). Those properties do not change across water, nanofluid and nanofluid with temperature-dependent properties formulations. However, the NF with temperature dependent properties showed that the optimum configuration was using 1 vol%.

Pakdaman et al. (2012) presented an experimental analysis in a helical vertical tube using oil/MWCNT as nanofluid. The concentrations used were 0.1%, 0.2% and 0.4% weight base. The authors validated its results against an analysis of thermophysical properties in a straight tube. Then, they presented their results of the performance index for helical coils and nanofluids in both straight tube and helical coils. Their results showed that using nanofluids in a straight tube reached a performance index of 1.5 with 0.4%wt at $\text{Re} = 10$. While, for a helical coil with the base fluid, the maximum performance index found was 5.1 at $\text{Re} = 487$. Finally, the maximum performance index found for the nanofluid studied at 0.4%wt concentration in helical coils were 6.4 at $\text{Re} = 20$.

Akhavan-Behabadi et al. (2012) run numerical experiments using oil/MWCNT nanofluid and validate its results for base fluid using the correlations of Nusselt number and pressure drop from Bergman et al. (2011). Then, they tried its system for straight tube and helical coil with oil/MWCNT at 0.1%, 0.2% and 0.4% weight concentration. The Nusselt number increased up to 45% compared to base fluid in straight tubes. The Nusselt number increased up to 60% in helical coils compared to the base fluid.

Kannadasan et al. (2012) performed simulations to compare horizontal and vertical coil tubes in a shell. They used two concentrations (0.1 and 0.2 vol%) for

Cuo/Water nanofluid. They compared heat transfer and pressure drop inside those geometries experimentally. They showed that heat transfer and pressure drop increased as the nanoparticle concentration increased. Also, they found that vertical coils observed a slight increase in its performance ratio compared to horizontal coils. In general, both coils using nanofluids showed a better performance when they are compared with water. Finally, they developed correlations for shell and coiled tube as a function of nanofluid concentration and Dean Number (1600-4000) in turbulent flow conditions.

Hashemi & Akhavan-Behabadi (2012) conducted simulations with CuO nanoparticles in oil SN-500 base fluid. The weight concentrations used were 0.5%, 1% and 2%. The numerical experiments were in the laminar regime flow ($Re < 150$) a constant heat flux of 1500, 2650 and 3800 W/m²). They compared the heat transfer coefficient and pressure drop using a helical tube and nanofluids with results found in a straight tube. They found that using a helical tube, the performance index was 1.16 while using helical tube and nanofluids the performance index was 1.26. Therefore, for practical applications, nanofluids in helical coils are a good option.

Narrein & Mohammed (2013) numerically investigated the flow characteristics in a double tube heat exchanger using four different type of particles (Al_2O_3 , SiO_2 , CuO, ZnO) in water as base fluid at a 4 vol% concentration. Then, they analyzed the effect of concentration (1 to 4 vol%) with CuO/Water nanofluid. Also, the authors found results for CuO and different base fluids (water, ethylene glycol and engine oil) at a concentration of 4 vol%, and they considered different particle diameters of CuO/water nanofluid at 4 vol%. The results revealed that pressure drop is an important parameter on heat transfer with nanofluids. They also noted that if CuO/water nanofluid is used with more than 2 vol%, the heat transfer tends to show less increase and pressure drop continues increasing. Another result was that as nanoparticle diameter increased, the pressure drop decreased.

Kahani et al. (2013a) developed numerical simulations and experimental work using two nanoparticles (Al_2O_3 and TiO_2) in water. The volume concentrations used were 0.25%, 0.5%, 0.75% and 1%. As boundary conditions, they used constant heat flux in a helical coil of two curvature ratios (0.05 and 0.1), varying the pitch in one. The experiments were in laminar flow regime, calculating the critical Re number at 4500. The results showed that Al_2O_3 /water have a better performance than TiO_2 due to their large ratio of surface area to mass. However, the stability time was 45 days for TiO_2 and 48 hours for Al_2O_3 . Finally, according to experimental results, the smallest curvature ratio and higher pitch coil showed the best performance. Although, the pitch spacing effect had a weaker impact than curvature ratio.

Another approach by Kahani et al. (2013b) was the development of computational simulations in three different helical coils combining two curvature ratios (0.05 and 0.1) and two pitch coils (24 and 42 mm). They used alumina (Al_2O_3) with water as nanofluid in volume concentrations of 0.25%, 0.5%, 0.75% and 1%. Their validation was against theoretical data for a straight tube with water and helical coil for the respective Prandtl number. The results showed that the curvature ratio has a greater impact than the pitch coil by increasing heat transfer and pressure

drop. They observed that using NF in a helical coil can enhance heat transfer until 320% compared with a straight tube. Finally, they noted that increased in heat transfer was higher at lower Reynolds numbers.

Again, Kahani et al. (2013c) reported numerical analysis of MWCNT nanoparticles in water base fluid with weight concentrations of 0.1%, 0.3% and 0.5%. The experiments were run in laminar flow regime in three different helical coils. The boundary condition was a constant heat flux of 100 W at the wall for all cases. Its results were validated against a theoretical correlation.

Fakoor-pakdaman et al. (2013) investigated the effect of pressure drop with helical coils and nanofluids as working fluid. They concluded that the use of both techniques increases the pressure drop. Other factors that increased the pressure drop was the Reynolds number. Finally, they reported a correlation for the pressure drop in helical coils based on the pressure drop for straight tubes, a modified Dean number and concentration of nanoparticles (MWCNT) in the base fluid (oil).

Wu et al. (2013) conducted numerical simulations with Al_2O_3 /water nanofluid for five different volume concentrations of 0.20%, 0.56%, 1.02%, 1.50% and 1.88%. The experiments were performed in laminar and turbulent regimes, considering critical Reynolds number of 6,000 and the highest Re value of 65,600. A correlation for average bulk Nu was found for laminar regime. On the other hand, for turbulent flow, results showed a negligible increase with base fluid. Finally, it was shown that thermophysical properties such as viscosity affects significantly the Nusselt number. They observed that if bulk average Nusselt number is compared with the Reynolds number, the error increased up to 40% in relative terms, while comparing Nusselt number with the velocity bulk average basis, it showed a perfect agreement with existing correlations of single-phase.

Khairul et al. (2013) developed an analytical study on the entropy generation rate for different nanoparticles and base fluid water in nanofluid with turbulent flow. The nanoparticles used were CuO, Al_2O_3 and ZnO in volume concentrations from 1% to 4%. The boundary condition considered was constant heat flux. The model considered the diameter particle of 25 nm and the Brownian motion in the thermal conductivity. For the Nusselt number, they used previous correlations of Nusselt number and friction factor for vertical coils (Kannadasan et al., 2012). They concluded that CuO/water nanofluids could increase the heat transfer coefficient and decreased entropy generation about 7.14% and 6.14%, respectively.

Akbaridoust et al. (2013) studied the difference between experimental and homogeneous/dispersion models in steady-state flow. The flow was laminar, incompressible and at constant wall temperature. They analyzed four configurations of helically tubes with 0.1% and 0.2% water-CuO nanofluid. They found that using a homogeneous model produce an error of 20-30% compared with experimental results. By contrast, the dispersion model lowered the error to about 4% compared with experimental results. The dispersion model used was modifying the model used by Mokmeli & Saffar-Avval (2010), which considers the nanoparticle size. The modifications were two: replacing the gradient velocity by the magnitude of gradient velocity and calibrating a dispersion coefficient that best suit to the phenomena of

curved pipes. The value of the dispersion coefficient calculated was $C_d = -1.194 \times 10^{-8}$.

Zonouzi et al. (2014) developed a CFD study using base fluid water and alumina (Al_2O_3) nanoparticle in different helical coils. They maintained the same length and varied the coil diameter. The volume concentrations used were 0, 1%, 2% and 3% in a laminar flow regime. The boundary condition was set to wall temperature. For the numerical model, they used a two-phase mixture model with temperature dependent properties, including the thermal expansion coefficient. The validation agreed with experimental data from Kim et al. (2009). They observed that higher overall heat transfer coefficients (OHTC) by adding 1% volume fraction of Al_2O_3 to the base fluid in a helical tube with lower PCD than in a helical tube with higher PCD. The last is also true for straight tubes.

Aly (2014) numerically studied the heat transfer and pressure drop in tube-in-tube helical coils using different coil diameters in turbulent flow regime. The working nanofluid was water as base fluid and alumina (Al_2O_3) as nanoparticle in a volume concentration range from 0.5% to 2%. The study was developed using CFD technique in a commercial software (ANSYS Fluent 14). There were used inlet temperatures as boundary conditions in the numerical experiments. The study found that Realizable k- ϵ turbulent model with wall enhanced treatment and temperature-dependent properties (conductivity and viscosity) had to be selected carefully to reach a good agreement with existing correlations from Gnielinski (1986) for Nusselt number and Mishra & Gupta (1979) for friction factor.

Rakhsha et al. (2015) investigated both experimentally and numerically the flow in helical coils using water base fluid and cupric oxide nanoparticle (CuO) at a maximum volume concentration of 1%. The experiments were at constant temperature boundary condition. The numerical experiments were run with the OpenFOAM software. They reported that the convective heat transfer coefficient and the pressure drop per unit length increased when nanofluids were used as the working fluid. The numerical convective heat transfer coefficient and pressure drop increased by 6-7% and 9-10%, respectively. On the other hand, the experimental heat transfer coefficient and pressure drop increased by 16-17% and 14-16%, respectively. The numerical experiments were run using measured thermal conductivity and viscosity. The results showed good agreement with Jayakumar et al. (2010).

Srinivas & Vinod (2016) studied numerically a shell and agitated helical coiled tube. They use Al_2O_3 as nanoparticle and water as base fluid in the shell-side. For the coil side, pure water was used. The weight concentrations used were 0.15%, 0.3%, 0.45%, 0.6% and 0.75%. The flow regimes in the helical coil were laminar, transition and turbulent. They found that using nanofluids require less energy to heat the shell-side to a desire temperature. The results showed that the laminar regime saved more energy than the turbulent regime. Also, for the maximum concentration, it was found the highest energy savings of 10.65% for 2 lpm and maximum stirrer speed (1500 rpm) at the maximum temperature shell-side of 50°C. Finally, it was observed that a higher outlet temperature was reached as an additional feature.

Huminic & Huminic (2016) review heat transfer and fluid flow in curved tubes using conventional fluids and nanofluids. Their heat exchangers geometries of interest are classified into three groups: (1) helical coiled tubes, (2) spirally coil tubes, and (3) others heat exchangers. They emphasize the use of helical coiled tubes due to the sub-classification of these heat exchangers. They classified works on helical coiled tubes as experimental, numerical, and analytical studies. The last classification is applied for both conventional fluids and nanofluids. In the case of conventional fluids, some remarks about the review articles state that the curvature ratio (d/D) and pitch ($2\pi\lambda/D$) ratios have significant effects on the average heat transfer coefficient. Correlations were made for: friction factor, heat transfer coefficient, mass transfer coefficients, Nusselt number, Reynold number, and Dean Number. Regarding nanofluids, the main remark is that heat transfer rate and pressure drop increase with increasing nanoparticle concentration and Reynolds number. The same characteristics from conventional fluids apply when the thermophysical properties of nanofluids are considered. Finally, for other geometries the review only found studies using water as a base fluid in nanofluids.

Bizhaem & Abbassi (2017) performed a numerical simulation using nanofluid water/ Al_2O_3 at 1%, 2% and 3% volume concentration in helical coils. The simulations were considered developing and laminar flow regime at Reynolds numbers of 500, 1000 and 1500. The geometry consisted in a curvature ratio (δ) of 0.1 and non-dimensional pitch (λ/R) of 0.06366. The simulations were performed in Fluent, with temperature-dependent thermophysical properties and using a Eulerian-Eulerian mixture model (2 phases). The boundary condition was constant wall temperature and the inlet was set at velocity and temperature constant values. They validated the simulation with 3 cases: (i) correlation for straight tubes, (ii) experimental and simulation data for helical coils and (iii) existing correlations for Nusselt number at different radial positions for a given cross-sectional area. The results revealed that the mixture model is appropriate for the simulation case, and nanofluid has greater effects in heat transfer at low Reynolds number. Also, small Reynolds numbers showed less entropy generation.

Kumar & Chandrasekar (2019) conducted a CFD analysis on a double helically coiled tube. They used MWCNT/water nanofluids. The analysis was made in ANSYS R14.5. They varied the volume concentration at 0.2D, 0.4D and 0.6% and Dean Numbers from 1300 to 2000. The assumptions of the analysis were: incompressible, single-phase, radiation and net convection neglected; the physical properties were not temperature-dependent and constant heat flux condition. They found that the Nusselt number increased as particle concentration increased, by 20%, 24% and 30%, respectively. Also, the friction factor and pressure drop were proportionally direct to particle concentration, and they decreased increase in 12%, 22% and 30% and 0.38, 0.3914 and 0.45 bar, respectively. One remarkable conclusion of the study was that as the thermal conductivity increased in the nanofluid by the effect of temperature, the viscosity reduced its effects.

Finally, Hajatzadeh-Pordanjani et al., (2019) took the approach on the application of nanofluids in heat exchangers. They addressed different applications of heat exchangers using nanofluids, which possible reduce energy consumption,

volume of the heat exchanger and indirectly save water and industrial waste. First, they describe the different heat exchangers for current applications. Then, they describe the characteristics of nanofluids and focus on the thermophysical properties of nanofluids and how they vary according to other variables. In the following sections, the study describes the preparation of nanofluids, hybrid nanofluids (combination of nanoparticles), and it shows evidence of the benefit when nanofluids are applied in heat exchangers and how nanofluids impact the process of energy management. The review concluded that more studies are needed regarding the treatment of thermophysical properties and Brownian motion in 3D domains.

1.4.3 Remarks

1.4.3.1 DPEC system

- Although there are analytical, experimental, and numerical studies of evaporative cooling systems. We focus on numerical studies of DPEC systems specifically.
- 15 articles were reviewed related to dew-point evaporative cooling numerical models. These numerical models commonly depart from energy balances in the airflows, water, and plate. Previous numerical models have the following model characteristics:
 - To be in 1D, 2D and 3D dimensions.
 - Steady and transient state.
 - Constant and dependent temperature thermophysical properties.
- The common assumptions among the models developed are (Sadighi-Dizaji et al., 2018):
 - No moisture nor thermal diffusivity in the flow directions.
 - The heat exchanger is adiabatic (no heat transfer to the surroundings).
 - The walls between the channels are impervious to liquid (water).
 - Mass flow rate and pressure are constant and uniform for both airflows.
- There was not found a correlation to estimate the outlet temperature in DPEC systems.
- Also, there are no information published about the performance of DPEC systems in the region of Mexico.
- Regarding the model details, there stand out some characteristics of the numerical models:
 - The Lewis factor varies from 0.91 to 1.09 when the ratio of the cooling capacity on the wet channel and the dry channel have a value of 1 and 2, respectively. A Lewis factor unity is fulfilled when the ratio is lower than 1 (Anisimov & Pandelidis, 2015).
 - There is an agreement about the range of the optimal extraction ratio, placing it between 0.28 – 0.35 (Anisimov et al., 2014; Liu et al., 2019; Pakari & Ghani, 2019).
 - The error in a DPEC model from a one-dimension model to a three-dimensions model when the models are compared with experimental data decreases from 10% to 8.5% (Pakari & Ghani, 2019).

1.4.3.2 Nanofluids in HCHE

- We review 5 studies of numerical analysis in conventional fluids and 24 studies of numerical analysis using nanofluids.
- Previous numerical analysis in helical coils depart from conventional fluids with thermophysical properties dependent on temperature (Jayakumar et al., 2010).
- Specifically, for HCHE, the numerical studies reviewed do not simulate more than 3 nanofluids.
- Also, commercial software (Fluent and Comsol) has been used to solve the numerical model of nanofluids in HCHE.
- There are different mathematical models developed. The models that stand out are the dispersion model (Akbaridoust et al., 2013; Zonouzi et al., 2014), the mixture model (Bizhaem & Abbassi, 2017) and single-phase model (Rakhsha et al., 2015).
 - In this regard, a single-phase nanofluid mathematical model showed good agreement with experimental data (Aly, 2014).
- There are not an agreement on the definition of the thermophysical properties correlations of nanofluids in combination with the mathematical model to properly simulate nanofluids thermal applications.
- More research about thermophysical properties and Brownian motion in heat exchange applications of nanofluids is necessary (Hajatzadeh-Pordanjani et al., 2019).

1.5 Objective

To evaluate the performance of the two distinct emerging technologies in HVAC systems through numerical simulations: (1) Dew Point Evaporative Cooling (DPEC) systems, and (2) Nanofluids in helical coils heat exchangers.

1.5.1 Specific objectives

The specific objectives by technology are:

DPEC system

- To develop a numerical model of a DPEC system.
- To characterize the effect of environmental variables and design parameters in the thermal performance of the DPEC model developed.
- To evaluate the performance in an hourly basis of the DPEC model in 4 climates (very arid, arid, mild, and warm).

Heat exchangers with Nanofluids

- To simulate nanofluids in helical coils heat exchangers on a commercial software.
- To evaluate the effect on the heat transfer and fluid dynamics of using different geometries, base fluids, nanoparticles, nanoparticle concentration and inlet velocities in the simulations of nanofluids.

1.6 Scope research

Regarding the first technology, A parametric analysis of a 1D numerical model for a DPEC system was carried. The model was evaluated for 8760 hours of a typical year for the climates: very arid, arid, warm, and mild. The model considered thermophysical properties dependent on temperature, humidity ratio and atmospheric pressure.

On the other hand, an analysis of the thermal performance and fluid dynamics of 9 different nanofluids formed by 3 base fluids and 3 nanoparticles. The analysis includes the evaluation of 7 geometries, 4 Dean numbers and 3 volume concentrations. The model considered thermophysical properties dependent on temperature from the base fluid, constant thermophysical properties from the nanoparticles and the diameter of the nanoparticles.

1.7 Methodology description

The methodology for each technology has different features as will be explained in this section. Even so, a general methodology was followed for each technology as shown in Figure 12. Henceforth, we refer to the DPEC model as 1D model (or vice versa) and the HCHE with nanofluids as 3D or Nanofluids model.

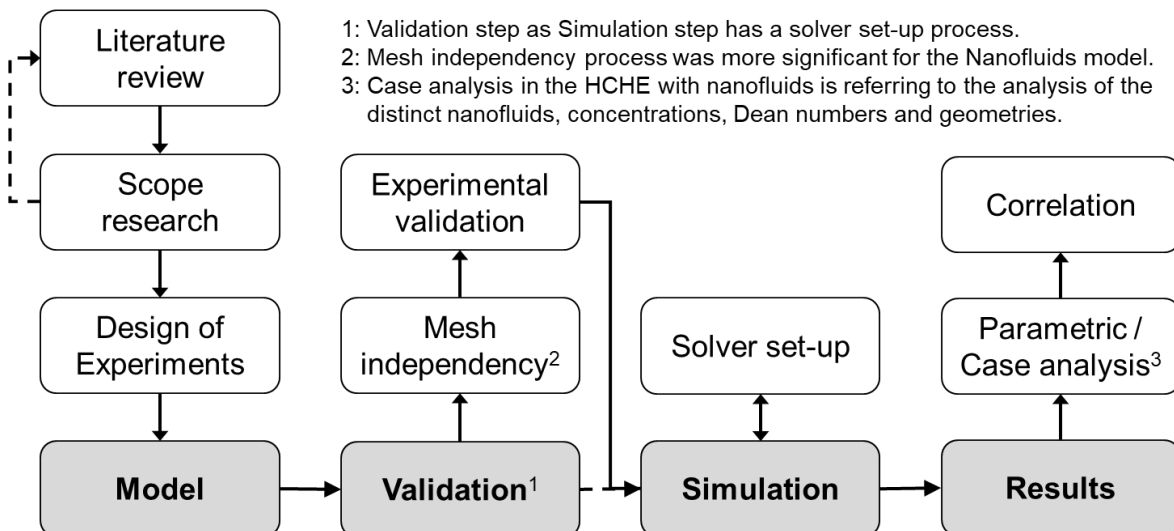
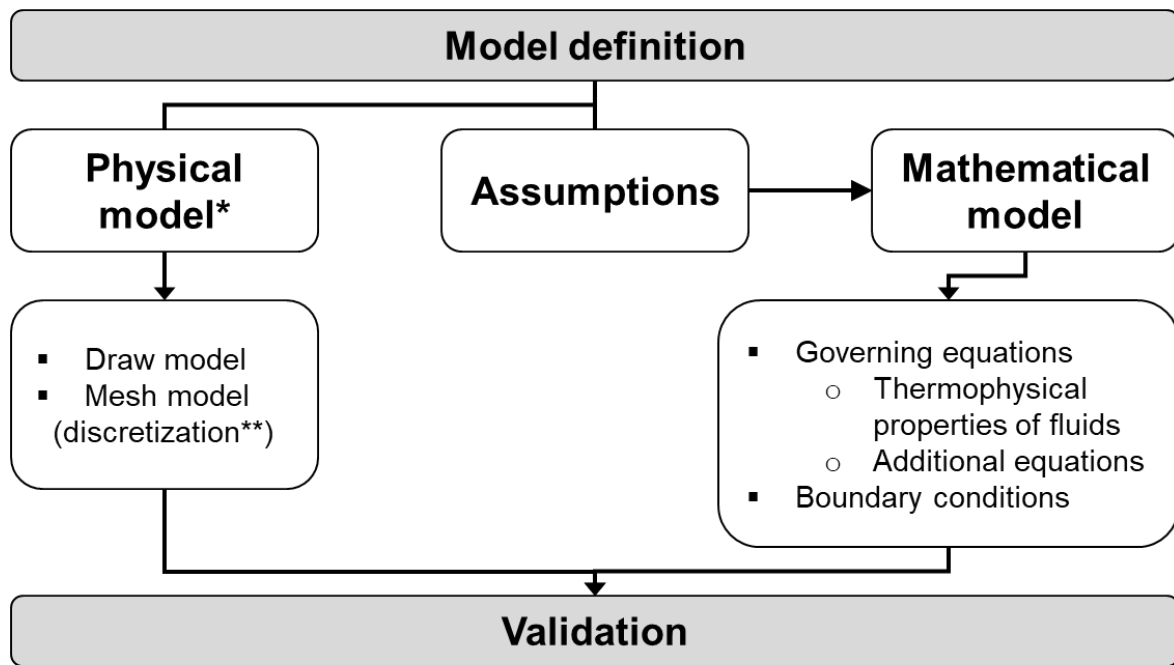


Figure 12. General methodology to assess each technology. The correlation process does not apply for the DPEC model.

Figure 12 shows the four main processes of the general methodology. The first process (Model), literature review and research scope constituted an important and iterative process in the definition of the model. In detail, from literature review were known what model characteristics have been used in previous studies. Then, the Design of Experiments (DoE) were set-up according to the scope research

established. The result of these mentioned steps is the model. In turn, the model consists of three main features (i) physical model, (ii) assumptions and (iii) mathematical model. At the same time, mathematical model consists of two parts: (a) governing equations (includes thermophysical properties and additional equations) and (b) boundary conditions. These model characteristics are shown in Figure 13.



* Physical model is a process for 3D model only. However, physical 1D model is considered in the mathematical model.

** A discretization process is made for 1D model but is part of the solver set-up (options) in Simulation step.

Figure 13. Components of the model definition which are considered in Validation and Simulations processes.

The following process after the Model was established is the validation process. In this stage, there are two important sub-processes: mesh independency and experimental validation. For the mesh independency analysis, we run the mathematical model and varies the number of spatial elements (cells delimited by nodes – vertexes) in which the physical model was partitioned. This analysis is made to be sure that the elements size does not influence the results. In the experimental validation we took results from previous studies and compared with the current model. This comparative process is intended to verify that the model is reproducing significantly well the phenomena involved.

Then the simulation process is carried out, where it is important to set-up the solver. There are some differences between 1D model and 3D model which are worth to mention. Simulations for 1D model (including validation) are faster than the simulations for 3D model. And more important, 1D model simulations are automated to run for a typical year of each city. Whereas 3D model simulations must be done for each inlet conditions and nanofluid concentration. Each 3D model simulation took

about 2-4 hours and a scaled convergence criterion of $1e-4$ was set up for all residuals from governing equations.

Finally, the Results process comprehends two analysis: parametric or case analysis and the obtention of regression equations (correlations). For the parametric analysis, we discussed the impact of distinct variables in the selected parameters from the results of the simulations. And, in the second analysis, we found correlations to estimate selected parameters from the input values.

To finish the methodology description, we describe some remarks on the Solvers for each model. On one hand, 1D model was solved in MATLAB using the `bvp5c`¹² used to solve a system of differential equations, subject to boundary conditions. These problems are named boundary value problems. The code implemented is presented in the Appendix Section. On the other hand, we will use commercially software Fluent for solving the Governing equations involved in the helical coil heat exchanger. Fluent solves efficiently the differential equations involved, and it has user-friendly controls to set-up the model.

1.8 Thesis structure

In Chapter 1 , an Introduction from the conceptual terms of the importance of energy in actual society is presented. Then, the justification towards energy consumption and especially HVAC electricity consumption is reviewed for Mexico. Also, the strategies and technologies to increase energy savings in HVAC sector are shown and the selection of the two technologies researched in this study. Then, the literature review regarding numerical studies of DPEC systems and numerical studies of conventional fluids and nanofluids are presented. The scope research, objectives and methodology are finally presented in this chapter.

Later, in Chapter 2 it is exhibited the characteristics of the DPEC numerical model regarding the physical model, assumptions and mathematical model. In the subsection of mathematical model, an analysis of energy balances is presented as the basis to establish the governing equations. Finally, the chapter finishes with the description of the parametric analysis and the selection of the cities in which the performance of the DPEC model was studied.

In Chapter 3 we describe the features of the Nanofluids model. As in the previous chapter, we describe the physical model, assumptions and mathematical model that were present in the simulations. In this chapter, if the reader is interested in find insights about the simulations, it is recommended to take attention at every note present in the section. Also, one important part to take attention are the development of temperature-dependent thermophysical properties of nanofluids as a second order polynomials. All the values and coefficients of functions are present in the chapter. Then, it is described the parameters varied in the case analysis. A

¹² More information about `bvp5c` algorithm is found in Mathworks website:
<https://la.mathworks.com/help/matlab/ref/bvp5c.html>

summary table with all values of parameters varied is present at the end of the chapter.

Next, in Chapter 4 , the results of the two numerical models simulated are reported. The chapter divides into two sections results: DPEC model and Nanofluid model. The validation and parametric analysis of the DPEC model is first presented and compared with previous studies. Then, the results of the performance of the model is reported for different cities of Mexico. In the second section of this chapter, regarding the Nanofluids mode, we describe first the mesh independency analysis and then the validation with a reference study. Afterwards, the results regarding the variation of geometry, Dean number, concentration and, nanofluid (base fluid and nanoparticle) is shown for each variable. The chapter ends with the development of correlations for the nanofluids.

Lastly, Chapter 5 presents insights and conclusions from the numerical models and their process. Future research work is finally included as the products of this study.

Chapter 2 DPEC model

This chapter describes the numerical model of a Dew-Point Evaporative Cooling (DPEC) system. We describe the considerations taken to define the physical and mathematical model from the real model. Next, we run a validation process which fit with the previous numerical model developed by other authors (Pakari & Ghani, 2019). Then, we evaluate the model through a parametric analysis and its performance for different climates. From the parametric analysis we obtained remarks about the model and the impact of different variables. At the ending section, we observe the throughput of the DPEC system in four different climates.

2.1 Model description

There were developed two models. One model is based on the model developed from Pakari & Ghani (2019), and the other includes modifications on additional equations to calculate thermal variables.

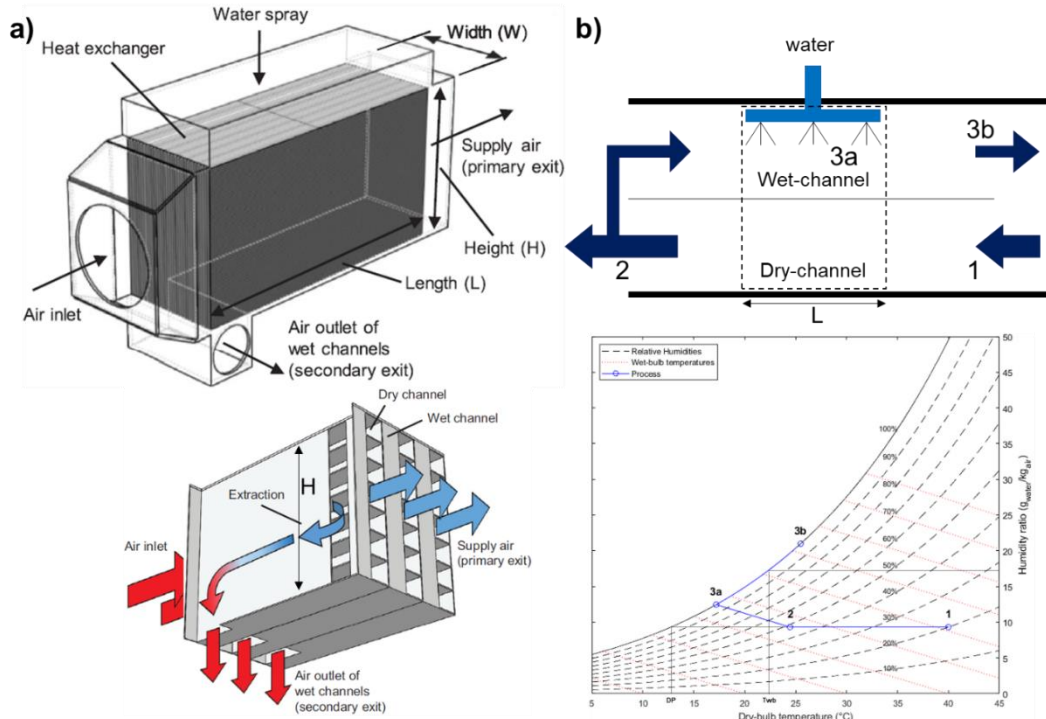


Figure 14. (a) Perspective view of the DPEC device and view of three stacked channel pairs for showing counter-flow, (b) schematic view of the DPEC device and psychrometric chart process. Twb and DP represent the wet-bulb temperature and dewpoint temperature of inlet air (Pakari & Ghani, 2019).

The device to analyze is the DPEC system shown in Figure 14.a). The physical model consists of a pair of channels as showed in Figure 14.b). It is worth to highlight

the points¹³ 1, 2, 3a and 3b. Point 1 represents the inlet air (ambient air) at the dry-channel; point 2 represents the outlet airflow from the dry-channel; point 3a represents the wet-bulb temperature of point 2; and point 3b represents a state forward point 3a in the wet-channel. Regarding the processes, the process 1-2 does not add water to the airflow and decrease the dry-bulb temperature. However, the process 2-3b is an adiabatic process (constant enthalpy) where the airflow increased its water mass content and decrease its dry-bulb temperature. Finally, process 3b-4 represents a heat exchange process while water mass increases.

The extraction ratio is the main feature of DPEC cycle. DPEC coolers reached lower temperatures because they first cool the air without adding water mass and then the evaporative cooling process (consider adiabatic) take place. This process permits to DPEC systems reach lower temperatures than DEC systems.

2.1.1 Physical model

The physical model is based on the system showed in Figure 14.a). We use the same geometrical characteristics of the system as used by Pakari & Ghani (2019). The device is a heat exchanger made by stacked corrugated plastic sheets with rectangular flutes of 2 by 3 mm, t_d and t_f , respectively. The corrugated layers shape the inside of the dry channel while the separation between them forms up the wet channels which has no flutes as the dry channel. The heat exchanger consists of 50 pairs of channels (wet and dry channels) stacked one each other. A diagram of a cross section of the stacked channels is visible in Figure 15.

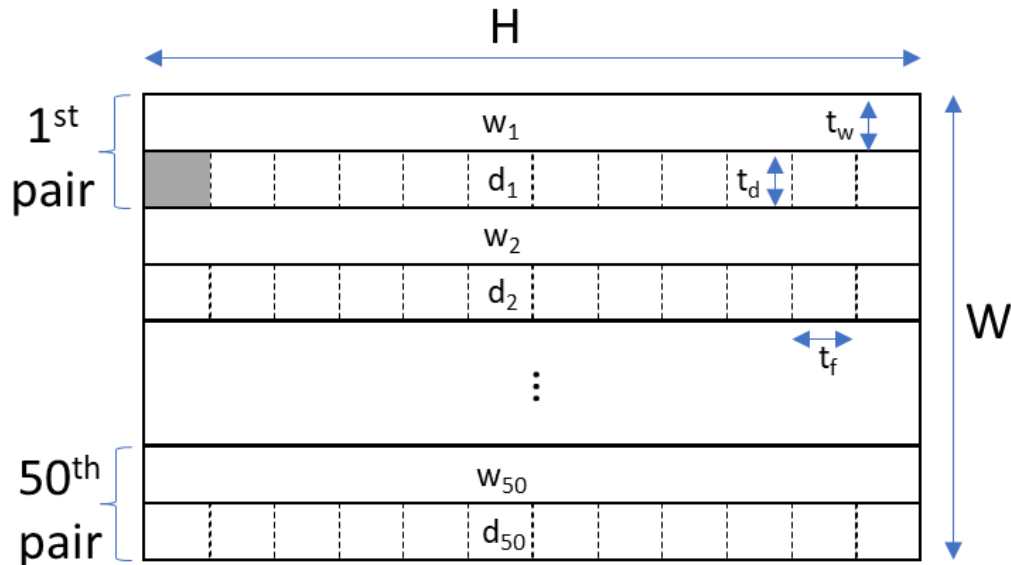


Figure 15. Schematic of a cross-section of the DPEC system.

¹³ A point should be understood as an airflow at a given temperature and humidity ratio.

The plastic sheets separate dry and wet channels, however, between channels there is a wick paper used to retain water in the wet channel. The wick paper allows a constant wetted wet channel. The dimensions of the system and details of the channels are established in Table 4.

Table 4. Dimensions of the physical model.

Parameter	Symbol	Value (mm)
Channels Length	L	500
Channels Height	H	300
Channels Width	W	220
Dry channels width	t_d	2
Wet channels width	t_w	2
Flutes height	t_f	3

The simplification of the physical model consists of one pair of dry and wet channels. Each channel has its own airflow named dry and wet airflow, \dot{m}_d and \dot{m}_w respectively. So, we relate both airflows by a dimensionless variable named *extraction ratio* ($ER = \dot{m}_w / \dot{m}_d$). Figure 16 shows the diagram of the pair of channels, it should be noted the direction and location of the x-origin and the mass flow delivered into the room which is the difference of dry and wet airflows.

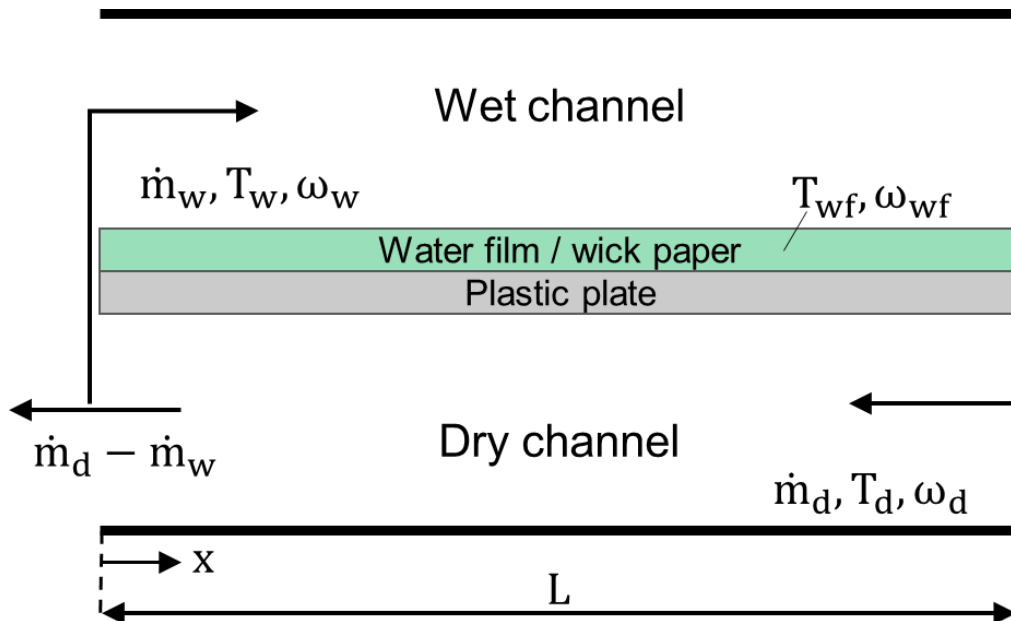


Figure 16. Physical DPEC model.

To obtain the governing equations we must study the heat and mass transferred in a differential volume of the physical model. A schematic of the differential control volume is showed in Figure 17. In the diagram, the thickness values for the plate (t_p) and the water film (t_{wf}) are 0.2 and 0.15 mm, respectively.

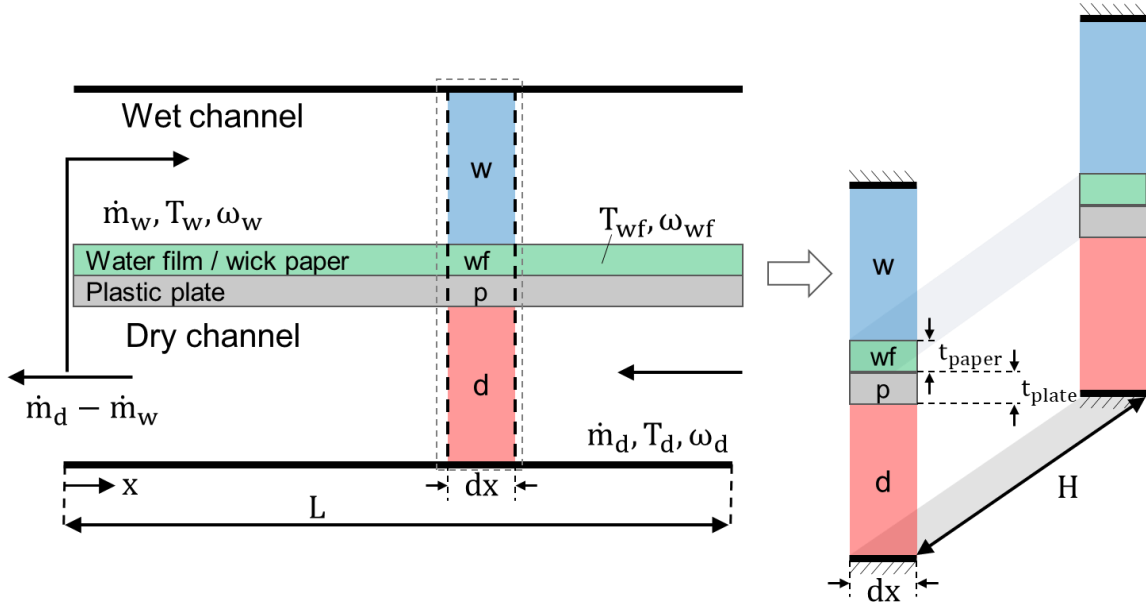


Figure 17. Schematic of differential volume of the control volume.

2.1.2 Assumptions

In this section, we enlisted all the assumptions considered for the two DPEC models developed. These assumptions have the intention to simplify the mathematical model without reducing the precision of the results. The main difference between the models are the thermophysical properties used in both models. On one hand, for the first model (M1), we use constant thermophysical properties. While, for the second model (M2), we use thermophysical properties dependent on temperature, humidity ratio and atmospheric pressure. The modification of thermophysical properties affects the convective and mass transfer coefficients. The assumptions shared for both models are enlisted in Table 5.

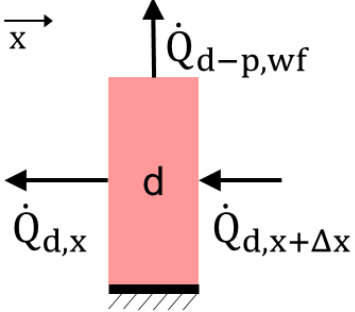
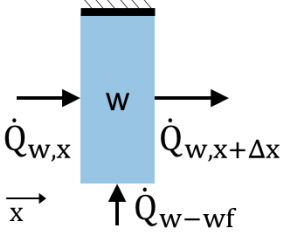
Table 5. Assumption for the two DPEC models developed.

ID	Assumption
1	The device is adiabatic, it means no heat transfer between the device and surroundings.
2	The height of the channel is small compared to the length. This means that the variation of temperature in the y-direction will be neglected. Only variation in the x-direction will be considered.
3	Laminar, incompressible, and fully hydraulic and thermal developed flow in both dry and wet channels.
4	Viscous dissipation is neglected.
6	Mass flow constant within an hour.
7	Lewis number unity
8	The water film and plastic sheet are at the same temperature.

2.1.3 Mathematical model

For each differential volume (w, wf, p, d) observed in Figure 17, we will balance the heat and/or mass transferred with the vicinity differential volumes. The balances observed from the differential analysis are evinced in Table 6.

Table 6. Differential analysis for DPEC model.

Diagram	Equations in detail	Equations
<p>1. Energy, dry channel</p> 	$\dot{Q}_{d,x+\Delta x} = \dot{Q}_{d,x} + \dot{Q}_{d-p,wf}$ $\Delta \dot{Q}_d = -\dot{Q}_{d,x+\Delta x} + \dot{Q}_{d,x}$ $\Delta \dot{Q}_d = -\dot{m}_d c_{a,d} (T_{d,x+\Delta x} - T_{d,x})$ $\dot{Q}_{d-p,wf} = U(T_d - T_{wf}) \Delta A_d$ $U = \left(\frac{1}{h_d} + \frac{t_p}{\theta_p} + \frac{t_{wf}}{\theta_{wf}} \right)^{-1}$ $\Delta \dot{Q}_d = -\dot{Q}_{d-p,wf}$	<p>a.1</p> <p>a.2.1</p> <p>a.2.2</p> <p>a.2.3</p> <p>a.2.4</p> <p>a.3</p>
<p>2. Energy, wet channel</p> 	$\dot{Q}_{w,x} + \dot{Q}_{w-wf} = \dot{Q}_{w,x+\Delta x}$ $\Delta \dot{Q}_w = \dot{Q}_{w,x+\Delta x} - \dot{Q}_{w,x}$ $\Delta \dot{Q}_w = \dot{m}_w c_{a,w} (T_{w,x+\Delta x} - T_{w,x})$ $\dot{Q}_{w-wf} = h_w (T_{wf} - T_w) \Delta A_w$ $\Delta \dot{Q}_w = \dot{Q}_{w-wf}$	<p>b.1</p> <p>b.2.1</p> <p>b.2.2</p> <p>b.2.3</p> <p>b.3</p>
<p>3. Mass, wet channel</p>	$\dot{m}_{ww,x} + \dot{m}_{evap} = \dot{m}_{ww,x+\Delta x}$ $\Delta \dot{m}_{ww} = \dot{m}_{ww,x+\Delta x} - \dot{m}_{ww,x}$ $\Delta \dot{m}_{ww} = \dot{m}_w (\omega_{w,x+\Delta x} + \omega_{w,x})$	<p>c.1</p> <p>c.2.1</p> <p>c.2.2</p>

	$\dot{m}_{\text{evap}} = h_m \rho_a (\omega_{\text{wf}} - \omega_w) \Delta A_w$ $\Delta \dot{m}_{\text{ww}} = \dot{m}_{\text{evap}}$	<p>c.2.3</p> <p>c.3</p>
<p>4. Energy, water film</p>	$\dot{Q}_{\text{wf},x+\Delta x} + \dot{Q}_{\text{wf}-d} = \dot{Q}_{\text{wf},x} + \dot{Q}_{\text{wf},-w}$ $\Delta \dot{Q}_{\text{wf}} = -\dot{Q}_{\text{wf},x+\Delta x} + \dot{Q}_{\text{wf},x}$ $\Delta \dot{Q}_{\text{wf}} = -\theta_p A_{\text{wf}} \left(\frac{dT}{dx} \Big _{x+\Delta x} - \frac{dT}{dx} \Big _x \right)$ $\dot{Q}_{\text{wf}-d} = \dot{Q}_{d-p,\text{wf}}$ $\dot{Q}_{\text{wf}-w} = \dot{Q}_{\text{evap}} + \dot{Q}_{w-\text{wf}}$ $\dot{Q}_{\text{evap}} = h_{fg} \dot{m}_{\text{evap}}$ $-\Delta \dot{Q}_{\text{wf}} = \dot{Q}_{\text{evap}} + \dot{Q}_{w-\text{wf}} - \dot{Q}_{\text{wf}-d}$	<p>d.1</p> <p>d.2.1</p> <p>d.2.2</p> <p>d.2.3</p> <p>d.2.4</p> <p>d.2.5</p> <p>d.3</p>

* The width of each control volume is given by $dx = x_2 - x_1 | x_2 > x_1$.

The negative sign on the right side of equation a.2.2 is given by the direction of the flow respect to the control volume¹⁴. Each balance in Table 6 give each one of the governing equations exhibit in Table 7. Here, we present the mathematical development to go from equations a-d to governing equation (4), which is a balance of energy in the water film. From now on, we described the arithmetic involved.

We substitute the correspondent terms on equation c.3:

$$-\Delta \dot{Q}_{\text{wf}} = \dot{Q}_{\text{evap}} + \dot{Q}_{w-\text{wf}} - \dot{Q}_{\text{wf}-d}$$

$$\theta_p A_{\text{wf}} \left(\frac{dT}{dx} \Big|_{x+\Delta x} - \frac{dT}{dx} \Big|_x \right) = h_{fg} \dot{m}_{\text{evap}} + h_w (T_{\text{wf}} - T_w) \Delta A_w - U (T_d - T_{\text{wf}}) \Delta A_d$$

$$\theta_p A_{\text{wf}} \left(\frac{dT}{dx} \Big|_{x+\Delta x} - \frac{dT}{dx} \Big|_x \right) = h_{fg} h_m \rho_a (\omega_{\text{wf}} - \omega_w) \Delta A_w + h_w (T_{\text{wf}} - T_w) \Delta A_w - U (T_d - T_{\text{wf}}) \Delta A_d$$

The delta area that multiplies each term on the right side of the last equation is the same ($\Delta A = \Delta A_d = \Delta A_w$). Its value is given by $\Delta A = H dx$ (see Figure 17). Also, A_{wf} is not a differential area and its value is given by $A_{\text{wf}} = H t_p$. Hence, dividing the equation by ΔA , we get as result:

$$\theta_p t_p \frac{\left(\frac{dT}{dx} \Big|_{x+\Delta x} - \frac{dT}{dx} \Big|_x \right)}{dx} = h_{fg} h_m \rho_a (\omega_{\text{wf}} - \omega_w) + h_w (T_{\text{wf}} - T_w) - U (T_d - T_{\text{wf}})$$

¹⁴ The signs come from the dot product of the direction (\vec{x}, \vec{y}) quantity (\dot{m}, \dot{Q}) and the direction of the unity vector area, where it points outside the control volume.

By getting the limit when $\Delta x \rightarrow 0$ in the left term and substituting in last equation and rearranging to the left side:

$$\frac{\left(\frac{dT}{dx}\right)_{x+\Delta x} - \left(\frac{dT}{dx}\right)_x}{dx} = \frac{d^2T}{dx^2}$$

$$\theta_p t_1 \frac{d^2T}{dx^2} = h_{fg} h_m \rho_a (\omega_{wf} - \omega_w) + h_w (T_{wf} - T_w) - U(T_d - T_{wf})$$

$$\theta_p t_1 \frac{d^2T}{dx^2} + h_{fg} h_m \rho_a (\omega_w - \omega_{wf}) + h_w (T_w - T_{wf}) + U(T_d - T_{wf})$$

All the procedure above gives as result equation (4). A similar procedure was made for each balance to prove the governing equations in Table 7.

2.1.3.1 Governing equations

The governing equations resulting from the heat and mass balances in each channel from Table 6 are revealed in Table 7.

Table 7. Governing equations for the DPEC model.

Type and location	Governing equations	Eq.
1. Energy in the dry channel	$-\dot{m}_d c_d \frac{dT_d}{dx} = UH(T_{wf} - T_d)$	(1)
2. Energy in the wet channel	$\dot{m}_w c_w \frac{dT_w}{dx} = h_w H(T_{wf} - T_w)$	(2)
3. Mass (water) in the wet channel	$\dot{m}_w \frac{d\omega_w}{dx} = h_m \rho_{air} H(\omega_{wf} - \omega_w)$	(3)
4. Energy in the water-film	$h_w H(T_w - T_{wf}) + UH(T_d - T_{wf}) + h_{fg} h_m \rho_{air} H(\omega_w - \omega_{wf}) + \theta_{plate} HL \frac{d^2 T_{wf}}{dx^2} = 0$	(4)

The four governing equations form an ODE system which can be solved by a numerical algorithm. These algorithms must receive an ODE system of first order. Then, we must convert the previous governing equations to a first order system to solve it. Specifically, we partitioned equation (4) into two equations:

$$\dot{T}_{aux} = \frac{dT_{wf}}{dx} \quad 4.a$$

$$k_p t_1 \frac{d\dot{T}_{aux}}{dx} + h_{fg} h_m \rho_a (\omega_w - \omega_{wf}) + h_w (T_w - T_{wf}) + U(T_d - T_{wf}) \quad 4.b$$

Therefore, the ODE system which we solve by a numerical algorithm is the set of equations formed by equations (1)-(3), (4.a) and (4.b).

2.1.3.2 Boundary conditions

The ODE system, apart from the governing equations, need the definitions of the boundary conditions to solve it. These boundary conditions are set up by climate dependent variables at the inlet, the consideration of the extraction ratio, and the adiabatic assumption of the device. The equations and comments regarding the boundary conditions mentioned are exhibit in Table 8.

Table 8. Boundary conditions for the DPEC model.

ID	Boundary condition	Comments
(5)	$T_d(x = L)$	Specified values.
(6)	$\omega_d(x = L)$	
(7)	$T_w(x = 0) = T_d(x = 0)$	Temperature and humidity for dry and wet channels at $x = 0$ are the same.
(8)	$\omega_w(x = 0) = \omega_d(x = 0)$	
(9)	$\left. \frac{dT_{wf}}{dx} \right _{x=0} = 0$	No heat transfer from to the surroundings (adiabatic)
(10)	$\left. \frac{dT_{wf}}{dx} \right _{x=L} = 0$	

2.1.3.3 Additional equations

To complete the mathematical model, we need to formulate the undefined terms in the governing equations.

$$U = \left(\frac{1}{h_d} + \frac{t_p}{\theta_p} + \frac{t_{wf}}{\theta_{wf}} \right)^{-1} \quad (11)$$

$$h = \frac{Nu \, k_{air}}{d_h}; \quad Nu_d = 2.811 \quad (12)$$

$$h_m = \frac{Sh_w D_{va}}{d_{h,w}}; \quad Nu_w = Sh_w; \quad Nu_w = 4 \quad (13)$$

$$c_w = c_d + \omega_w c_v \quad (14)$$

$$\omega_{wf} = 0.622 \frac{P_g}{P_{atm} - P_g} \quad (15)$$

$$P_g = 611.21 \exp \left[\left(18.678 - \frac{T_w}{234.5} \right) \left(\frac{T_w}{257.14 + T_w} \right) \right] \quad (16)$$

$$h_{fg} = 1000 (2501 - 2.369 T_{wf}) \quad (17)$$

$$\theta_p = 0.21 \frac{W}{m \, K}, \quad \theta_{wf} = 0.5449 \frac{W}{m \, K} \quad (18)$$

From equations (11)-(18), U is the overall heat transfer coefficient considering the equivalent thermal resistance given by the processes of convection and

conduction through plate and wet-film; h refers to the heat transfer coefficient of a channel with the plate; Nu is the Nusselt number which has constant values of 2.811 and 4 in the dry and wet channel, respectively; h_m is the convective mass transfer coefficient; Sh_w is the Sherwood number, and it will be set equal to the value of Nusselt due to Lewis unity consideration. Finally, additional equations are included to calculate the specific heat of humid-air $c_w(c_d, c_v, \omega_w)$ given the specific heat of dry-air (c_d), vapor (c_v) and the content of water (ω_w); saturated humidity ratio (ω_{wf}) given the partial vapor pressure (P_g) which is a function of airflow on the wet-channel (T_w), and the latent heat of vaporization (h_{fg}). The last term is calculated from the water-film temperature (T_{wf}).

The difference between the two models developed is the formulation for the thermophysical properties of the air. These values and functions of both models are presented in Table 9. It is notable to difference equations (21) and (22). Equation (21) refers to a specific heat capacity equation for a mixture air-vapor ($c_{p,m}$) which is applicable for both airflows in the wet and dry channels. In contrast, equation (22) refers to the formulation for the specific heat capacity equation for the air in the wet channel ($c_{p,w}$).

Table 9. Thermophysical properties of air in the two DPEC models developed.

Property	Symbol	Model 1	Model 2**	Eq.
Density (kg/m³)	ρ	1.2	$\rho_m = \frac{M_a P_0}{ZRT} \left[1 - x_v \left(1 - \frac{M_v}{M_a} \right) \right]$	(19)
Thermal conductivity (W/m²K)	θ	0.02588	$\theta_m = \frac{\theta_a + x_v(0.8536 \cdot \theta_v - \theta_a)}{1 - 0.1464x_v}$	(20)
Specific heat of dry air (J/kgK)	$c_{p,d}$	1 007	$c_{p,m} = c_{p,a}(1 - x_v) \frac{M_a}{M_m} + c_{p,v}x_v \frac{M_v}{M_m}$	(21)
Specific heat of wet air (J/kgK)	$c_{p,w}$	$c_{p,w} = c_{p,d} + \omega_w 1820$		(22)
Mass diffusivity of vapor in air (m²/s)	D_{va}	2.68×10^{-5}	$D_{va} = 2.178 \left(\frac{T}{273.15} + 1 \right)^{1.81} \times 10^{-5}$	(23)

** For further information of thermophysical properties equations of density (Picard et al., 2008), thermal conductivity, specific heat (Tsilingiris, 2008) please refer to Appendix A. For Mass diffusivity equation refer to Massman (1998).

In the following section, we explain the analysis made. It is important to remember that these analyses are made after a Mesh Independency test, and a validation of the algorithm implemented to solve the ODE system.

2.2 Analysis description

In this study we will run two different analyses:

1. Parametric analysis
2. Cases of study in different climates

The first type of analysis is to measure the impact of varying different variables such as control parameters of the system (air mass flow and extraction ratio), environmental variables (inlet temperature, humidity and pressure) and geometry of the equipment (length, width and hydraulic diameter).

2.2.1 Parametric analysis

The cases we will analyze will be set to analyze the effect of three variables:

1. Mass flow and extraction ratio
2. Climates (inlet conditions)
3. Equipment parameters (length of the system)

The base values and range of the parametric analysis are showed in Table 10.

Table 10. Base values and range of the different values for the parametric analysis.

Variable	Symbol	Base value	Range
Dry volumetric flow rate (CFM)	$\dot{V}_d = \frac{\dot{m}_d}{\rho_{air}}$	0.15	0.1 – 0.3
Extraction ratio	$ER = \frac{\dot{m}_w}{\dot{m}_d}$	0.33	0.1 – 0.75
Inlet temperature (°C)	T_{in}	30	26 – 40
Channel length (m)	L	0.5	0.5 – 0.7
Relative Humidity (%)	RH	50	10% – 90%
Pressure (kPa)	P	100	80 – 100

In this step, it is worth to mention that all psychrometric values of air could be calculated by knowing 2 different values (e.g. dry-bulb temperature and relative humidity or dry-bulb temperature and wet-bulb temperature).

The reference variables to compare the impact of modifying variables mentioned above are four:

- a. Outlet temperature of the dry channel (T_{out})
- b. Conditioning cooling capacity at 25°C – (\dot{Q}_{ref})
- c. Environmental cooling capacity – (\dot{Q}_{cool})
- d. Wet-bulb effectiveness (ε_{wb})
- e. Dew-Point effectiveness (ε_{DP})

Whereas outlet temperature is found by solving the ODE boundary value problem. The other 4 reference variables are functions of the outlet temperature and climate variables. Equations (24)-(27) are used to calculate these reference variables.

$$\dot{Q}_{\text{ref}} = \dot{m}_d(1 - ER)c_p(T_{\text{ref}} - T_{\text{out}}) \quad (24)$$

$$\dot{Q}_{\text{cool}} = \dot{m}_d(1 - ER)c_p(T_{\text{in}} - T_{\text{out}}) \quad (25)$$

$$\varepsilon_{\text{wb}} = \frac{T_{\text{in}} - T_{\text{out}}}{T_{\text{in}} - T_{\text{wb,in}}} \quad (26)$$

$$\varepsilon_{\text{DP}} = \frac{T_{\text{in}} - T_{\text{out}}}{T_{\text{in}} - T_{\text{DP,in}}} \quad (27)$$

These referenced variables are intended to provide information about the performance of the system in the different inlet conditions and climates. Concerning the first variable, conditioning cooling capacity, equation (24), is set to get the potential heat removed by the DPEC system from a zone of interest at a comfort reference temperature ($T_{\text{ref}} = 25^\circ\text{C}$). It is worth to mention that \dot{Q}_{ref} could be negative, indicating that the system could not remove thermal load from the space of interest. On the other hand, the environmental cooling capacity, equation (25), is set to obtain the heat removed from the ambient by the system. The other reference variables are different equations to measure the effectiveness of the system. Equation (26), ε_{wb} , is the wet-bulb effectiveness which measure the outlet temperature reached in terms of the difference of inlet temperature and inlet wet-bulb temperature. Next, in equation (27), ε_{DP} is the dew-point effectiveness and measures the outlet temperature reached in terms of the difference of inlet temperature and inlet dew point.

2.2.2 Cases of study

The model described in the first section of this chapter was used to calculate the performance of a DPEC system from a set of climatic values from meteorological stations across Mexico. Where set of values comprehend a typical year. We have selected 4 sets of climatic values near urban cities with different climates. These “cities” (set of climatic values) were selected considering the climates classification from Köppen adapted to Mexico (García, 2004). Figure 18 shows a map of the main climates in Mexico and the locations of the met stations.

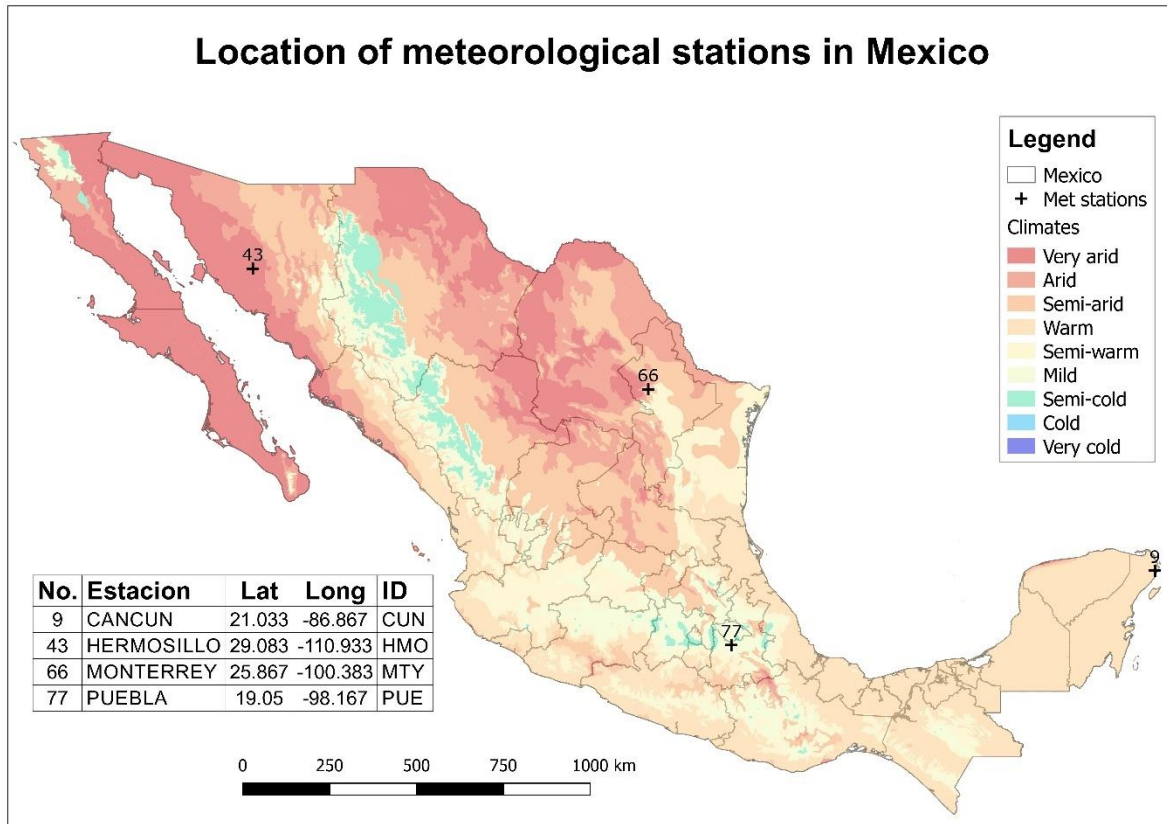


Figure 18. Map of main climates (García, 1998) in México and the location of met stations.

The characteristics of the cities selected are showed in Table 11.

Table 11. Cities (stations) characteristics.

City and state	Climate	Latitude (°)	Longitude (°)	Altitude (m)
Hermosillo, SR	Very arid	29.083	-110.933	278
Monterrey, NL	Arid	25.867	-100.383	550
Puebla, PL	Mild	19.05	-98.167	2175
Cancun, QR	Warm	21.033	-86.867	8

The atmospheric pressure of each station (city) was estimated from the altitude of the station at the corresponding cartesian coordinates (latitude, longitude). The altitude value was found from Google Earth® software and the atmospheric pressure for each city was calculated through equation (28).

$$P_{\text{atm,city}} = \begin{cases} 101.325(1 - 2.25577 \times 10^{-7}H)^{5.2559} & H < 600 \\ 101.325 - 0.01153H & 600 \leq H < 1200 \\ 99.436 - 0.01H & H \geq 1200 \end{cases} \quad (28)$$

For each city, we analyzed a typical year comprehended of 8760 hourly values. The initial values were the dry-bulb temperature and the humidity ratio for each hour value of the set of climate values.

Chapter 3 Nanofluids model

In this chapter, we review the considerations made to define the numerical model of nanofluids in a helical coil heat exchanger (HCHE). First, we describe the characteristics of helical coils and then we enumerate the assumptions considered to simulate these systems. In the mathematical model, there are remarks about how the model was set-up in the software Ansys Fluent. Even though, the remarks center its attention in the mathematical model rather than how to set up in Fluent. At the end of the chapter, we present the cases studied, establishing with the detail all the characteristics of the simulation and geometries.

3.1 Model description

The device considered in this model is a helical coil heat exchanger (HCHE). We only consider the control volume of the helical coil (HC) without including the wall of the tube. The heat transfer phenomenon occurs between the fluid inside the helical coil (control volume) and a uniform temperature boundary condition. The fluid would enter the HC at a uniform temperature and velocity. Moreover, we are interested in varying four parameters:

1. Geometry
2. Fluid regime
3. Nanofluid (base fluid and nanoparticle)
4. Nanoparticle volume concentration

In the following sections, we explain the general model, and describe the characteristics of performed experiments.

3.1.1 Physical model

The physical model is a helical coil geometry. The representative dimensions of this geometry are shown in Figure 19.

The dimensionless numbers and physical parameters which characterize a helical coil geometry are coil curvature (δ), dimensionless Pitch (λ), curvature (κ) and torsion (τ), defined as following equations:

$$\delta = \frac{d_t}{D_c} \quad (29)$$

$$\lambda = \frac{P}{2\pi D_c} \quad (30)$$

$$\tau = \frac{p}{p^2 + R_c^2} \quad (31)$$

$$\kappa = \frac{R_c}{p^2 + R_c^2} \quad (32)$$

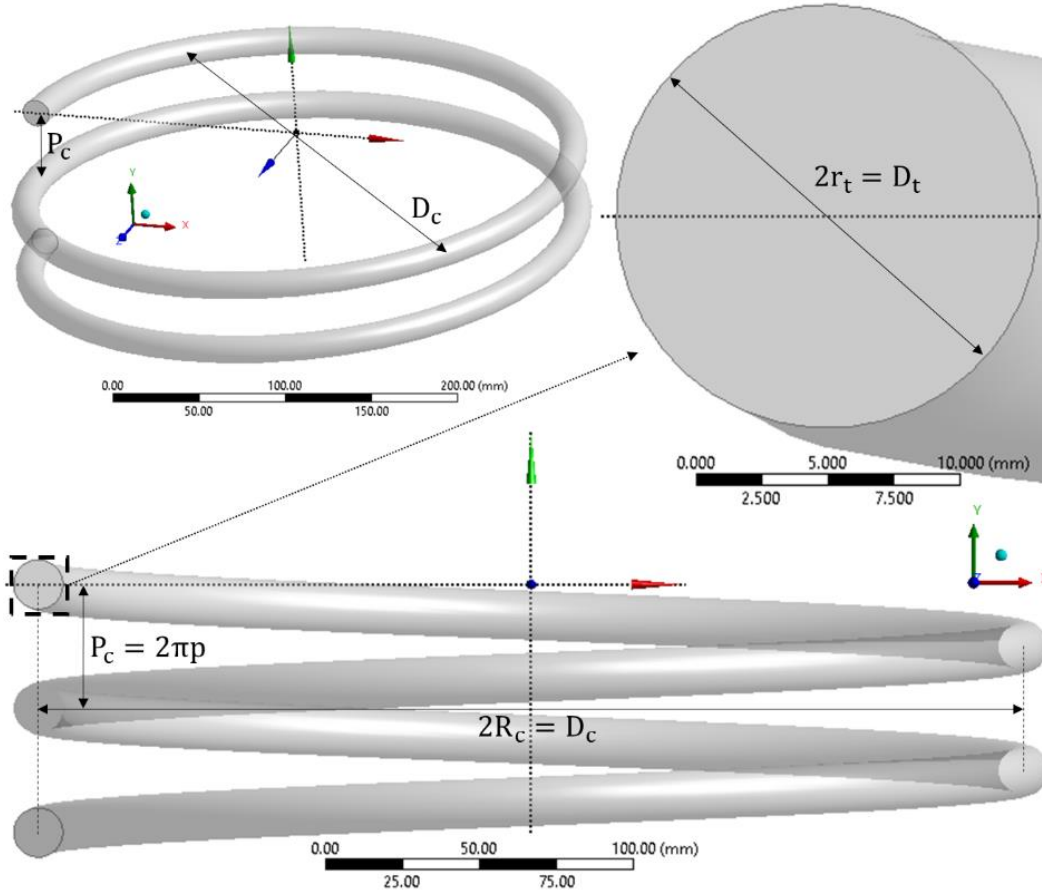


Figure 19. Helical coil physical model.

3.1.2 Assumptions

The assumptions considered for the Nanofluids model are shown in Table 12. The first three assumptions relate to considerations of the flow, typical used for fluid flow problems. The fourth assumption, negligible viscous heating, is considered from a Brinkman number ($Br = \frac{\mu u^2}{k(T_w - T_b)} < 1$) of nanofluids lower than 1 (Aydın & Avcı, 2006). Finally, assumptions sixth and seventh are characteristically of the model developed.

Table 12. Assumptions made in Nanofluid model.

ID	Assumption
1	Steady state
2	Incompressible flow
3	Uniform temperature and velocity at the inlet
4	Viscous heating is negligible
5	Nanofluids behave as single-phase fluids.
6	Nanofluids thermophysical properties depend on temperature

3.1.3 Mathematical model

The model was developed for turbulent flow regime. The turbulence model selected was the $k - \varepsilon$ Realizable with Enhanced Wall Treatment (EWT) including Thermal and Pressure Gradient effects. In the next section, we present the governing equations that Fluent solves for the turbulent regime. The complete formulation of EWT with thermal and pressure gradient effects can be consulted in section 4.14.5 in Fluent Theory Guide (ANSYS, 2013)

3.1.3.1 Governing equations for turbulent flow

Continuity

$$\frac{\partial}{\partial x}(\rho u) + \frac{\partial}{\partial y}(\rho v) + \frac{\partial}{\partial z}(\rho w) = 0 \quad (33)$$

Energy

$$\frac{\partial}{\partial x}(\rho u c_p T) + \frac{\partial}{\partial y}(\rho v c_p T) + \frac{\partial}{\partial z}(\rho w c_p T) = \left(K + \frac{c_p \mu_t}{Pr_t} \right) \left(\frac{\partial^2 T}{\partial x^2} + \frac{\partial^2 T}{\partial y^2} + \frac{\partial^2 T}{\partial z^2} \right) \quad (34)$$

Momentum (x, y, z directions)

$$u \frac{\partial(\rho u)}{\partial x} + v \frac{\partial(\rho u)}{\partial y} + w \frac{\partial(\rho u)}{\partial z} = -\frac{\partial p}{\partial x} + (\mu + \mu_t) \left[\frac{\partial^2 u}{\partial x^2} + \frac{\partial^2 v}{\partial x^2} + \frac{\partial^2 w}{\partial x^2} \right] \quad (35)$$

$$u \frac{\partial(\rho v)}{\partial x} + v \frac{\partial(\rho v)}{\partial y} + w \frac{\partial(\rho v)}{\partial z} = -\frac{\partial p}{\partial y} + (\mu + \mu_t) \left[\frac{\partial^2 v}{\partial y^2} + \frac{\partial^2 v}{\partial y^2} + \frac{\partial^2 w}{\partial y^2} \right] \quad (36)$$

$$u \frac{\partial(\rho w)}{\partial x} + v \frac{\partial(\rho w)}{\partial y} + w \frac{\partial(\rho w)}{\partial z} = -\frac{\partial p}{\partial z} + (\mu + \mu_t) \left[\frac{\partial^2 u}{\partial z^2} + \frac{\partial^2 v}{\partial z^2} + \frac{\partial^2 w}{\partial z^2} \right] \quad (37)$$

Turbulent kinetic energy equation (k)

$$\begin{aligned} \frac{\partial}{\partial x}(\rho u k) + \frac{\partial}{\partial y}(\rho v k) + \frac{\partial}{\partial z}(\rho w k) &= G_k + G_b - \rho \varepsilon + \\ \frac{\partial}{\partial x} \left[\left(\mu + \frac{\mu_t}{\sigma_k} \right) \frac{\partial k}{\partial x} \right] + \frac{\partial}{\partial y} \left[\left(\mu + \frac{\mu_t}{\sigma_k} \right) \frac{\partial k}{\partial y} \right] + \frac{\partial}{\partial z} \left[\left(\mu + \frac{\mu_t}{\sigma_k} \right) \frac{\partial k}{\partial z} \right] \end{aligned} \quad (38)$$

Turbulent dissipation rate (ε):

$$\begin{aligned} \frac{\partial}{\partial x_i}(\rho \varepsilon u_i) + \frac{\partial}{\partial x_i}(\rho \varepsilon u_i) + \frac{\partial}{\partial x_i}(\rho \varepsilon u_i) &= +\rho C_1 S \varepsilon - \rho C_2 \frac{\varepsilon^2}{k + \sqrt{\nu \varepsilon}} + C_{1\varepsilon} \frac{\varepsilon}{k} C_{3\varepsilon} G_b + S_\varepsilon + \\ \frac{\partial}{\partial x} \left[\left(\mu + \frac{\mu_t}{\sigma_\varepsilon} \right) \frac{\partial \varepsilon}{\partial x} \right] + \frac{\partial}{\partial y} \left[\left(\mu + \frac{\mu_t}{\sigma_\varepsilon} \right) \frac{\partial \varepsilon}{\partial y} \right] + \frac{\partial}{\partial z} \left[\left(\mu + \frac{\mu_t}{\sigma_\varepsilon} \right) \frac{\partial \varepsilon}{\partial z} \right] \end{aligned} \quad (39)$$

Here, it is worth to remember that viscous heating was neglected. However, there are additional terms which need a formulation¹⁵.

$$\mu_t = \rho C_\mu \frac{k^2}{\varepsilon}, \quad G_k = \mu_t S^2 \quad (40)$$

$$S \equiv \sqrt{2S_{ij}S_{ij}}, \quad S_{ij} = \frac{1}{2} \left(\frac{\partial u_j}{\partial x_i} + \frac{\partial u_i}{\partial x_j} \right) \quad (41)$$

$$G_b = \beta g_i \frac{\mu_t}{Pr_t} \frac{\partial T}{\partial x_i}, \quad \beta = -\frac{1}{\rho} \left(\frac{\partial \rho}{\partial T} \right)_p \quad (42)$$

$$C_1 = \max \left[0.43, \frac{\eta}{\eta + 5} \right], \quad \eta = S \frac{k}{\varepsilon} \quad (43)$$

$$C_{3\varepsilon} = \tanh \left| \frac{v}{u} \right|, \quad \begin{array}{l} v: \text{component parallel to gravity field} \\ u: \text{component perpendicular to gravity field} \end{array} \quad (44)$$

The constant values are

$$Pr_t = 0.85, \quad \sigma_k = 1.0, \quad \sigma_\varepsilon = 1.2, \quad C_{1\varepsilon} = 1.44, \quad C_2 = 1.9$$

3.1.3.2 Boundary conditions

These are the boundaries in the model: inlet, wall, and outlet. The values or equations for the boundary conditions are based on the variables of the experiments and values or functions that model the behavior of the variables. In this model, at the inlet boundary condition, we define temperature and velocity, which are two of the main variables we vary in the different simulations. At the wall boundary condition, we define a constant Temperature value across the different experiments; we use the no-slip condition for the velocity and an Enhanced Wall Treatment which model the behavior of k and ε at the wall and the behavior of temperature and velocity in the region near to the wall; finally, the outlet boundary condition was set up considering a hydraulically and thermally fully developed flow which means a negligible variation of variables in the normal direction of the boundary condition. The formulation and functions of the boundary conditions are shown in Table 13.

¹⁵ The main difference of the Standard $k - \varepsilon$ model with Realizable $k - \varepsilon$ model is the inclusion of the term C_μ . The term C_μ is a function of the mean strain and rotation rates, the angular velocity of the system rotation, and the turbulence fields (k and ε). Additionally, in this model include a term of rotation not included by default. For the complete formulation of C_μ and instructions to include the additional rotating term refer to section 4.3.3.3 of Fluent Theory Guide (ANSYS, 2013).

Table 13. Boundary conditions for the Nanofluid model.

Variable \ BC	Inlet	Wall	Outlet
T	$T = T_0$	$T_w = 330 \text{ K}$	$\frac{dT}{dn} = 0$
\vec{V}	$w = w_0$ $u = v = 0$	$u = v = w = 0$ (No slip)	$\frac{du}{dn} = \frac{dv}{dn} = \frac{dw}{dn} = 0$
k	$I = 0.04$ $k = \frac{3}{2}(w_0 I)^2$	EWT	$\frac{dk}{dn} = 0$
ε	$\varepsilon = c_\mu^{3/4} k^{3/2} (0.03 D_t)$		$\frac{d\varepsilon}{dn} = 0$

k from the formulation for inlet boundary condition (Aly, 2014)

ε from formulation for inlet boundary condition (Aly, 2014; Jayakumar et al., 2010)

3.1.3.3 Thermophysical properties of nanofluids

Thermophysical properties constitute an important part of every Nanofluids model. The consideration of the thermophysical properties of constant values or functions of other variables could significantly modify the results of the problem modeled. According to the assumptions made, we consider four thermophysical properties: Density (ρ), Specific Heat (c_p), Thermal Conductivity (θ) and Dynamic Viscosity (μ). These thermophysical properties depend on four variables: base fluid, nanoparticle, nanoparticle concentration (α) and temperature (T).

For the density and specific heat, we used the mixture equation given by:

$$\rho_{nf} = \alpha \rho_{np} + (1 - \alpha) \rho_{bf} \quad (45)$$

$$c_{p,nf} = \frac{\alpha \rho_{np} c_{p,np} + (1 - \alpha) \rho_{bf} c_{p,bf}}{\rho_{nf}} \quad (46)$$

In equations (45)-(46), thermophysical properties of nanoparticles ($c_{p,p}$, ρ_p) were considered constant and the thermophysical properties of base fluids ($c_{p,bf}$, ρ_{bf}) were functions of temperature. Therefore, density and specific heat of nanofluids are functions of volume concentration (α) and temperature (T). The equations for base fluids properties and values for particle properties are shown in Table 14 and Table 15, respectively.

$$\varphi(T) = A_0 + A_1 T + A_2 T^2 + A_3 T^3 \quad (47)$$

Table 14. Coefficients of equation (47) for thermophysical properties of base fluids.

Fluid	Prop	A0	A1	A2	A3	Ref
H ₂ O	ρ	8.0192E+02	1.5917E+00	-3.1000E-03		(Zonouzi et al., 2014)
	θ	-5.9810E-01	6.5300E-03	-8.3540E-06		
	μ	3.1767E-02	-2.3999E-04	6.1953E-07	-5.4398E-10	
	c_p	4.6319E+03	- 1.4780E+00	-3.1780E-03	1.1105E-05	(Jayakumar et al., 2010)
EG	ρ	9.9205E+02	9.9016E-01	-2.4316E-03		(ASHRAE, 2001)
	θ	2.1489E+03	3.8607E+00	-7.1608E-18		
	c_p	-1.4895E-01	2.8772E-03	-3.6538E-06		
	μ	6.3497E-01	-5.5687E-03	1.6389E-05	-1.6155E-08	
Oil	ρ	1.0535E+03	-6.5000E-01			(MultiTherm, 2018)
	θ	6.2713E+02	4.5300E+00			
	c_p	1.5522E-01	-7.2000E-05			
	μ	2.9127E+01	-2.5634E-01	7.5313E-04	-7.3833E-07	

In contrast with density and specific heat, the thermophysical properties of thermal conductivity and viscosity for nanofluids do not follow the mixture equation. Therefore, significant efforts towards defining correlations to estimate the values of thermal conductivity and viscosity has been made (Gupta et al., 2017; Hassani et al., 2015). In this study, we use the equation (48) (Patel et al., 2010) to estimate the thermal conductivity of nanofluids.

Table 15. Nanoparticles thermophysical properties.

Nanoparticle	ρ	c_p	θ	d_p	Source ρ, c_p, θ	Source d_p
CuO	6500	533.6	20	31	(Murshed, 2011)	(Patel et al., 2010)
TiO ₂	4157	710	8.4	12.5		(Mahmoudi et al., 2017)
Al ₂ O ₃	3970	765	46	53		(Vajjha & Das, 2009)
ZnO	5600		13	29	(Vajjha & Das, 2009)	

$$\theta_{nf} = \theta_{bf} \left(1 + 0.135 \left(\frac{\theta_p}{\theta_{bf}} \right)^{0.273} \alpha^{0.467} \left(\frac{T}{20} \right)^{0.547} \left(\frac{100}{d_p} \right)^{0.234} \right) \quad (48)$$

In equation (48), temperature (T) is in degree Celsius (°C) and d_p is the nanoparticle diameter in nanometers.

The dynamic viscosity (μ) was calculated from the equation (49) (Corcione, 2011).

$$\mu_{nf} = \frac{\mu_{bf}}{1 - 34.87 \left(\frac{d_p}{d_f} \right)^{-0.3} \alpha^{1.03}} \quad (49)$$

In equation (50), d_f is the equivalent diameter of a base fluid molecule.

$$d_f = 0.1 \left(\frac{6M}{N\pi\rho_{fT_0}} \right)^{1/3} \quad (50)$$

where M is the molecular weight of the base fluid (kg/kmol), N is the Avogadro Number, and ρ_{fT_0} is the base fluid density at reference temperature T_0 ($T_0 = 273$ K). Values used for d_f , M , and ρ_{fT_0} are showed in Table 16.

Table 16. Values and input values for equation (50).

Fluid	d_f (m)	M (kg/kmol)	ρ_{fT_0} (kg/m ³)
Water (H ₂ O)	8.74E-10	18.01528	1001.0
Ethylene Glycol (EG)	1.90E-09	40.04264	1071.2
Oil	2.28E-08	446	859.85

Finally, thermophysical properties of nanofluids were estimated using equations (45)-(50). For each nanofluid and concentration, a set of 4 thermophysical properties was found from a second order polynomial regression of values calculated from above mentioned equations. The values for nanofluid composed of water as base fluid and alumina as nanoparticle at 1% volume concentration are shown in Table 17. A complete set of coefficients are shown in Appendix C.

Table 17. Coefficients of equation (47) for thermophysical properties of Water/Alumina at 1% vc.

Nanofluid	Conc	Prop	R2	A0	A1	A2
Water / Alumina	1%	ρ	100%	833.6	1.5758	-3.07E-03
		c_p	100%	4780.1	-4.3272	6.53E-03
		θ	100%	-1.1968	9.87E-03	-1.24E-05
		μ	100%	0.016747	-8.90E-05	1.21E-07

Complete set of equations for all nanofluids simulated is showed in Appendix C.

3.2 Case analysis description

We conducted a case analysis by varying four variables of the nanofluids model. The variables and values selected are reported in Table 18.

Table 18. Different values for each variable for the case analysis.

Variables	Base	V1	V2	V3	V4	V5	V6	V7	V8	V9
De	7k	3k	5k	7k	10k	-	-	-	-	-
α	1%	0.50%	1.00%	2%		-	-	-	-	--
Geo	G7	G1	G2	G3	G4	G5	-	-	-	-
NF BF	H₂O	H ₂ O	H ₂ O	H ₂ O	EG	EG	EG	Oil	Oil	Oil
NF NP	Al₂O₃	Al ₂ O ₃	CuO	TiO ₂	Al ₂ O ₃	CuO	TiO ₂	Al ₂ O ₃	CuO	TiO ₂

NF BF: Base fluid of Nanofluid, NF NP: Nanoparticle of Nanofluid

* Dimensions of geometries used are shown in Table 17.

Columns refers to the value vary for each variable row.

Dimensions of geometries used in the case analysis of the nanofluids mode are showed in Table 19.

Table 19. Dimensions of the seven geometries studied.

Geometry ID	D _t (mm)	D _c (mm)	P _c (mm)	δ	λ
G1	16	320	40.21	0.05	0.04
G2	16	320	100.53	0.05	0.10
G3	16	160	100.53	0.10	0.20
G4	16	106.7	67.04	0.15	0.20
G5	16	106.7	33.52	0.15	0.10
G6	16	160	20.11	0.10	0.04
G7	16	160	50.27	0.10	0.10

The above values were selected from the comparison of different studies for the values of δ and λ . The graphical comparison of the geometries studied by a selection of different authors is shown in Figure 20.

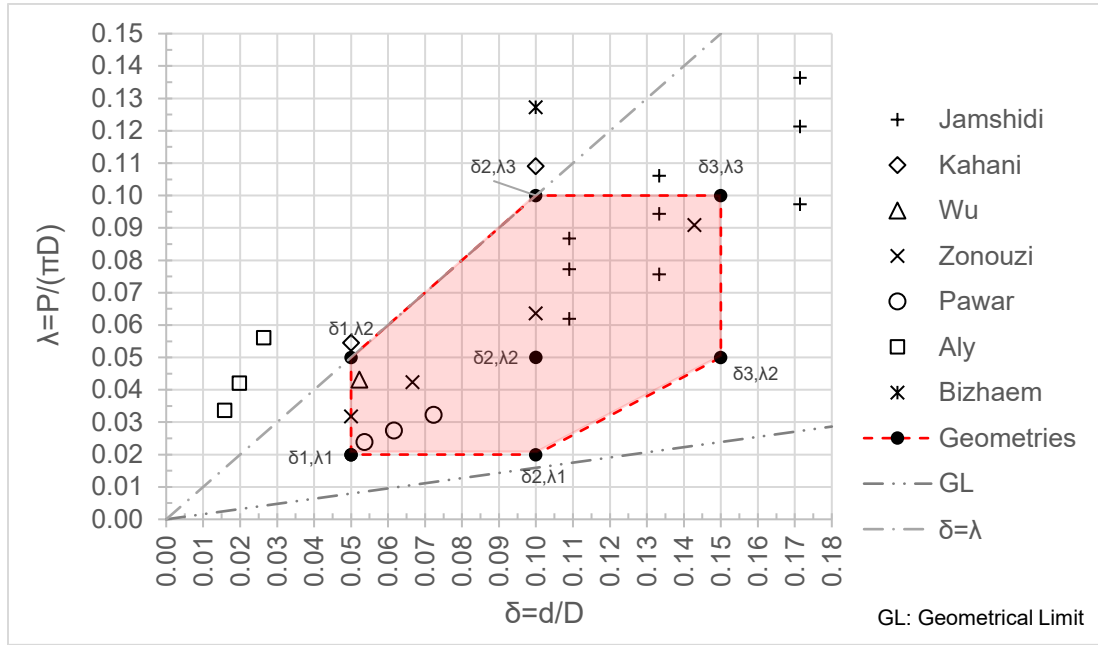


Figure 20. Geometries studied in different studies (Aly, 2014; Bizhaem & Abbassi, 2017; Jamshidi et al., 2012; Kahani et al., 2013a; Pawar & Sunnapwar, 2014; Wu et al., 2013; Zonouzi et al., 2014).

In Figure 20, the geometries were selected to comprehend most of the geometries studied. There are two lines which part from the origin. The GL line is the geometrical limit. This limit is established from the physical reason that Pitch dimension cannot be lower than the tube's diameter of the helical coil. The other line is given by the function of $\lambda = \delta$.

The next variable to select its values was the base fluid. Base fluids were selected according to their Prandtl number - equation (51). A heat transfer oil (MultiTherm, 2018) was selected for the high Prandtl number, while an aqueous solution of ethylene glycol (EG)/water at 50:50 (ASHRAE, 2001) was selected for the medium Prandtl number. Finally, water was selected for the low Prandtl number due to its lowest value comparative with the other base fluids and its use in most of nanofluids studies.

$$Pr = \frac{\mu c_p}{\theta} \quad (51)$$

The next variable studied was the Dean number, which is a variation of Reynolds number for helical coils. The equations of Dean and Reynolds number are shown in equations (52) and (53).

$$Re = \frac{\rho U_{avg} D_t}{\mu} \quad (52) \quad De = Re \sqrt{\delta} \quad (53)$$

There were selected four values of Dean number to analyze its effect in helical coils. The values selected for the Dean numbers were 3 000, 5 000, 7 000, and 10000.

Finally, according from the literature review, there were considered *low* values of volume concentration. The concentration values used for this study were three: 0.5%, 1% and 2%. However, to have an intermediate point when we evaluate the effect of concentration. There were defined the thermophysical properties of water / alumina at 1.5% vc. A summary of the different variables of the simulations is showed in Table 20.

Table 20. Summary of different values used in simulations.

Geometry	Nanofluid BF / NP	De Dean number	α Vol. Concentration
G1 $D_c=320\text{mm}$, $P_c=40.21\text{mm}$	H₂O / Al₂O₃	3 000	0.5%
G2 $D_c=320\text{mm}$, $P_c=100.53\text{mm}$	H ₂ O / CuO	5 000	1.0%
G3 $D_c=160\text{mm}$, $P_c=100.53\text{mm}$	H ₂ O / TiO ₂	7 000	2.0%
G4 $D_c=106.7\text{mm}$, $P_c=67.04\text{mm}$	EG / Al ₂ O ₃	10 000	
G5 $D_c=106.7\text{mm}$, $P_c=33.52\text{mm}$	EG / CuO	-	-
G6 $D_c=160$, $P_c=20.11\text{mm}$	EG / TiO ₂	-	-
G7 $D_c=160\text{mm}$, $P_c=50.27\text{mm}$	Oil / Al ₂ O ₃	-	-
-	Oil / CuO	-	-
-	Oil / TiO ₂	-	-

Values with bold letters and color filled are the base values which remains constant during most of simulations.

The case analysis consists of varying values of the reference variables (Geometry, NF, De or α). This values should be interpreted on the form that when we studied Dean number impact; geometry, nanofluid and volume concentration remain constant with the base values (G4, H₂O / Al₂O₃, 1.0%, respectively) while Dean number values studied were the ones showed in Table 20.

Chapter 4 Results analysis

In this chapter we present the results of both models: DPEC and Nanofluids in HCHE. For both models, we first show the mesh independency analysis and afterwards the validation of the model with experimental and numerical data from other authors. Then, for the DPEC model, we exhibit the results of the parametric analysis and show a further analysis of the optimal flow for the conditioning cooling capacity. In contrast, for the Nanofluids model, we present a qualitative analysis of the numerical model for a specific case and the results of the case analysis. Finally, there are reported the correlations obtained for DPEC model and Nanofluids model. The DPEC model also includes the evaluation of the numerical model for four distinct climates.

4.1 DPEC model

We classified the results of DPEC model in four analysis: (1) Mesh independency analysis, (2) Validation, (3) parametric analysis and (4) performance of the model in different climates. The first analysis refers to the optimal mesh for running the simulations, while validation refers to the comparison of the numerical results with experimental data from Pakari & Ghani (2019). The third analysis is an impact assessment of the variables within the model. The fourth analysis refers to the performance of the modeled system in four different climates.

The experimental and numerical results from Pakari & Ghani (2019) in Doha, Qatar are showed in Table 21. These results were used in first and second analysis.

Table 21. Validation values from experimental work (Pakari & Ghani, 2019).

Case	\dot{m}_d (kg/s)	\dot{m}_w (kg/s)	T_d (°C)	ω_d (—)	$T_{d,out}(^{\circ}\text{C})$ exp	$T_{d,out}(^{\circ}\text{C})$ model	ϵ_{wb} (%)
1	0.0465	0.0154	29.2	0.0109	17.9	19.3	1.239
2	0.0433	0.0193	30.0	0.0080	16.3	15.5	1.151
3	0.0648	0.0153	30.2	0.0083	19.1	20.5	0.945
4	0.0493	0.0187	30.2	0.0081	17.3	16.9	1.08
5	0.0693	0.0256	30.3	0.0091	20.2	18.8	0.934
6	0.0754	0.0130	30.4	0.0093	25.4	23.0	0.459
7	0.0450	0.0161	32.3	0.0175	24.8	24.1	1.075
8	0.0429	0.0157	35.1	0.0099	19.9	19.3	1.055
9	0.0461	0.0148	36.7	0.0117	23.1	21.3	0.971
10	0.0407	0.0150	38.1	0.0092	18.1	18.6	1.205
11	0.0655	0.0246	40.2	0.0150	24.5	25.3	1.095
12	0.0531	0.0256	42.2	0.0093	21.1	19.6	1.082
13	0.0463	0.0143	43.8	0.0113	24.2	22.9	1.019
14	0.0612	0.0255	44.1	0.0144	23.5	25.2	1.18
15	0.0435	0.0147	44.2	0.0098	20.9	20.8	1.129

4.1.1 Mesh independency

First, we ran a mesh independency analysis on the results of model 2 according to the experiments from Table 21. The parameter to modify the mesh is the number of uniform divisions. There were studied four different meshes with 10, 50, 100 and 500 divisions, equivalent to an element length (Δx) of 50, 10, 5 and 1 mm, respectively. We compared the outlet temperature of the reference mesh with the outlet temperature of the immediate coarser mesh. For example, mesh of element length $\Delta x = 10$ mm was compared with the mesh of element length $\Delta x = 50$ mm. Figure 22 displays the relative differences of the element meshes of 10, 5 and 1 mm. It can be monitored that as the element length decreases, the relative difference decreases. Based on the results presented, we select the mesh of 5 mm element length (50 divisions) to simulate the parametric analysis.

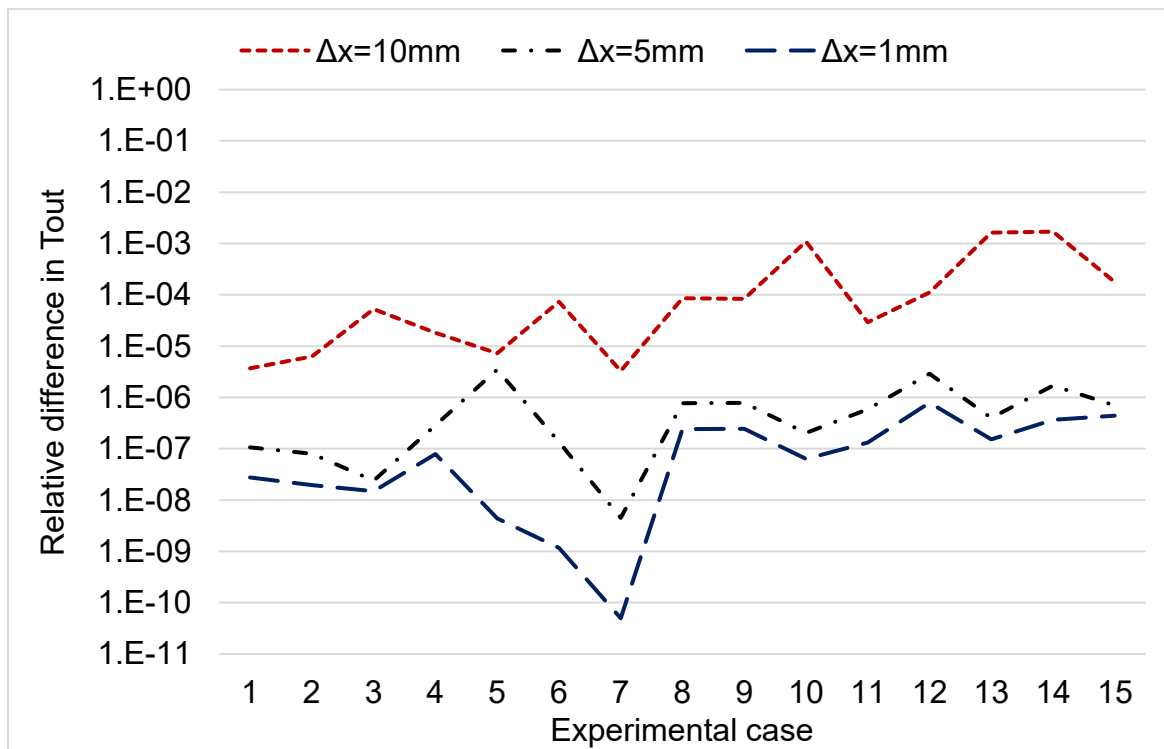


Figure 21. Mesh independency results for the outlet temperature using the Model 2.

4.1.2 Validation

Figure 22 shows the results of the developed models against the model from Pakari & Ghani (2019). The two models developed are named M1 and M2. The main difference between the models are the inclusion of thermophysical properties dependent on the temperature, humidity ratio and atmospheric pressure on the model 2, while the properties of model 1 remain constant for all situations. The

impact of variable thermophysical properties is the modification of the heat transfer convection coefficient and the mass transfer convection coefficient.

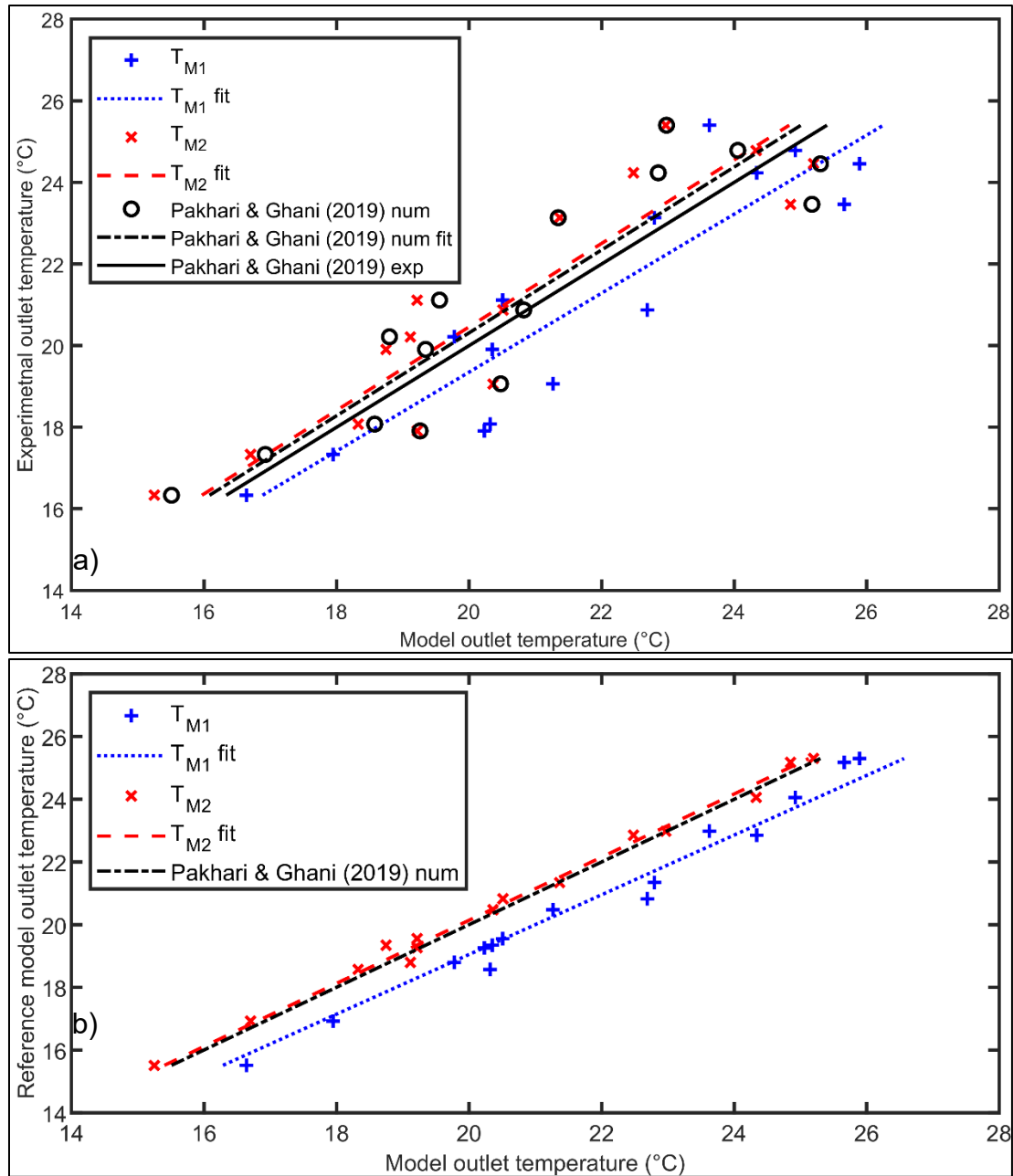


Figure 22. Comparison of outlet temperature of numerical models with experimental data (exp) and numerical model (num) from Pakari & Ghani (2019). a) Developed models (T_{M1} and T_{M2}) and numerical model against experimental data. b) Developed numerical models (T_{M1} and T_{M2}) against numerical reference model.

From Figure 22, we can observe the linear regression of both numerical models developed in this study with regard to experimental and numerical data from Pakari & Ghani (2019). We noticed that linear regression of model 2 is closer than model 1

with a slope value of about 1 ($m=1$) when is compared with the reference experimental and numerical data.

Additionally, to evaluate the distinct linear regressions, in Figure 23 we show the coefficient of determination (R^2), Root Mean Squared Error (RMSE) and slope of the fitted curves from Figure 22. From this figure, we remark the lowest RMSE, highest R^2 and nearest value slope to 1 of the Model 2 with the reference model and its remarkable results comparatively with experimental data (3 left bars of each comparison).

From the results showed in Figure 23, we will use model 2 due to its good comparative results and its feature of using thermophysical properties dependent on temperature, humidity, and atmospheric pressure.

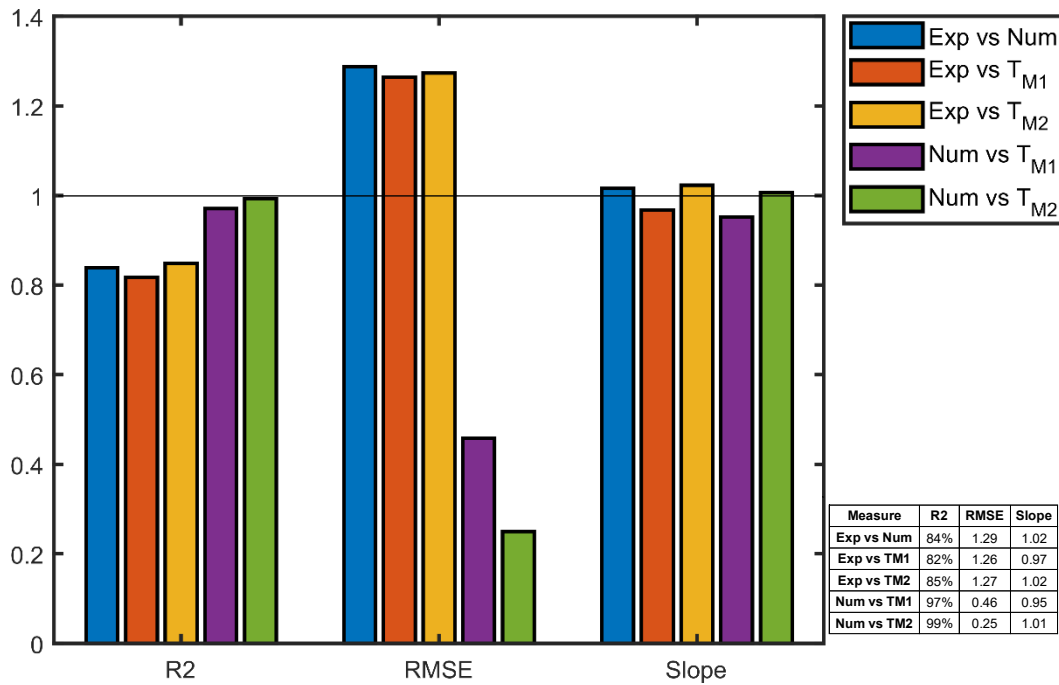
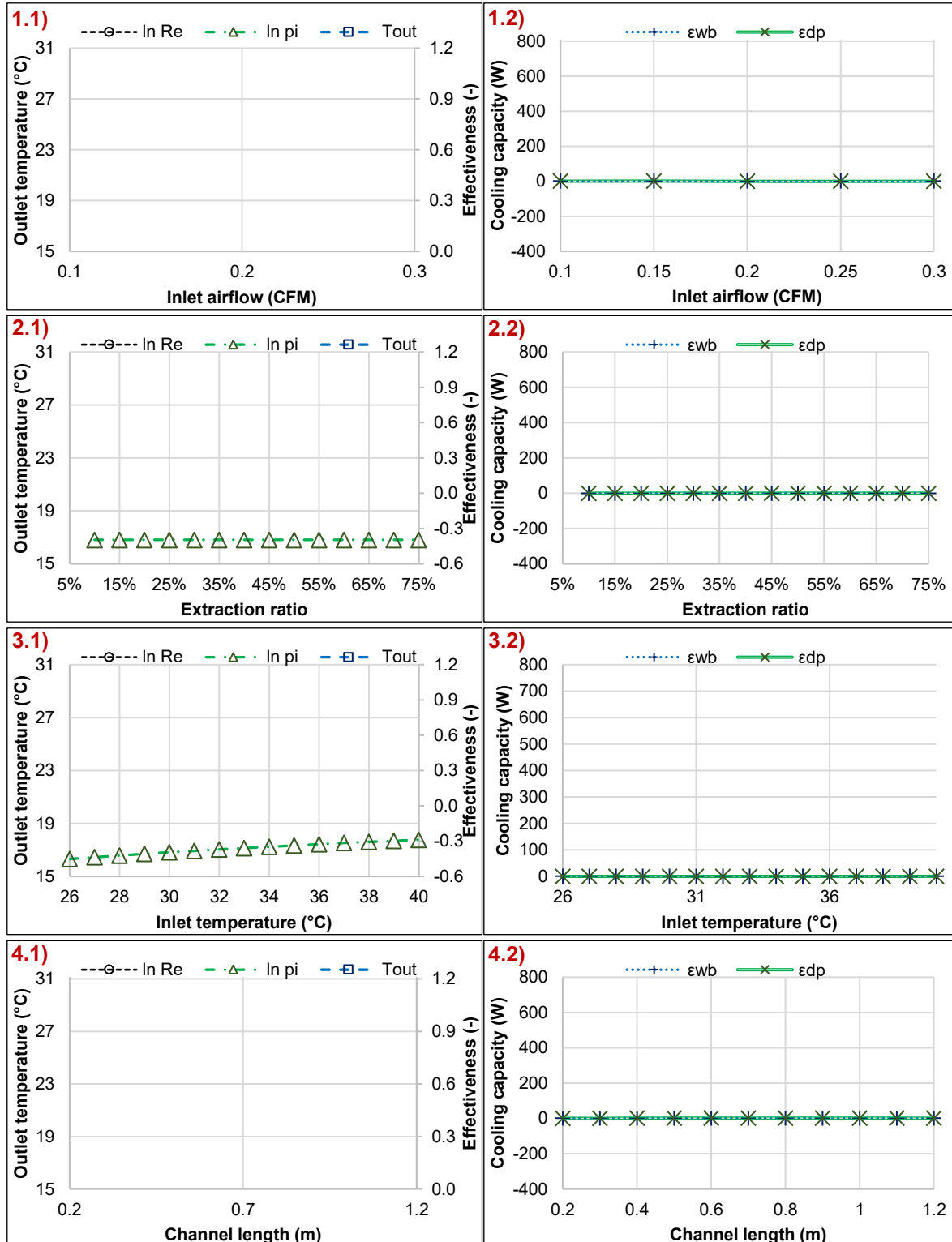


Figure 23. Coefficient of determination (R^2), RMSE and slope of the linear regression of numerical models with experimental data and numerical reference model.

4.1.3 Parametric analysis

The parametric analysis was made by modifying the variables in the range and with the base values exhibited in Table 10. For each variable modified, we present the resulting parameters of outlet temperature (T_{out}), wet-bulb effectiveness (ϵ_{wb}) and dew-point effectiveness (ϵ_{DP}) in one chart, and the results of environmental cooling capacity (\dot{Q}_{cool}) and conditioning cooling capacity (\dot{Q}_{ref}) in a second chart. In Figure 24, we show the results of the resulting parameters when six different variables were modified.

From Figure 24 we noticed different impact on the resulting parameters by the variation of the selected variables. In this point, it is important to remember that the effectiveness and cooling capacities are function of the outlet temperature.



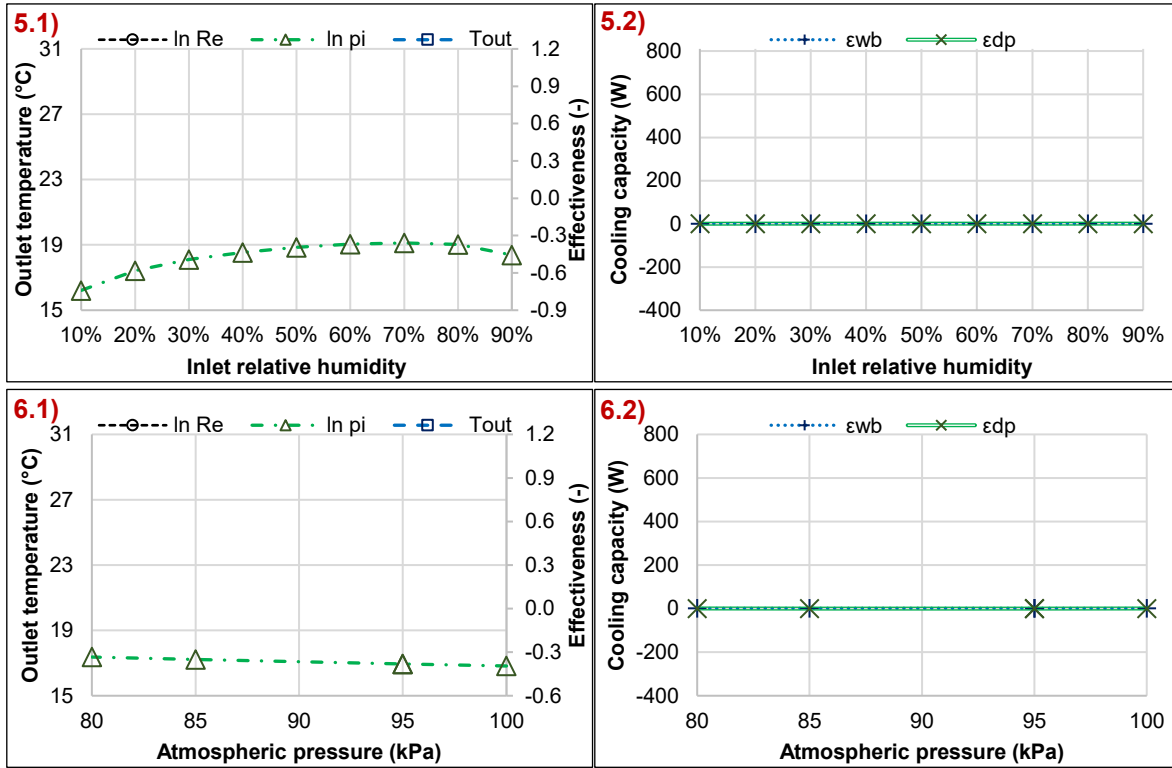


Figure 24. Resulting parameters with a variation the setting variables to modify. Right charts, series 1, show the parameters: outlet temperature (T_{out}), wet-bulb effectiveness (ϵ_{wb}) and dew-point effectiveness (ϵ_{DP}). Left charts, series 2, show the parameters: conditioning cooling capacity (\dot{Q}_{ref}) and environmental cooling capacity (\dot{Q}_{cool}). In each row formed by two charts, the variables modified are: 1) inlet airflow, 2) extraction ratio, 3) inlet temperature, 4) channel length, 5) inlet relative humidity and 6) atmospheric pressure. Base values of the runs presented were: $\dot{m}_d = 0.15$ CFM, $ER = 0.33$, $T_{in} = 30$ °C, $L = 0.5$ m, $RH = 50\%$, $P = 100$ kPa.

In the case of the inlet airflow, we are varying the volumetric airflow through the device. A higher airflow means more volume or mass of air which flows into the device in the same period. However, it also means that a differential volume of air increases its velocity and therefore its residence time into the device decrease. Hence, we observe a direct relationship with outlet temperature and environmental cooling capacity related with the decrease in residence time and increase in the mass of air, respectively. On the other hand, we observe an inverse relationship of the inlet airflow with both wet-bulb effectiveness and dew-point effectiveness, due to the decrease in the residence time. However, the relationship of the inlet airflow with the conditioning cooling capacity (\dot{Q}_{cool}) is more complex. In detail, we observe a slight increase of \dot{Q}_{cool} when the airflow increases from 0.1 CFM to 0.15 CFM, but then, after 0.15 CFM, the conditioning cooling conditioning decreases as the inlet airflow increases. In the next subsection, we further analyze the relation of inlet airflow and length of the system with the resulting parameters.

In another case, we monitor the impact of the extraction ratio variation on the resulting parameters. In this regard, as the extraction ratio increases, the wet airflow increases, and the outlet airflow decreases. From the figure, we noticed that the outlet temperature has an inverse relationship with the outlet temperature.

Particularly, given that the ambient temperature was the same, we observe that both ε_{wb} and ε_{DP} show a direct relationship with the inlet airflow. Nevertheless, the cooling capacity behave as a concave function of the inlet airflow. Both cooling capacities show a maximum in the range 0.3 – 0.35, being in agreement with previous studies (Lee et al., 2013; Liu et al., 2019; Riangvilaikul & Kumar, 2010b).

For the variation of the inlet temperature, we get very uniform relationships with the resulting parameters. Specifically, the inlet temperature shows a direct relationship with T_{out} , ε_{wb} , ε_{DP} and \dot{Q}_{cool} . The increase in each effectiveness means that the increase in T_{out} was lower than the increase in T_{wb} and T_{DP} . Yet, it is not the case for the conditioning cooling capacity (\dot{Q}_{ref}), having the inlet temperature an inverse relationship with \dot{Q}_{ref} . The behavior of \dot{Q}_{ref} with T_{in} is due to the outlet temperature is increasing. Even, the conditioning cooling capacity becomes negative when the outlet temperature is higher than the reference temperature of 25°C.

Next, the impact of the channel length in the resulting parameters is always a direct relationship, except for the outlet temperature. In this regard, given that the channel length increases, it allows that the same airflow increases its residence time and the evaporative cooling phenomenon to decrease the airflow temperature. Then, a decrease in the outlet temperature improve the other cooling variables as expected. However, the penalty in this case is due there is an increasing amount of material to build the device, which has an economic impact, which should be optimized.

Other studied impact was the produced by the inlet relative humidity. Regarding the relative humidity, it is well known that evaporative cooling devices work better in dry climates (i.e. low relative humidity). Then, it was expected a direct relationship of the relative humidity with the outlet temperature and an inverse relationship with both cooling capacities. However, the direct relationship of relative humidity with wet-bulb effectiveness show us that for dry climates the effectiveness of the device is low in comparison with more humid climates. For example, the increase in wet-bulb effectiveness from a RH of 10% to a RH of 90% goes from 88% to 95%. In contrast, the dew-point effectiveness shows a negative parabolic behavior going from a value of 42% for a RH of 10%, to a maximum value of 66% for a RH of 70% and then decreases to 60% for a RH of 90%.

Finally, we observe that atmospheric pressure has a low impact on the resulting parameters. However, it is worth to mention the direct relationship of outlet temperature with atmospheric pressure. Last means that for places with low atmospheric pressure, high altitude, evaporative cooling devices show an improved performance compared with places at sea level altitude.

The variables modified can be classified in environmental variables and design variables. The environmental variables are inlet temperature, inlet relative humidity and atmospheric pressure. The design variables are inlet airflow, extraction ratio and channel length. While the environmental variables depend on the climate, season or even the hour of the day, we are capable to set the value of the design variables. In

this regard, there are a wide consensus about the optimal value of extraction ratio, whereas there are not optimal values for inlet airflow and channel length.

In Figure 25, it can be seen the conditioning cooling capacity (\dot{Q}_{ref}) in function of the inlet airflow (\dot{m}_d) for different channel lengths (L) at inlet conditions of 30°C inlet temperature and 50% relative humidity. For the three different channel lengths, we perform a second order fit of \dot{Q}_{ref} in function of \dot{m}_d . From the second order fit, we could estimate an optimal value for a maximum conditioning cooling capacity in terms of the inlet airflow. Concerning this relation, it is worth to discuss the meaning of the conditioning cooling capacity, which is a cooling load of a specific space to maintain the reference temperature of 25°C. Unlike the environmental cooling capacity¹⁶ (\dot{Q}_{cool}), the conditioning cooling capacity could be negative. A negative value of \dot{Q}_{ref} means that the reference temperature of 25°C was not reached by the system.

Table 22. Summary of relationships between input variables and parameters from the parametric analysis.

Variable	Base	Min	Max	T_{out} [°C]	ϵ_{wb}	ϵ_{DP}	\dot{Q}_{cool} [W]	\dot{Q}_{ref} [W]
\dot{V}_{in} [CFM]	0.15	0.1	0.3	↑	↓	↓	↑	↓
ER	0.33	0.1	0.75	↓	↑	↑	↑↓ Poly2	↑↓ Poly2
T_{in} [°C]	30	26	40	↑	↑	↑	↑	↓
L [m]	0.5	0.2	1.2	↓	↑	↑	↑	↑
RH	50%	10%	90%	↑	↑	↑↓ Poly2	↓	↓
P [kPa]	100	80	100	↑	↓	↓	↑	↓

The summary of the different relationships of parameters with input variables is showed in Table 22. In the table, the arrows indicate if the parameter increases (arrow up – direct relationship) or decreases (arrow down – inverse relationship) when the input variable increases. The arrows up and down together (↑↓) indicates a

¹⁶ From the mathematical model, we observe that outlet temperature will always be lower than inlet temperature. Therefore, \dot{Q}_{cool} will always be positive.

negative parabolic behavior of the parameter variable. It means that first, the parameter value starts increasing (arrow up) until a maximum value is reached. Then, the parameter value decreases. The red color indicates a negative effect (e.g., higher outlet temperature and lower effectiveness or cooling capacity), while the blue color indicates a positive effect (e.g., lower outlet temperature and higher effectiveness or cooling capacity).

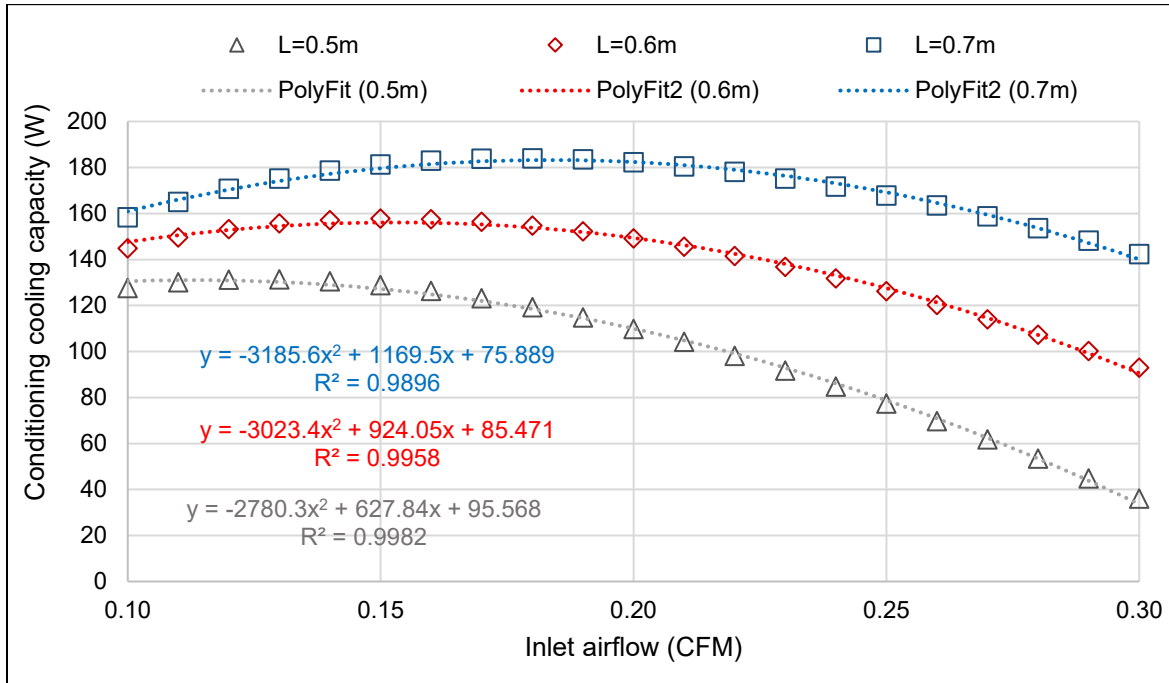


Figure 25. Conditioning cooling capacity versus inlet airflow for different channel lengths for inlet conditions $T_{in} = 30^{\circ}\text{C}$ and $\text{RH} = 50\%$.

Then, we were able to obtain the optimal airflows for the three devices (different channel lengths) at different inlet conditions. The tested inlet conditions were set by defining three values of relative humidity (40%, 50% and 60%) and three values of inlet temperature (30, 35 and 40°C). So, we realized that inlet conditions could merged into one variable: inlet wet-bulb temperature ($T_{in,wb}$). Hence, the values found of optimal inlet airflow against inlet wet-bulb temperature for the different devices are presented in Figure 26.

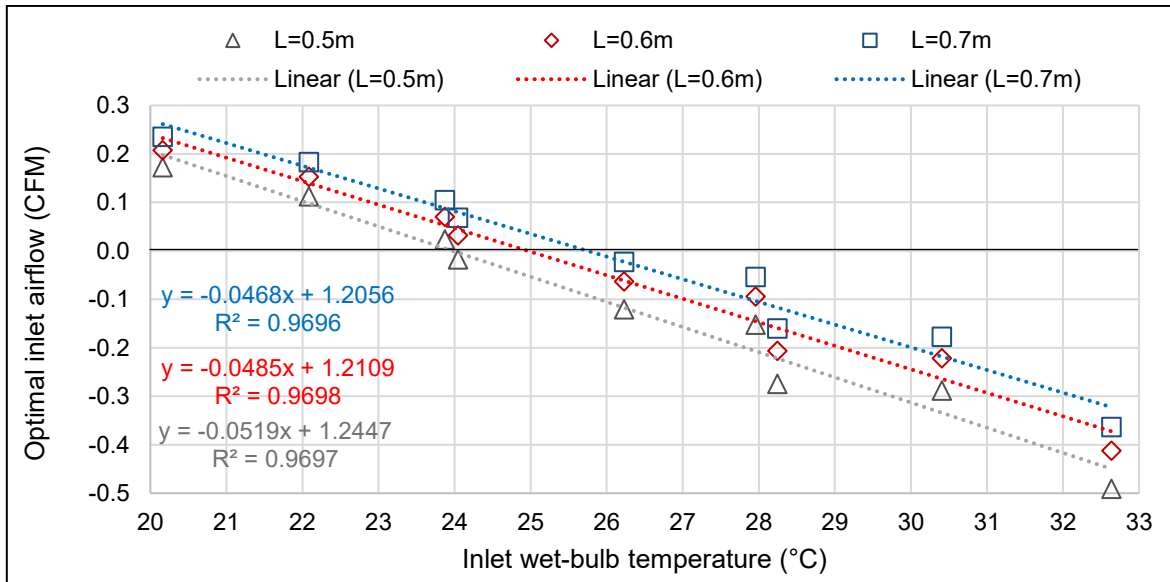


Figure 26. Optimal airflows in function of wet-bulb temperature for different channel lengths.

From Figure 26, we noticed the existence of negative optimal airflows which has not a valuable physical meaning. This physical inconsistency is based on the variable to optimize: \dot{Q}_{ref} . In consequence, a negative airflow means that comfort reference temperature was not reached. Also, it is worth to discuss that an unreached comfort temperature does not mean that the device does not remove heat from the ambient. In other words, because the device will deliver a lower temperature than the ambient temperature, a negative \dot{Q}_{ref} means that comfort temperature was not reached but it decreased the ambient temperature, and it could be useful as an auxiliary device.

Then, from the optimal airflow values, we could observe a similar linear behavior of the three devices. By performing a linear fit to each device, we can obtain the maximum wet-bulb temperature¹⁷ at which the device could supply a conditioning cooling capacity, or a cooling load to a space. The results of the maximum wet-bulb temperature for the devices are showed in Figure 27. In this point, it is important to remember the inlet temperatures were used for hot climate conditions (30 – 40°C). Therefore, it means that for temperatures above 30°C, the DPEC system should have a larger channel to reach comfort temperatures at the outlet.

¹⁷ The minimum wet-bulb temperature for a positive optimal airflow (cooling conditioning capacity). From a mathematical view, it is the interception of the curve with the x-axis.

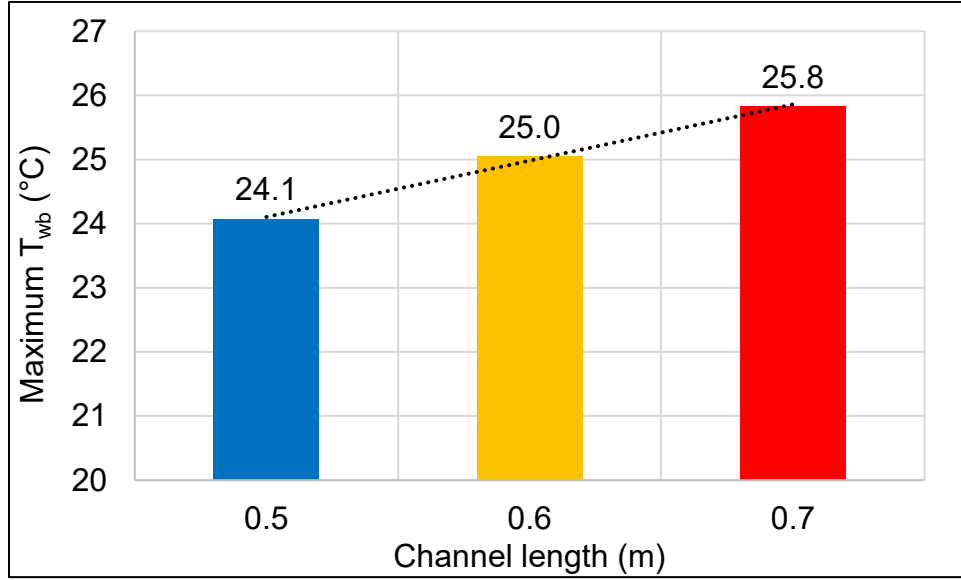


Figure 27. Maximum wet-bulb temperature for the devices studied.

We developed a dimensionless analysis of the DPEC model. The analysis made is showed in Appendix B – Dimensionless analysis. Then, we define enough input values to obtain a dataset of outlet temperatures from the DPEC model. We vary the input values of inlet temperature (26-48°C), inlet relative humidity (10-90%) and operating airflow velocity in the dry channel (0.1-0.3 CFM). The parameters of extraction ratio, channel length and atmospheric pressure remain constant for all the data points with values of 0.33, 0.5 m and 100 kPa.

We use three different forms of correlations to estimate the outlet temperature of the DPEC system. The correlations obtained are:

$$T_{out,R1} = T_{in} - 1.353(T_{in} - T_{wb,in})(1 - RH) \quad (54)$$

$$T_{out,R2} = T_{in} - 9.754(T_{in} - T_{wb,in})Re^{-0.4029}(1 - RH)^{-0.0295} \quad (55)$$

$$T_{out,R3} = T_{in} - 6.9921(T_{in} - T_{DP,in})Re^{-0.4215}(1 - RH)^{-0.0848} \quad (56)$$

It is worth to mention the term defined in this analysis as “*potential humidity*” (1-RH). This potential humidity was set on this way due to the inverse relationship of the relative humidity with the outlet temperature. The first form of the equation (54) to set the first regression ($T_{out,R1}$) was defined considering a linear relationship of the wet-bulb effectiveness with the potential humidity. Then, we realize the neediness to include the term of the third pi-number (Reynolds number, $Re = \rho V_{in} d_h / \mu$) in the second regression ($T_{out,R2}$). Finally, given the good results of the second regression, it was tried the same form with the difference of using the dew-point effectiveness instead the wet-bulb effectiveness to obtain the third regression ($T_{out,R3}$). The regression curves of equations (54), (55) and (56) are exhibited in Figure 28. The total dataset used consists in 2268 points.

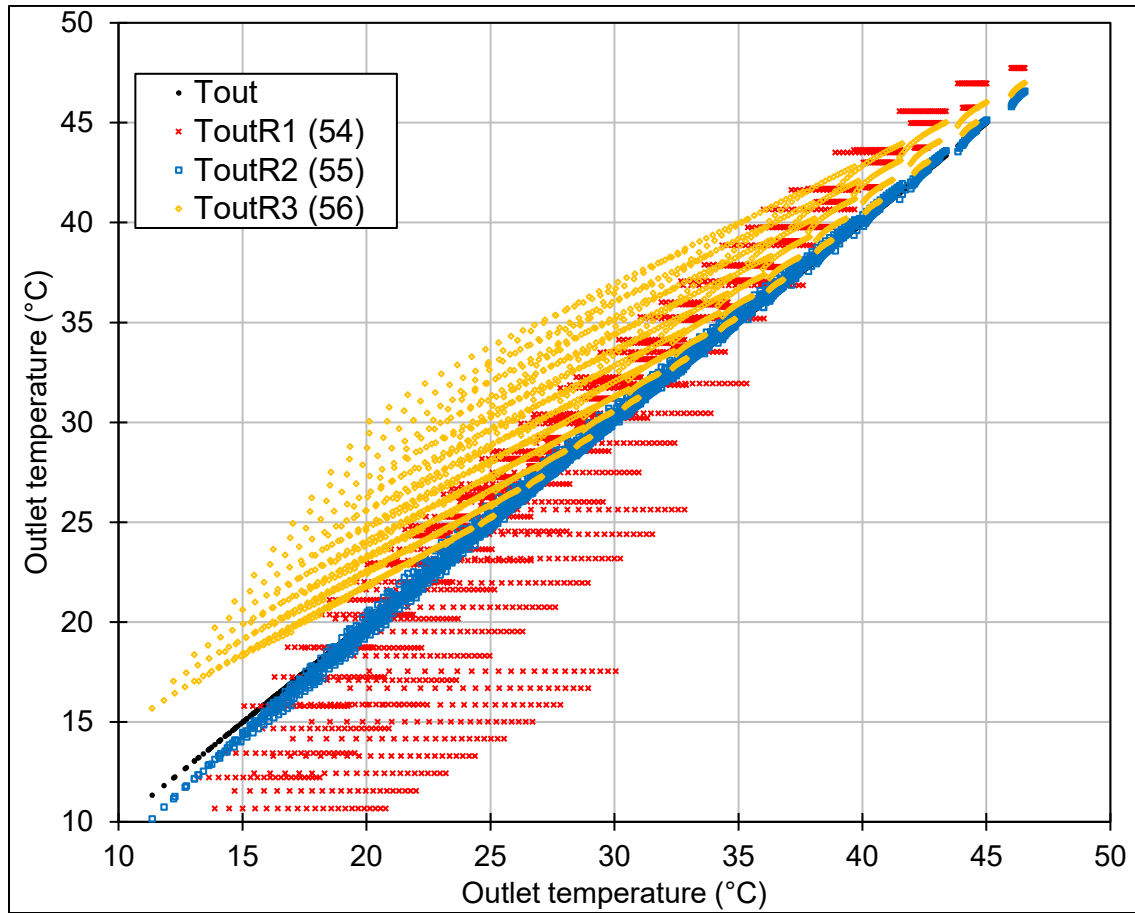


Figure 28. Regressions found to estimate the outlet temperature.

From the results above, we obtain parameters which measures the correlation between the regression curves and the results of the model. These parameters are the adjusted coefficient of determination (R_{adj}^2), the root mean square error (RMSE) and the mean absolute relative error (MARE). The regression fits better with the modeled data as the parameters approach to values of 1, 0 and 0, respectively. These parameter values for the distinct regressions are showed in Figure 29.

From Figure 29, we noticed that the second regression ($T_{out,R2}$) shown the lowest RMSE and MARE with values of 1.4 and 1.0%, respectively. This regression also shows the closest R_{adj}^2 to the unity with a value of 93%.

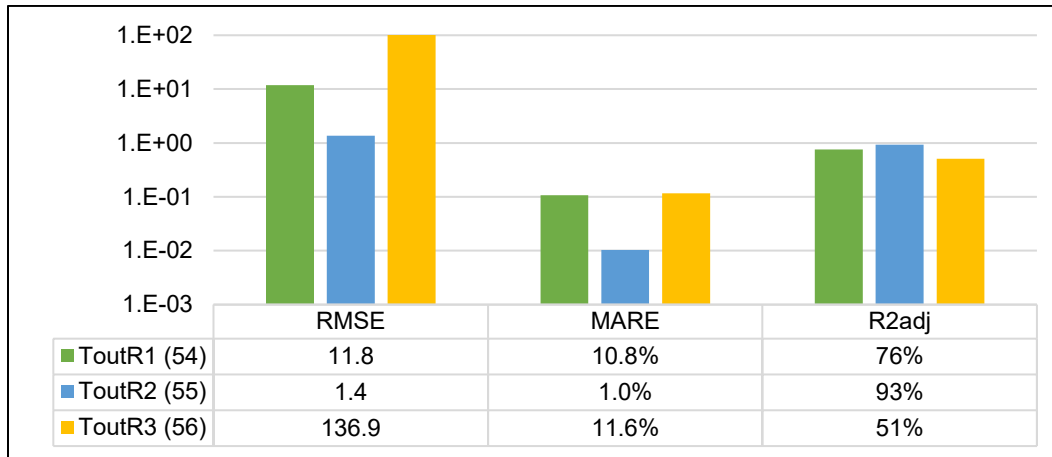


Figure 29. Parameters of the regressions found.

4.1.4 Model performance for different climates

The performance of the DPEC system with the environmental data from four meteorological stations in Mexico. As explain in section 2.2.2, the cities (or stations) were selected based on their climate classification.

The simulations were made during the values of a typical year for each city. Each city was characterized by three variables: ambient temperature, ambient relative humidity, and atmospheric pressure. Each station provides the ambient temperature and relative humidity for a typical year in an hourly resolution. The atmospheric pressure was treated as constant along all the hourly values and it was estimated from the equation (28). The same design parameters were used in all the cities. The values of the design parameters were $\dot{m}_d = 0.07 \text{ kg/s}$, $L = 0.5\text{m}$, and $ER = 0.33$.

The ambient (inlet) temperature (T_{amb}), outlet temperature (T_{out}) and the reference temperature for each city are exposed in Figure 30. We plot the ambient temperature to make visible the data points above the reference temperature (25°C).

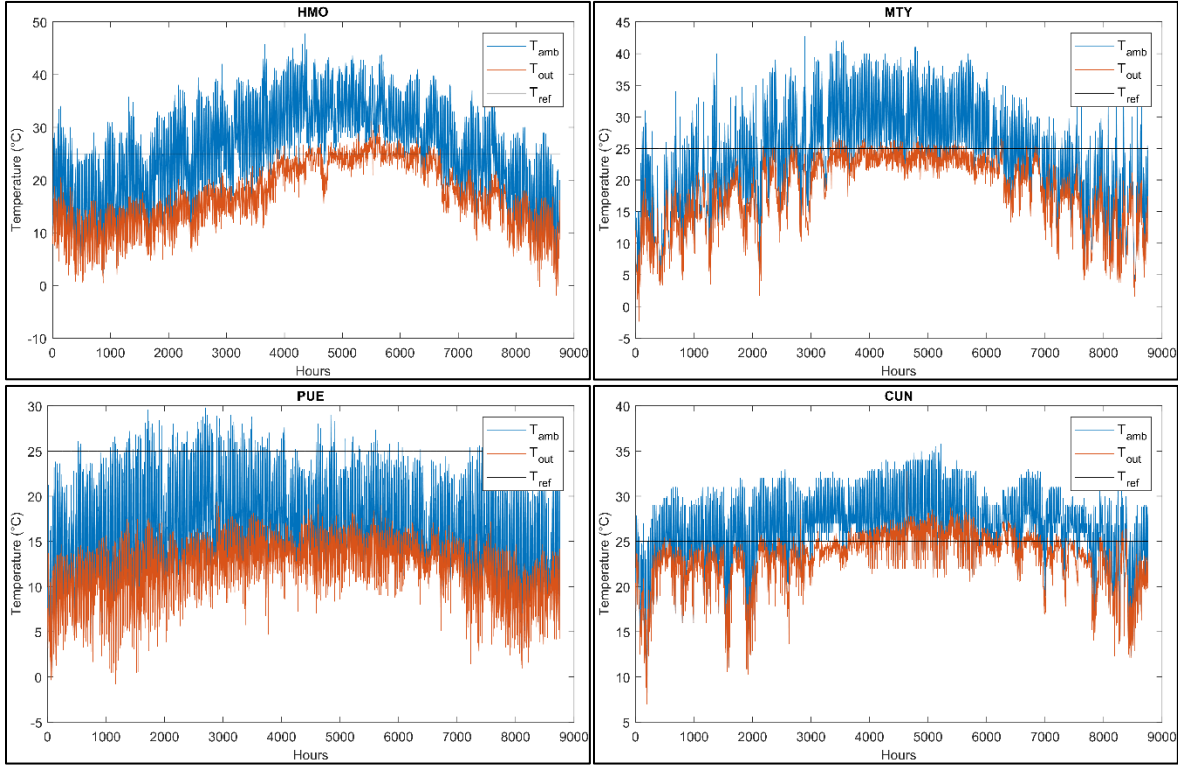


Figure 30. Ambient (inlet) temperature and outlet temperature of the DPEC system simulated. $T_{ref} = 25^{\circ}\text{C}$.

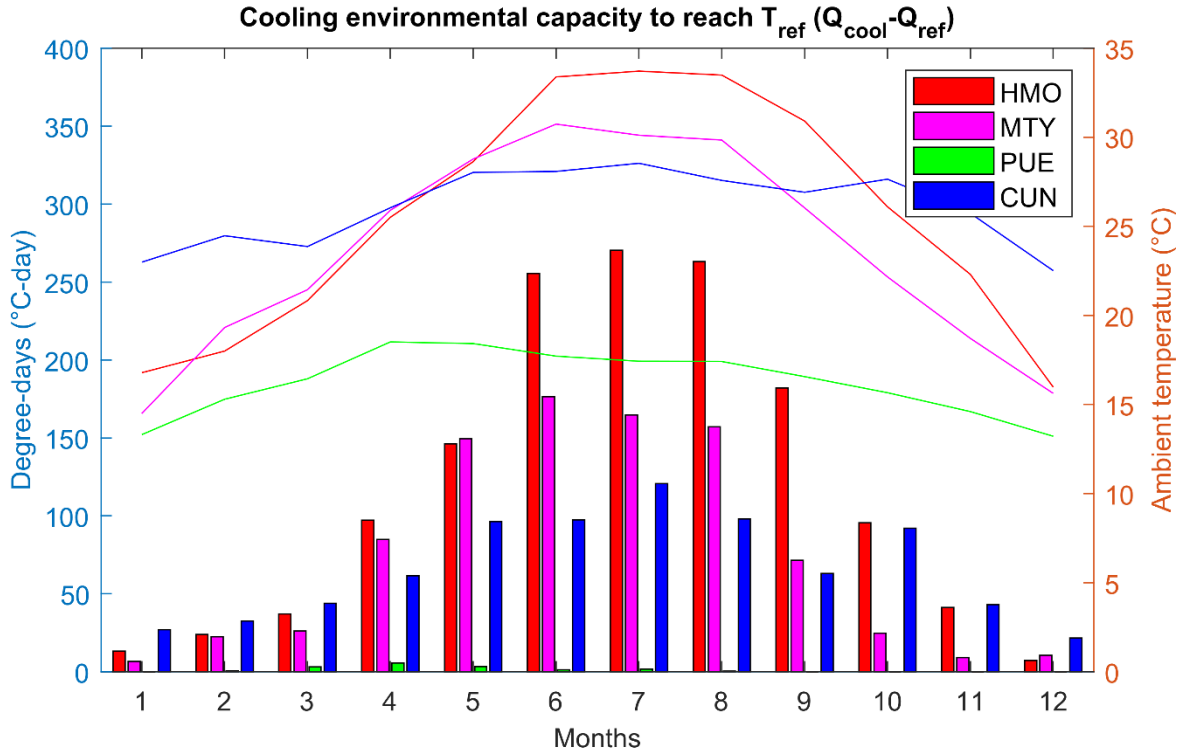


Figure 31. Sum of hourly necessary cooling capacity to reach the reference temperature ($\dot{Q}_{cool}-\dot{Q}_{ref}$) when cooling is needed ($T_{amb} > 25^{\circ}\text{C}$) and mean ambient temperature for each city per month.

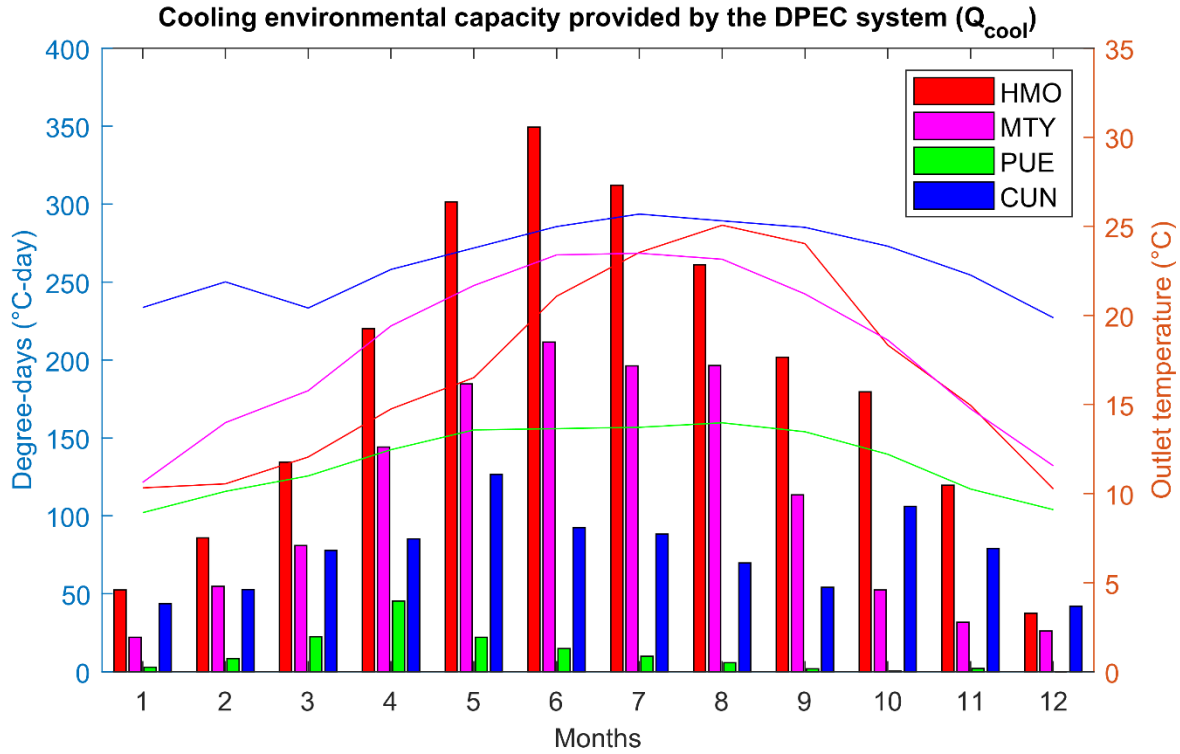


Figure 32. Sum of hourly environmental cooling capacity (\dot{Q}_{cool}) provided by the system when cooling is needed ($T_{amb} > 25^{\circ}\text{C}$) and mean outlet temperature for each city per month.

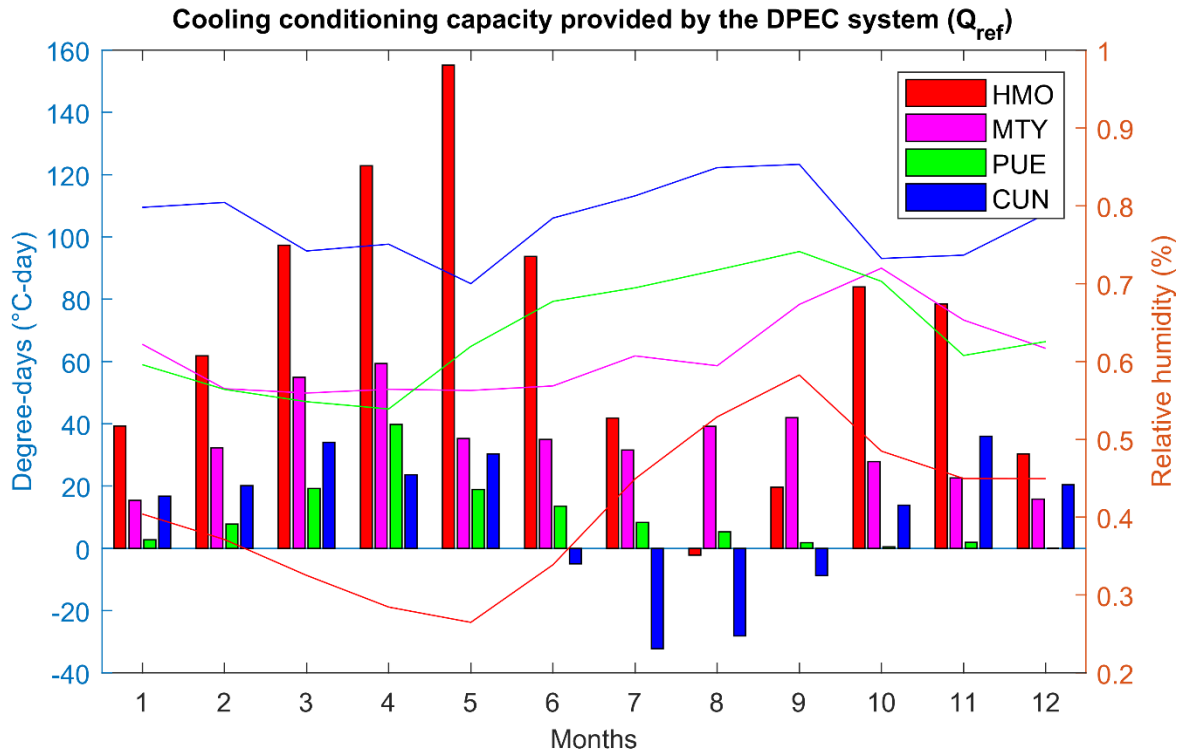


Figure 33. Sum of hourly conditioning cooling capacity (\dot{Q}_{ref}) provided by the system when cooling is needed ($T_{amb} > 25^{\circ}\text{C}$) and relative humidity for each city per month.

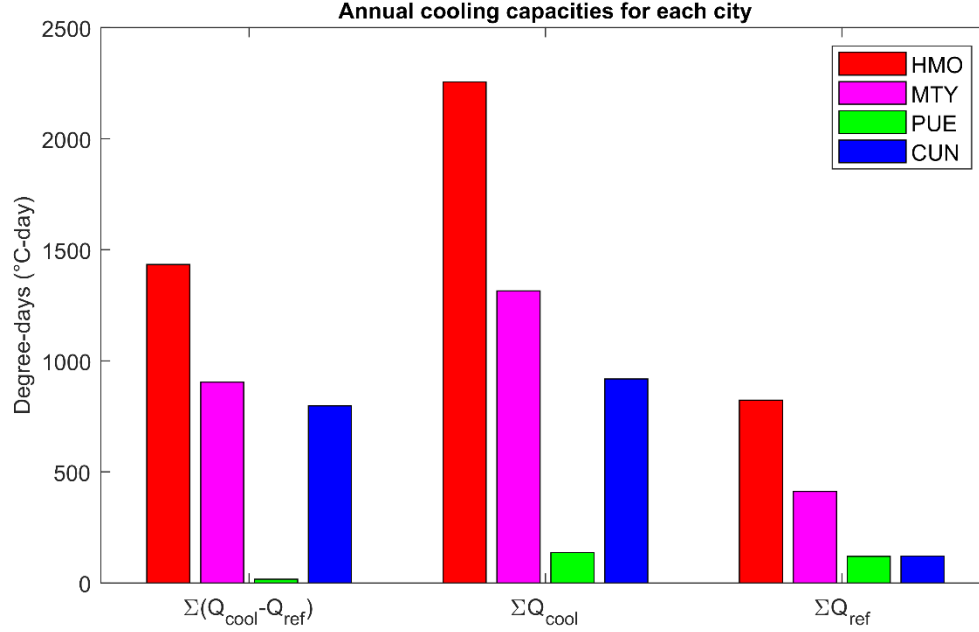


Figure 34. Sum of annual cooling capacities for each city.

In Figure 31 is exhibited the sum of the environmental cooling requirement ($\dot{Q}_{cool} - \dot{Q}_{ref}$) for each city per month. The same figure also shows the mean ambient temperature for each city. From this figure, we observe the higher environmental cooling requirements for the summer months (April to October – 4 to 10). The magnitude of this requirement is not the same for each city. For example, we could observe that the climate of Hermosillo (HMO), which has higher mean ambient temperatures also presents higher environmental cooling requirements. In contrast, Puebla which presents the lowest ambient temperatures, below the reference temperature, also has the lowest cooling requirements. It is worth to mention that the variable showed in this figure, do not depend on the system. Also, through a simple mathematical procedure we obtain that this cooling requirement in degree-days ($T_{amb} - T_{ref}$) is the difference of \dot{Q}_{cool} and \dot{Q}_{ref} as stated first.

In another example, Figure 32 shows the environmental cooling capacity (\dot{Q}_{cool}) given by the difference between the ambient temperature (T_{amb}) and the outlet temperature (T_{out}). The figure also shows the outlet temperature of the DPEC system. From this figure, we observe a slight increase (y-axis in Figure 31 and Figure 32 has the same range) in the amount of degree-days in comparison with the previous figure for Puebla station. We attribute this behavior due to the difference of the ambient temperature (see ambient temperature of month 4 in Figure 31) and the outlet temperature (see outlet temperature of month 4 in Figure 32).

Then, we calculate \dot{Q}_{ref} by making the difference operation of the environmental cooling capacity (\dot{Q}_{cool}) and the necessary environmental cooling requirement ($\dot{Q}_{cool} - \dot{Q}_{ref}$). Getting as result the conditioning cooling capacity (\dot{Q}_{ref}) showed in Figure 33. In this figure is also plotted the mean relative humidity for each city per month. One of the most remarkable features of this figure is the presence of

negative values in the months 6 to 9 (June to September) for Cancun city. These negative values appear due to the conditioning cooling capacity is lower than the necessary cooling requirement. In other words, the system is incapable to provide comfort (reach reference temperature) in average for these months. Another feature of this figure is the visible inverse relationship of \dot{Q}_{ref} with the relative humidity. This feature can be seen by comparing in relative terms for each city an increase of relative humidity and a decrease in the conditioning cooling capacity.

Finally, in Figure 34 it is presented the annual sum of required conditioning capacity (left grouped bars), environmental cooling capacity (centered grouped bars) and conditioning cooling capacity (right grouped bars). From this figure, we observe that the system shows the highest conditioning cooling capacity for Hermosillo, then Monterrey, and as a technical tie Cancun and Puebla. Last is remarkable given that Cancun has a much higher cooling requirement than Puebla, but the environmental cooling capacity (\dot{Q}_{cool}) barely supply the cooling requirement.

4.2 Nanofluids in helical coils

Before showing the results for the Nanofluids in helical coil model. There are some parameters to establish. The equations of these parameters are defined in equations (57) to (65).

$$U_{b,CS} = \frac{\int V_n dA}{A} \Big|_{CS} \quad (57)$$

$$T_{b,CS} = \frac{\int V_n T dA}{\int V_n dA} \Big|_{CS} \quad (58)$$

$$\varphi_{eff,CS} = \varphi_{nf}(T_{b,CS}) \quad (59)$$

$$\varphi_{wall,CS} = \frac{\int \varphi_{wall} dA}{dA_{wall}} \quad (60)$$

$$\Delta P_{CS} = \frac{\int V_n P dA}{\int V_n dA} \Big|_{inlet} - \frac{\int V_n P dA}{\int V_n dA} \Big|_{CS} \quad (61)$$

$$f_{CS} = \frac{8\tau_{wall,CS}}{\rho_{eff,CS} U_{b,CS}^2} \quad (62)$$

$$h_{CS} = \frac{q_{wall,CS}}{T_{wall} - T_b} \quad (63)$$

$$Nu_{CS} = \frac{h_{CS} D_t}{\theta_{wall}} \quad (64)$$

$$Nu_{avg} = \frac{1}{L} \int_0^{CS} Nu \cdot ds \quad (65)$$

In above equations, U is the axial velocity of the fluid (related to a bulk velocity), V_n is the normal velocity to the cross section, T is the temperature, dA is the differential area of the cells, φ is a property (ρ, c_p, θ, μ) or a flux of heat (\dot{q}) or shear wall (τ_{wall}), ΔP is the pressure drop from the inlet, f is the friction factor, h is the convective heat transfer coefficient, and Nu is the Nusselt number. Regarding the subscripts, CS means a cross section which could be related to a specific axial position, b stands for a bulk parameter, eff is the effective properties calculated with the bulk temperature (T_b) at a given cross section, wall refers to a heat flux or shear wall calculated in the cells adjacent to the wall.

4.2.1 Mesh independency

The mesh independency was made by building a structured mesh based on three sizing controls on the mesh volume of geometry 3 (G3). Figure 35 shows these three sizing controls.

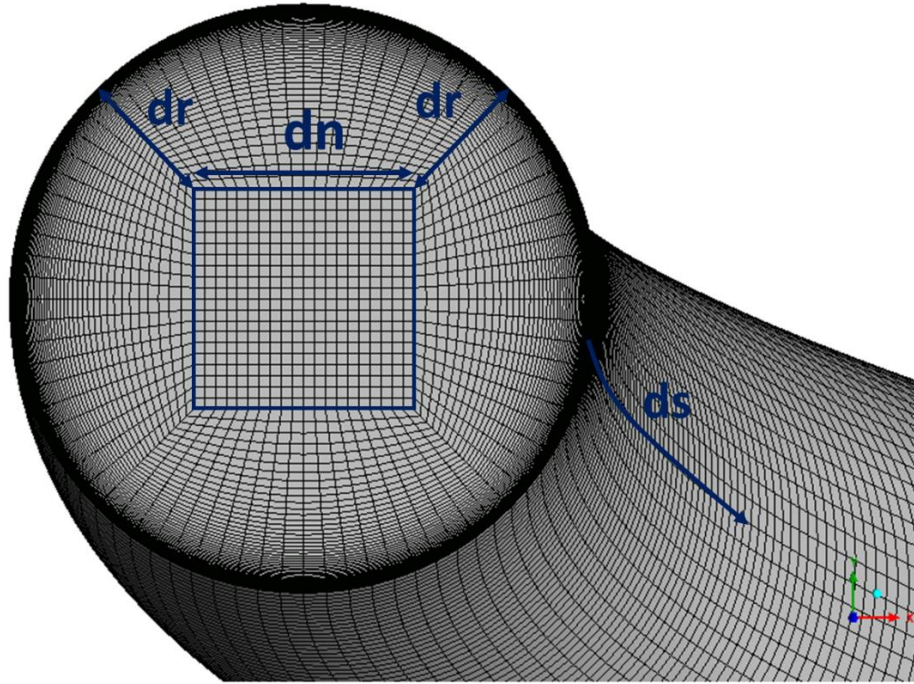


Figure 35. Mesh sizing controls used to create the different structured meshes.

There were studied seven different meshes. The mesh differences from themselves by having different number of divisions of bias factor in the mesh controls d_n , d_r and d_s . The square, with a side divided in d_n divisions, was built in such a way that its side measures $3/8$ of the diameter. Also, the center point of the square was coincident with the center point of the inlet surface (circle). For a diameter of 16 mm, the square side measures 6 mm. The values for the mesh controls used are showed in the Table 23.

Table 23. Mesh sizing controls used in the mesh independency analysis.

Sizing	Control	M1	M2	M3	M4	M5	M6	M7
Dn	# div	16	20	20	30	30	20	20
Dr	# div	18	25	31	31	31	52	52
	BF	5.0	5.0	5.0	5.0	5.0	32.0	32
ds*	# div	360	720	720	720	1440	$\leq 90^\circ$ 234 div BF 4	$\leq 90^\circ$ 360 div BF 4
ds2	-	-	-	-	-	-	$> 90^\circ$ 540 div	$> 90^\circ$ 1080 div
Number of elements		507 k	1.728 M	2.074 M	3.326 M	6.653 M	3.529 M	6.566 M

* If there is only one mesh control, it applies to the whole range of 2 turns.

It is remarkable from Table 23 that mesh 6 and 7 show a smaller number of elements than Mesh 5. However, both meshes (M6 and M7) has more elements in the dr sizing control. This modification was implemented after calculating the normal height of the nearest element to the wall. The modification follows the goal that the first near-wall node is placed at $y^+ = 1$ (resolving the viscous sublayer). The characteristic of a fine mesh near the wall allows Fluent to improve its accuracy by using a two-layer zonal model (viscosity affected region and fully turbulent region).

The results for the mesh independency are showing next. As in the DPEC model section. Here, the results of the MeshN reflects the comparison with the immediate coarser mesh. In other words, the results of the Mesh 3 are by comparing the Mesh 3 with the Mesh 2 (immediate coarser mesh). The comparison of Mesh 6 was made with Mesh 4 because this mesh was the immediate coarser mesh. There were calculated the average Nusselt. The relative differences of the mesh compared to the immediate coarser mesh are showed in Figure 36.

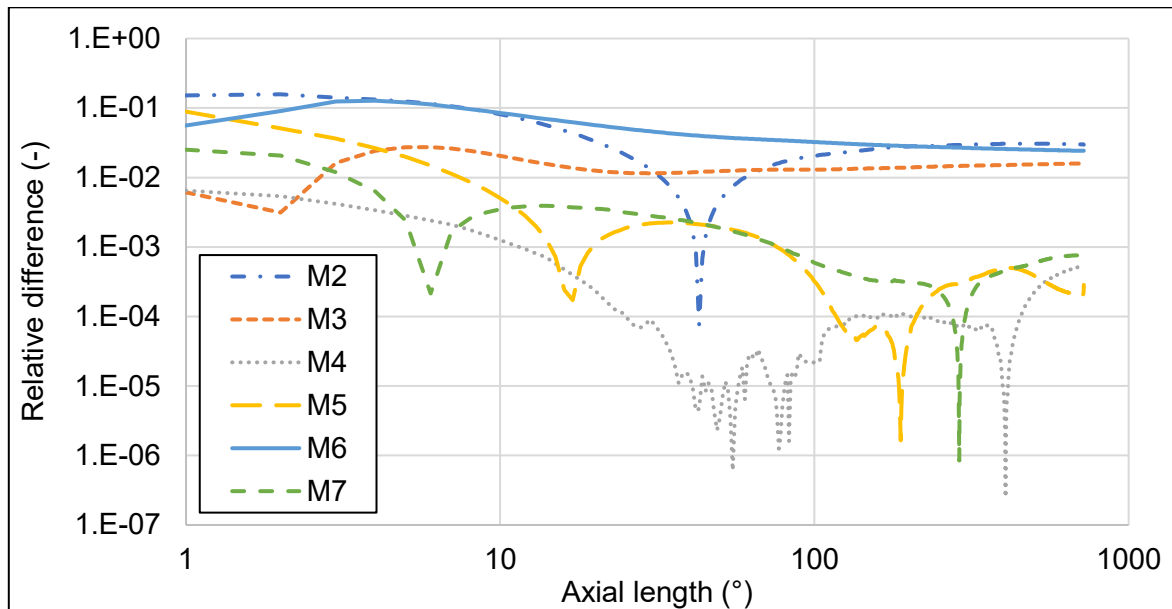


Figure 36. Relative differences of the meshes compared to the immediate coarser mesh.

The fact that the curve approach to 1 means a higher error. Therefore, error parameters were calculated for the different comparisons of meshes in the whole range of the two turns. Absolute Mean Errors (AME) and Relative Mean Squared Errors (RMSE) are showed in the upper side of Figure 37. Then, in the bottom side of Figure 37, there are exhibited the parameters of Relative Absolute Error (RAE) and Relative Root Squared Error (RRSE).

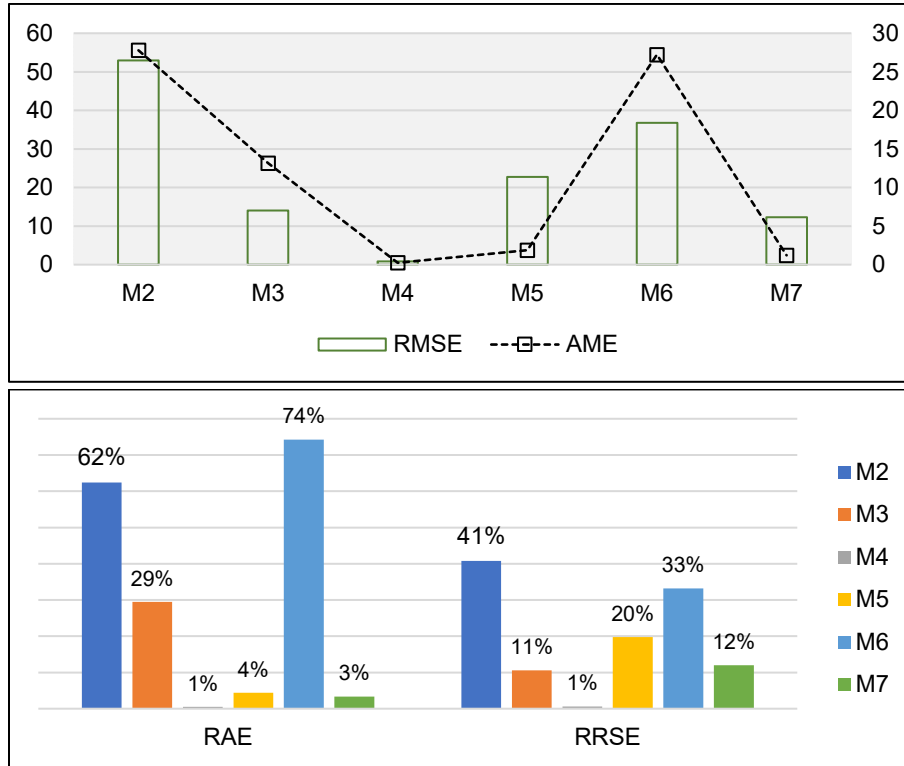


Figure 37. Calculated error parameters of the mesh with the immediate coarser mesh,

From Figure 37, it is visible that Mesh 5 showed an increase in error (it change its Nusselt average value (Nu_{avg}) in comparison with Mesh 4. Then, because Mesh 5 increases its axial divisions in comparison with Mesh 4, we built Mesh 6 increasing the axial division and using less the same dn elements than Mesh 3. Also, the refinement as stated before of dr control was made to reach the viscous sub-layer and increase the accuracy of the EWT used in the wall. Though, M6 show higher errors, then, Mesh 7 which has almost two times the elements of Mesh 6, shows very low errors. Indeed, the errors diminish significantly if average Nusselt at the entrance (axial position of 0 degrees) is not considered. The values without considering the inlet surface are 0.8, 2.8, 2.3% and 3.2% for parameters AME, RMSE, RAE and RRSE, respectively. From the analysis above, Mesh 6 was selected as the Mesh to run all the simulations. It is worth to remember that it accomplishes a near-wall node inside the viscous sub-layer with the sufficient precision in the results.

4.2.2 Validation

The results of the coil 4 of a previous experimental and numerical study (Rakhsha et al., 2015) were selected to develop the validation process. Coil 4 has a tube diameter of 8 mm, coil diameter of 110 mm and Pitch of 20 mm. The nanofluid used by them was Water / CuO at 1% volume concentration. The inlet conditions were uniform. While the inlet velocity varies depending on the Reynolds number, the

temperature was set at 300 K and the wall temperature was set at 373 K. The results of the validation are showed in Figure 38.

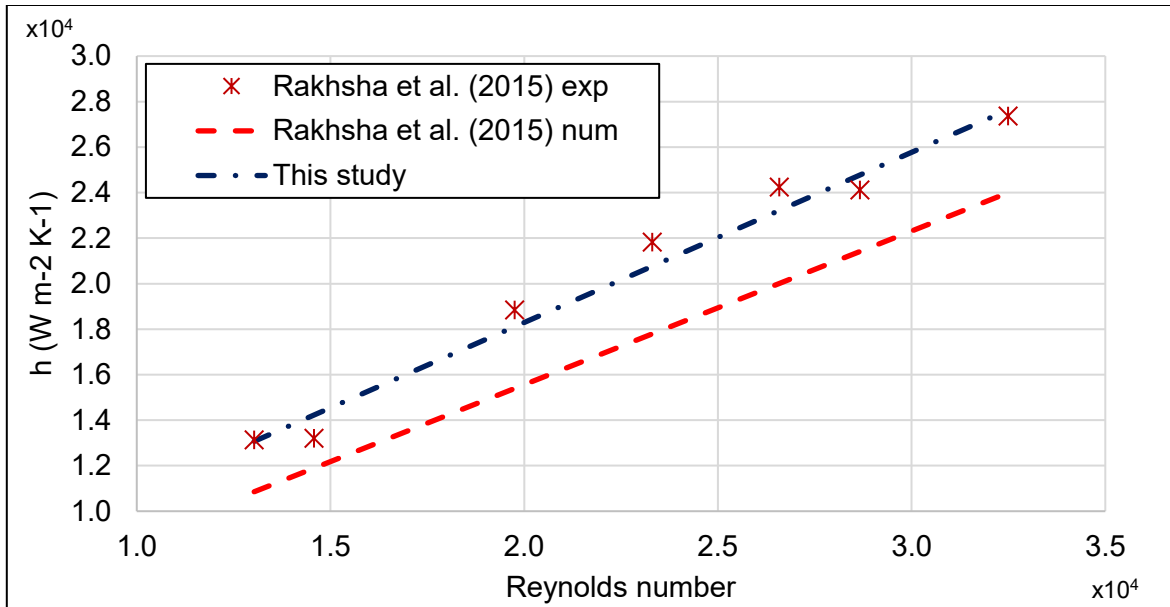


Figure 38. Validation of the convective heat transfer coefficient with experimental and numerical values (Rakhsha et al., 2015).

From Figure 38, we observe the simulations results of this study and the experimental and numerical results from Rakhsha et al. (2015). The error parameters, RMSE, MAE and MARE between the experimental values and the values found by the simulations of this study are 924, 965 and 5%, respectively.

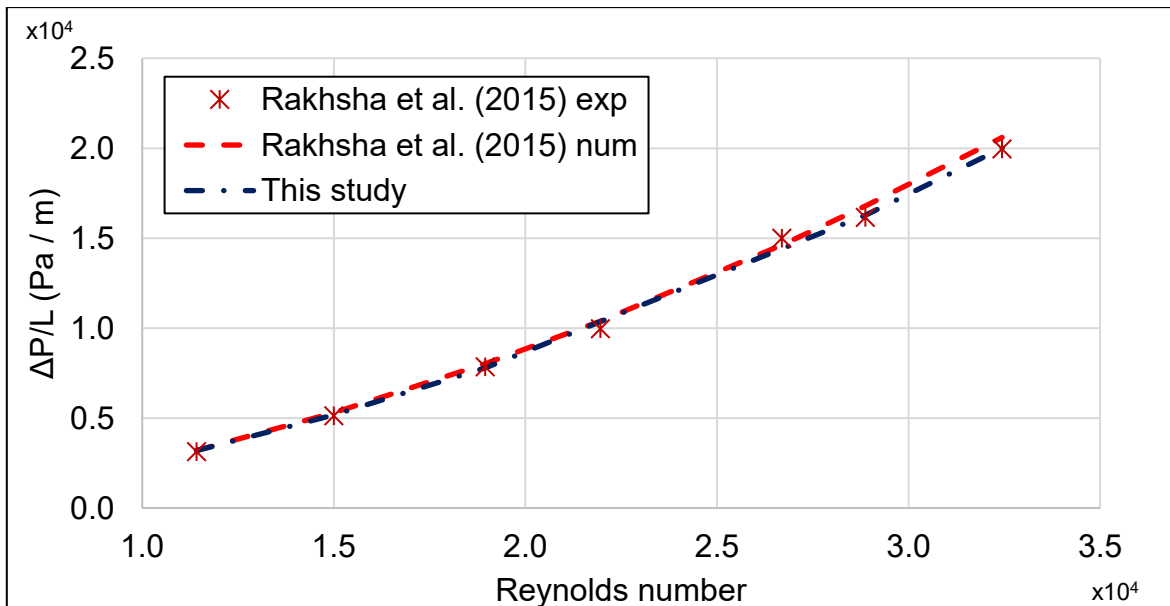


Figure 39. Validation of the pressure drop with experimental and numerical values (Rakhsha et al., 2015).

Similarly, to the convective heat transfer coefficient, we compare the pressure drop per unit length found with the experimental and numerical results from Rakhsha et al. (2015). From Figure 39 we observe a slight improvement of the results found with the experimental data reported. The RMSE, MAE and MARE found of the simulations carried on with the experimental data are 80, 74 and 0.74%, respectively.

From the above results, we validate that our model reproduces the nanofluids heat transfer phenomena in helical coils. Therefore, we perform a series of case analysis by varying the geometry, the nanofluid (fluid base and nanoparticle), Dean number (Reynolds multiplied by square root of the curvature ratio) and concentration of the nanoparticle. The results are presented in the following section.

4.2.3 Qualitative analysis

Figure 40 shows the contours of dimensionless temperature and dimensionless velocity at different axial positions. From the contours, the higher dimensionless temperatures and velocities are moving outside the helical coil due to centrifugal force which experiments the fluid in the geometry. It is worth to mention that inlet temperature and velocity is uniform. Here, the formulation of the dimensionless temperatures refers to the difference of the wall temperature to the node temperature.

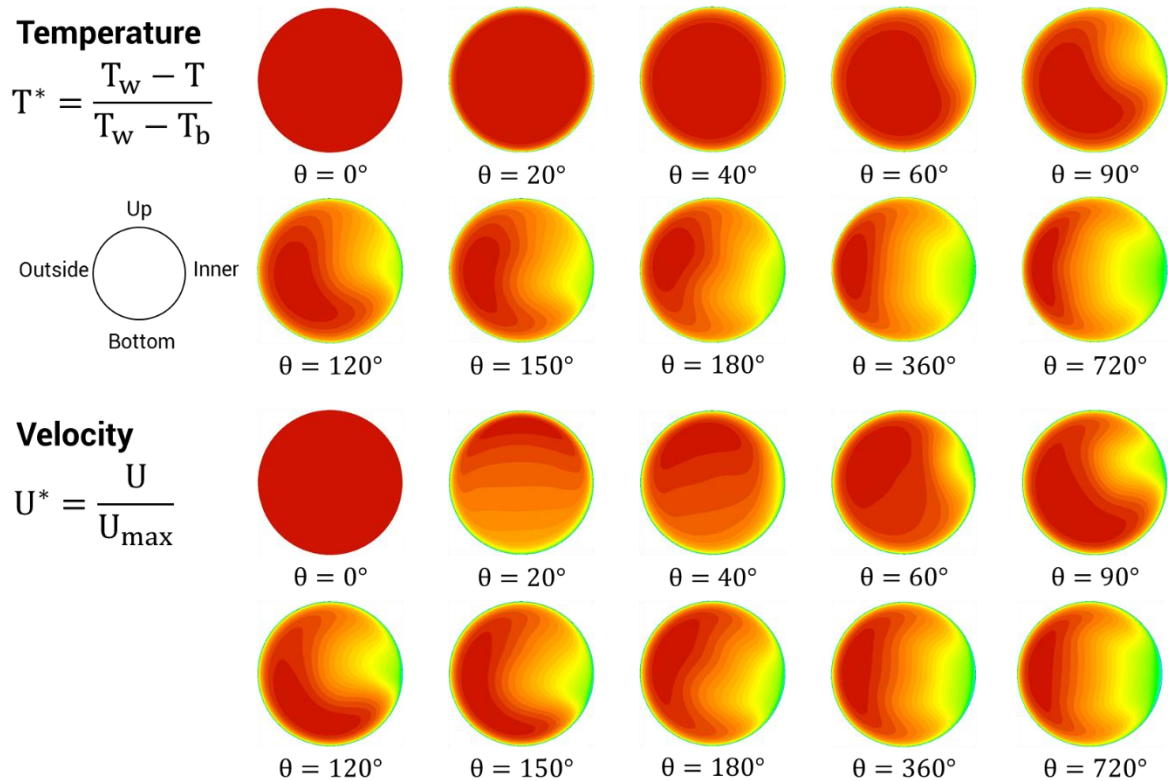


Figure 40. Contours of dimensionless temperature and velocity at different axial positions. $T_w = 370$ K, $T_{in} = 300$ K, $Re = 32.5k$.

Figure 41 shows the contours of kinetic energy. In contrast with dimensionless temperature and velocity, we observe that higher values of turbulence kinetic energy (k) are found near the wall, while lower values of k are moving outside the tube. This region of lower values indicates smaller variation of the velocity in this zone. The medium values of k in the region near to the inner side stand out, indicating a zone more turbulent in the inner side of the coil.

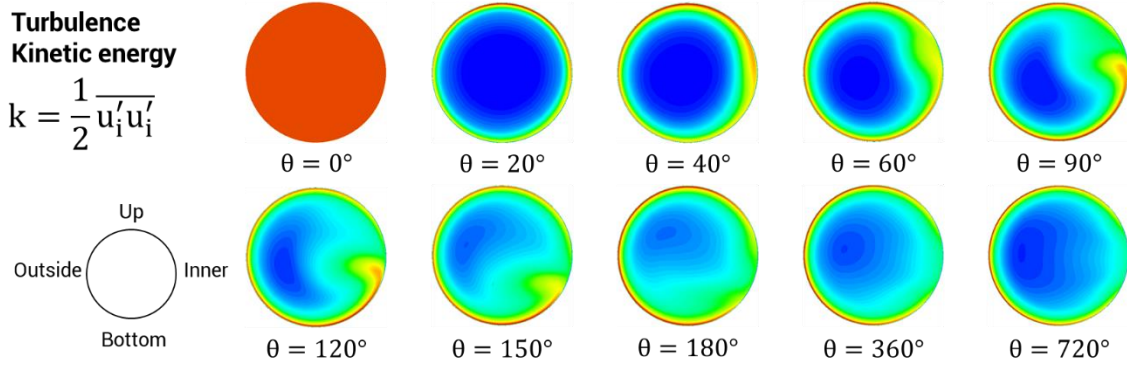


Figure 41. Contours of kinetic energy at different axial positions. $T_w = 370$ K, $T_{in} = 300$ K, $Re = 32.5k$.

4.2.4 Case analysis

The complete set of simulations for this section are showed in Table 18 and the dimensions of the distinct geometries are defined in Table 19.

4.2.4.1 Geometry variation

The results of the average Nusselt number for the simulations with a distinct geometry are showed in Figure 42. From this figure, we observe that Nusselt number increases for a lower curvature ratio. In other words, as the coil diameter increases (D_c), the thermal performance increases. Also, as the dimensionless pitch (λ) increases, the Nusselt number slightly increases.

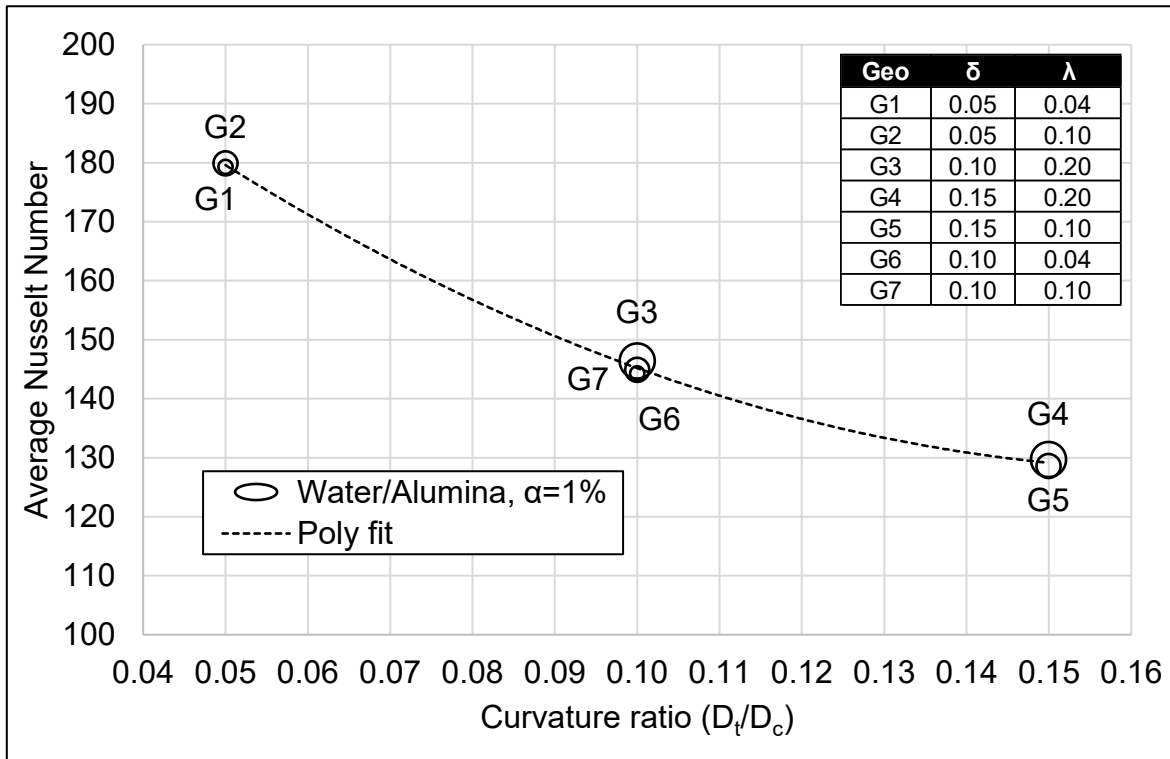


Figure 42. Average Nusselt number for the seven geometries. The nanofluid is the same: $\text{H}_2\text{O}/\text{Al}_2\text{O}_3$, $\alpha = 1\%$.

4.2.4.2 Dean number variation

From Figure 43, we noticed the relationship of the Dean number with the Nusselt number. The figure shows the increases of Nusselt number as the Dean number increases. This relationship is a well-known relation given the increase in turbulence and the mixture of the fluid inside the helical coil.

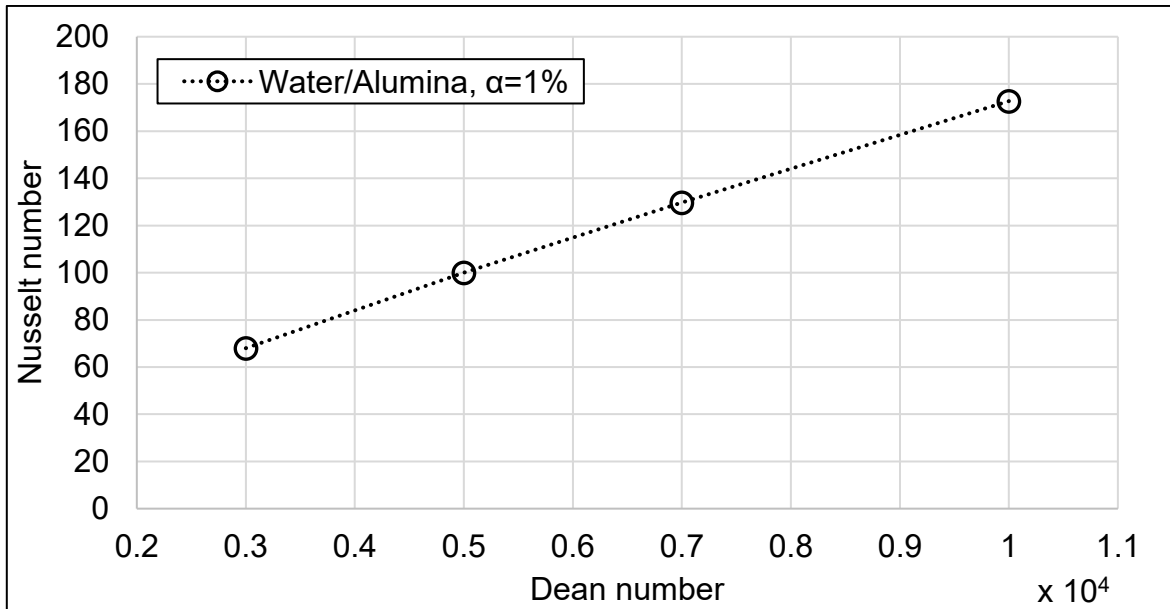


Figure 43. Nusselt number for 9 different Nanofluids.

4.2.4.3 Concentration variation

From Figure 44, we observe that Nusselt number increases as the volume concentration increases. It is worth to highlight the range of the Y-axis in comparison with Figure 42 and Figure 43. In comparison, the increase of volume concentration is lower than the increase of Dean number in the range studied.

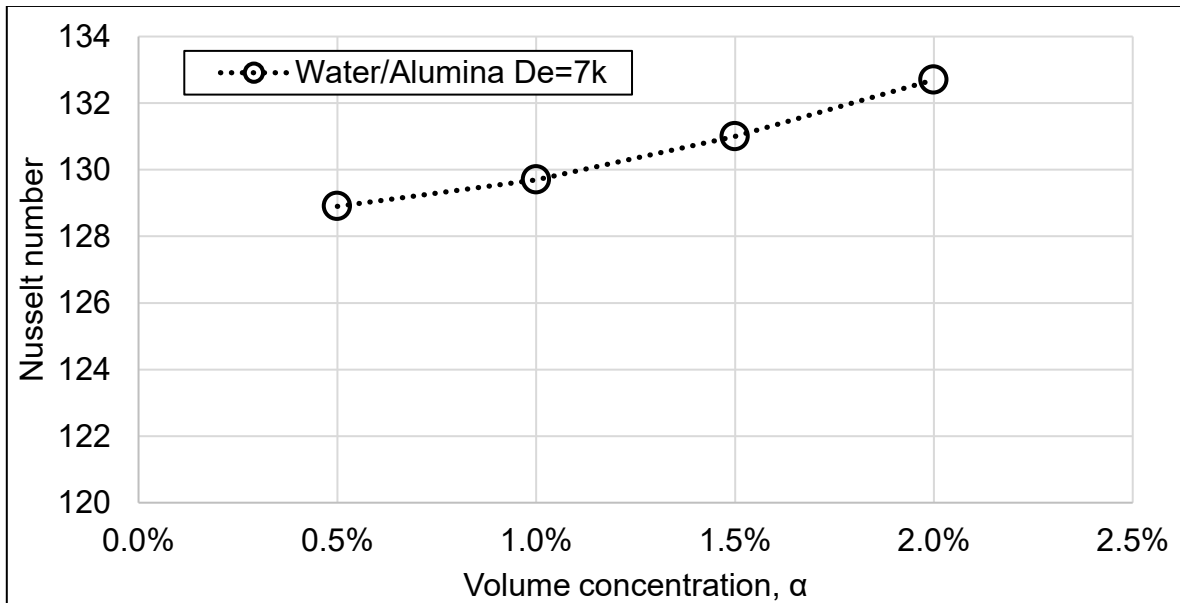


Figure 44. Nusselt number for a variation in Dean number.

4.2.4.4 Nanofluid variation

Figure 45 shows the variation of the Nusselt number for the different nanofluids simulated. From the figure, we observe that the data values of Nusselt number has a good fit to a linear regression of the natural logarithm of the Prandtl number.

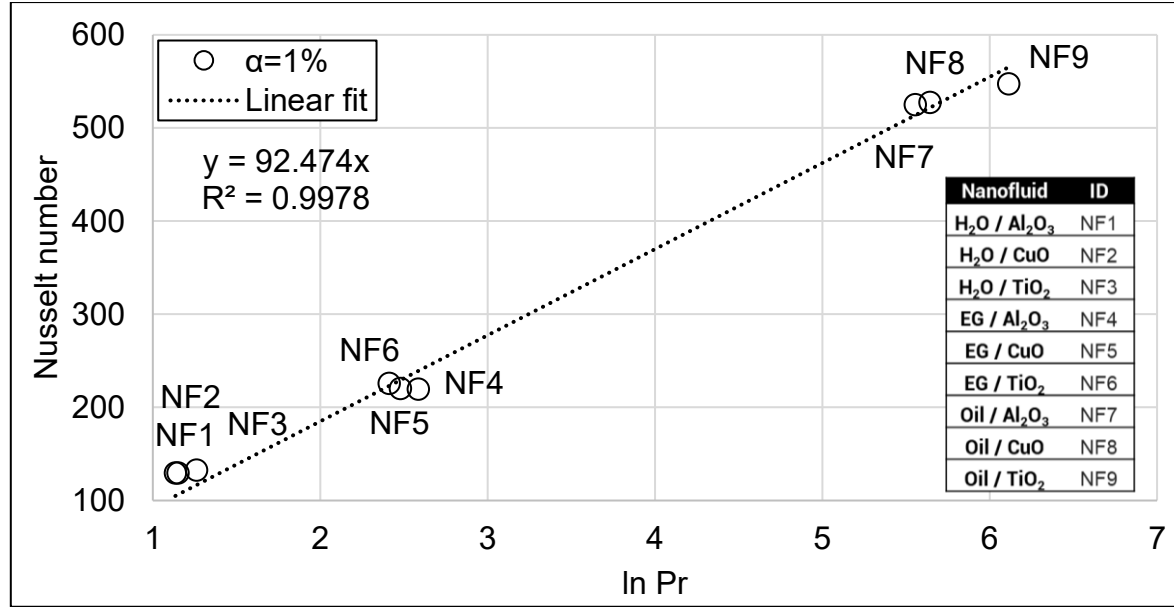


Figure 45. Nusselt number for a variation of nanoparticle concentration.

From the results above we observe that curvature ratio (δ), Dean number (De), volume concentration (α) and Prandtl number (Pr) modify the Nusselt number of the nanofluids flow in helical coils. In the next section we show two correlations obtained from the data simulated.

4.2.5 Correlation by nanofluids

First, we will correlate the data for Water / Alumina. This nanofluids (including different concentration) has more data points than any other nanofluid. This greater amount of data is result of the definition of the experiment.

Figure 46 shows the correlation found to estimate the Nusselt number in the nanofluids of Water / Alumina. The correlation is showed in equation (66).

$$Nu = 0.0283 \cdot Pr^{0.9367} Re^{0.7666} \delta^{0.0908} \alpha^{-0.008} \quad (66)$$

$$3.04 \leq Pr \leq 3.18$$

$$8000 \leq Re \leq 30\,000$$

$$0.05 \leq \delta \leq 0.15$$

$$0.5\% \leq \alpha \leq 2\%$$

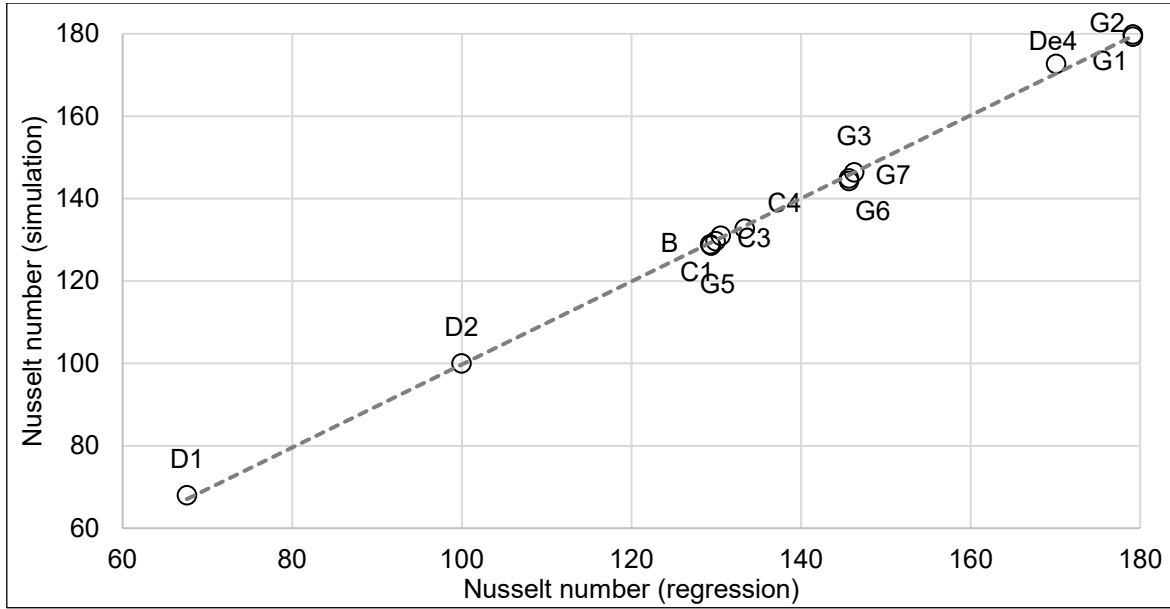


Figure 46. Correlation for Water / Alumina.

It is worth to mention that a previous form of the correlation (66) without including the Prandtl number. This correlation without the Prandtl number is showed in the equation (67) to comparison with the other correlations found.

$$Nu = 0.0857 \cdot Re^{0.7711} \delta^{0.0742} \alpha^{0.0198} \quad (67)$$

$$8000 \leq Re \leq 30\,000$$

$$0.05 \leq \delta \leq 0.15$$

$$0.5\% \leq \alpha \leq 2\%$$

The same form of the equation made for Water / Alumina was implemented for all the nanofluids modeled. The resulting correlation using all the simulations as input is showed in Figure 47. Although it can be seen a good fit of the correlation found with the modeled data. It is not sufficient to accurately estimate the Nusselt number for fluids having a high Prandtl number. The correlation is showed in equation (68).

$$Nu = 0.0828 \cdot Pr^{0.2927} Re^{0.7363} \delta^{0.0743} \alpha^{0.0079} \quad (68)$$

$$3.04 \leq Pr \leq 451.35$$

$$8000 \leq Re \leq 30\,000$$

$$0.05 \leq \delta \leq 0.15$$

$$0.5\% \leq \alpha \leq 2\%$$

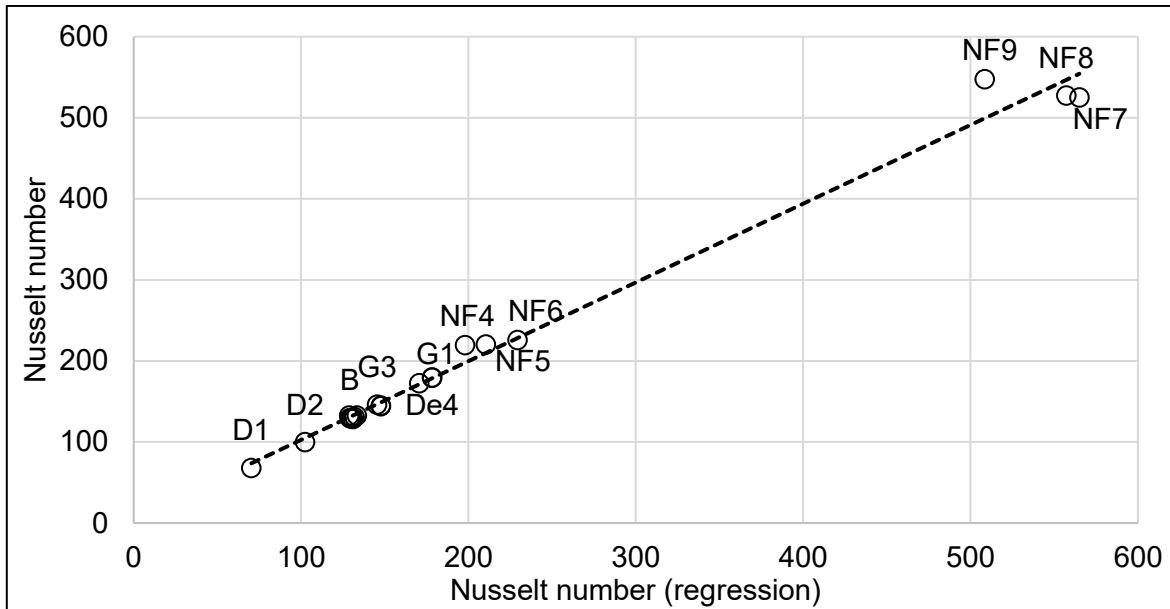


Figure 47. General correlation found for the nanofluids studied.

Given the results from the correlations above, we compare the coefficients and exponents. Where the symbol “A” represents the coefficient of the correlation. Here we observe that for the three equations (66), (67) and (68) shares the same exponent for the Reynolds number. In this sense, equations (67) and (68) also shares the coefficient (A) and the exponent of δ but the exponent of α for equation (67) is 2.5 times the exponent for equation (68). Finally, the coefficient and exponents when Prandtl number is included in equation (66) is different from the other correlations.

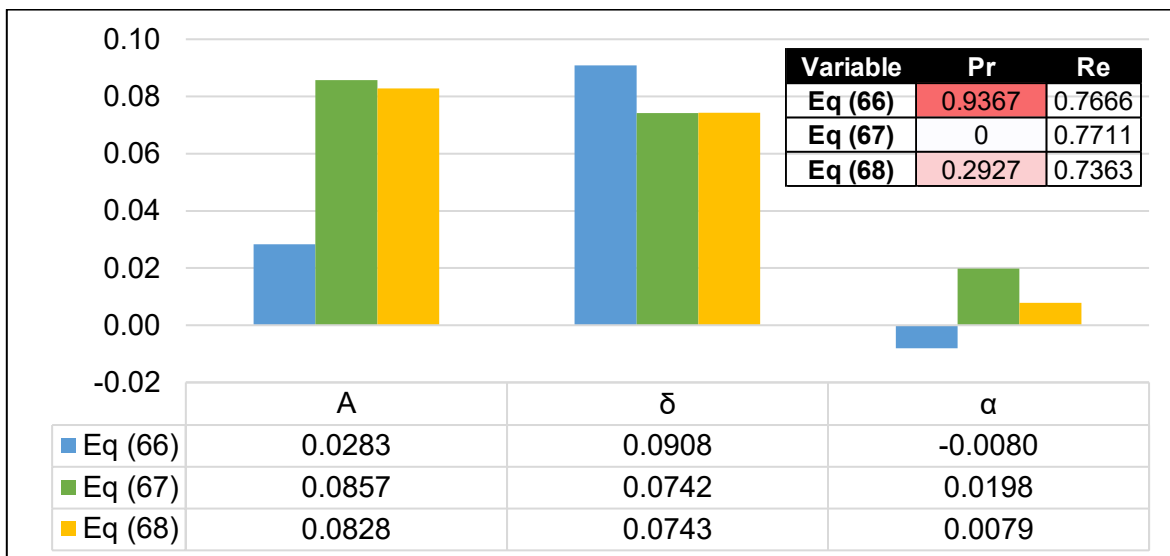


Figure 48. Coefficients and exponents of the correlations (66), (67) and (68).

Chapter 5 Conclusions

5.1 DPEC Model

A 1D model was developed for this study. This 1D model provide us a tool to simulate the performance of a DPEC system. The remarkable features of the model developed is a low computational requirement and thereby a low computational time needed to simulate different scenarios in an hourly basis. For example, the computational time required to solve 1000 data points was of 226.5 seconds. The personal computer used have 8 GB RAM memory and Core i5 8th generation processor.

Through the parametric analysis it was noticed a remarkable behavior provoked by the relative humidity (i.e. the amount of water mass in relation with air mass). The results show that at a higher relative humidity the effectiveness of the device increases. This could suggest that the water mass added into the air has a weak dependency on the relative humidity.

It was found a maximum wet-bulb temperature at which the device could provide a conditioning cooling capacity in a space. It means that for hot climates, the device should increase its channel length to be able of working as a stand-alone system.

A correlation to estimate the outlet temperature in the DPEC system was found within a 1% of error for a device of 0.5 channel length in a place with sea level atmospheric pressure.

We carry out an analysis of the model performance for different climates. The model shows that the best performance for the DEPC model is in the climate very arid.

On the other hand, although the environmental cooling capacity was high in the warm climate, the conditioning cooling capacity was not as high as the arid climates due to the high relative humidity.

Also, for the mild climate, though it has not a high requirement of cooling capacity at the reference temperature of 25°C, it could provide conditioning cooling capacity for another application with a reference temperature below 25°C (servers).

5.2 Nanofluids in helical coils

A model was designed to perform numerical simulations of nanofluids in helical coils.

The low error results ($< 5\%$) in the validation process suggests that thermophysical properties correlations, mesh and mathematical model showed a well synergy to accurately simulate the problem.

From the case analysis, it was obtained the influence of the inlet variables (Geometry, Dean number, concentration, nanofluid).

For the variation of geometry, despite the well-known direct relationship with the curvature ratio, it was observed a slight increase when the dimensionless pitch was higher.

For higher velocities or Dean numbers, the nanofluids show an increase in the thermal performance.

For a higher concentration of the nanofluid the thermal performance increases. However, the increase in the thermal performance were not as high as the Dean number or geometry.

A correlation of Nusselt number for water/alumina was obtained. The correlation shows good agreement by the variation of curvature ratio, Reynolds number, Prandtl and volume concentration of the alumina.

A correlation of Nusselt number for the nanofluids simulated was also found. This correlation is a useful equation to estimate the thermal performance of helical coils for a variety of nanofluids.

5.3 Future work

5.3.1 DPEC systems

A deeper analysis of the DPEC model should be made to improve the accuracy of the model. The model should be work as a practical tool to increase the presence of these systems where the reliability of DPEC systems is not clear. In this regard, the main characteristic of a future model should maintain the low computational requirements needed to extend its use in an hourly basis for a typical year.

Another approach of a practical tool should be further investigation on pi-numbers and how they are correlated with the outlet temperature. A regression to estimate the outlet temperatures is a significant advance in this topic. It should be studied the use of the maximum wet-bulb temperature as a first and practical parameter design to define the viability of the system for a specific climate. Experimental work to prove this tool is desirable.

Finally, Hourly analysis should be made in more climates and sub-climates to assess the performance of the model in more scenarios.

5.3.2 Nanofluids in helical coils

More inlet temperatures and geometries for the different nanofluids should be simulated for the different nanofluids and find general correlation for the nanofluids.

Perform simulations with other mathematical model such as the dispersion model for the nanofluids studied.

Compare the state of the art of the correlation found with other correlations from previous studies.

Develop experimental work with high-Prandtl base fluid (such as oil) to compare the correlation found.

Appendix A – Humid air thermophysical properties

Thermophysical properties of air as functions of temperature, humidity ratio and atmospheric pressure are based from a study of these properties in humid air (Massman, 1998; Picard et al., 2008; Tsilingiris, 2008).

Values and variables considered for the calculation of thermophysical properties are described next.

Molar mass of dry air (kg/kmol)	M_a	28.96546
Molar mass of vapor (kg/kmol)	M_v	18.01528
Universal gas constant (J/molK)	R	8.314472

Also, two additional variables are calculated:

$$x_v = \frac{M_a \omega_w}{M_v + M_a \omega_w}$$

where x_v is the molar fraction of vapor in air. It is the ratio of water vapor moles to the total number of moles of the mixture.

$$Z = 1 - \frac{P_0}{T} [a_0 + a_1 t + a_2 t^2 + (b_0 + b_1 t)x_v + (c_0 + c_1 t)x_v^2] + \frac{P_0^2}{T^2} (d_0 + e_0 \cdot x_v^2)$$

where Z is the compressibility factor of air (Picard et al., 2008), P_0 is the atmospheric pressure in kilopascals (kPa), T is the temperature in Kelvins (K) and, t is the temperature in Celsius degrees ($^{\circ}\text{C}$). The constant values involved to calculate Z are:

$$\begin{aligned} a_0 &= 1.58123 \times 10^{-3} \text{ [K kPa}^{-1}\text{]} & a_1 &= -2.9331 \times 10^{-5} \text{ [kPa}^{-1}\text{]} \\ a_2 &= 1.1043 \times 10^{-7} \text{ [K}^{-1} \text{ kPa}^{-1}\text{]} & b_1 &= -2.051 \times 10^{-5} \text{ [kPa}^{-1}\text{]} \\ b_0 &= 5.707 \times 10^{-3} \text{ [K kPa}^{-1}\text{]} & c_1 &= 2.376 \times 10^{-3} \text{ [kPa}^{-1}\text{]} \\ c_0 &= 0.19898 \text{ [K kPa}^{-1}\text{]} & e_0 &= -0.765 \times 10^{-2} \text{ [K}^2 \text{ kPa}^{-2}\text{]} \\ d_0 &= 1.83 \times 10^{-5} \text{ [K}^2 \text{ kPa}^{-2}\text{]} \end{aligned}$$

In the following lines, we exhibit the equations for thermophysical properties of humid air. The properties calculated are density (ρ), specific heat (c_p) and thermal conductivity (θ). The subscripts m, a and v represent the mixture, (dry) air and vapor, respectively.

Density (kg/m³)

$$\rho_m = \frac{M_a P_0}{ZRT} \left[1 - x_v \left(1 - \frac{M_v}{M_a} \right) \right]$$

Where ρ_m is the density of the mixture air-vapor.

Specific Heat (kJ / (kg K))

$$c_{p,m} = c_{p,a}(1 - x_v) \frac{M_a}{M_m} + c_{p,v}x_v \frac{M_v}{M_m}$$

Where $c_{p,m}$ is the specific heat of the mixture air-vapor, $c_{p,a}$ is the specific heat of dry air, and $c_{p,v}$ is the specific heat of vapor. The coefficients to calculate $c_{p,a}$ and $c_{p,v}$ are present next.

$$M_m = M_a(1 - x_v) + M_vx_v$$

$$c_{p,a}(T) = CA_4T^4 + CA_3T^3 + CA_2T^2 + CA_1T + CA_0$$

$$c_{p,v}(t) = CV_2t^2 + CV_1t + CV_0$$

where T is the air temperature in Kelvins and t is the air temperature in °C. The constant values of the above equations are presented next.

$CA_4 = 0.1077024 \times 10^{-12} \text{ [kJ kg K}^{-5}\text{]}$	$CV_2 = 1.941058941 \times 10^{-5}$
$CA_3 = -0.4970786 \times 10^{-9} \text{ [kJ kg K}^{-4}\text{]}$	$CV_1 = -2.578421578 \times 10^{-4} \text{ [kJ kg K}^{-2}\text{]}$
$CA_2 = 0.7816818 \times 10^{-6} \text{ [kJ kg K}^{-3}\text{]}$	$CV_0 = 1.86910989 \text{ [kJ kg K}^{-1}\text{]}$
$CA_1 = -0.284887 \times 10^{-3} \text{ [kJ kg K}^{-2}\text{]}$	
$CA_0 = 1.03409 \text{ [kJ kg K}^{-1}\text{]}$	

Thermal conductivity (W / (m K))

$$\theta_m = \frac{\theta_a + x_v(0.8536 \cdot \theta_v - \theta_a)}{1 - 0.1464x_v}$$

where θ_m is the thermal conductivity of the mixture air-vapor, θ_a is the thermal conductivity of dry air, and θ_v is the thermal conductivity of vapor.

$$\theta(T) = KA_5T^5 + KA_4T^4 + KA_3T^3 + KA_2T^2 + KA_1T + KA_0$$

$$\theta(t) = KV_2t^2 + KV_1t + KV_0$$

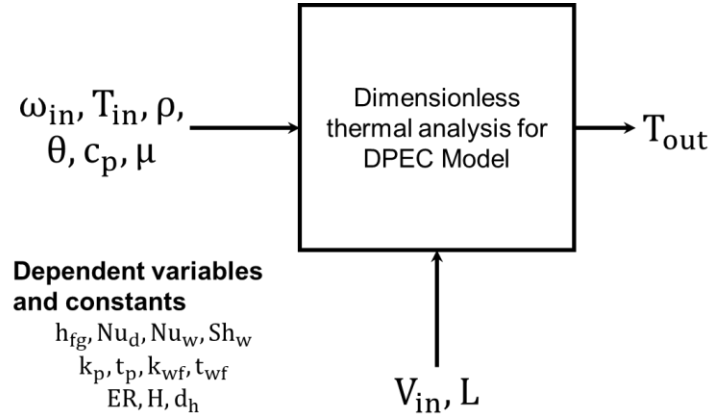
where T is the air temperature in Kelvins and t is the air temperature in °C. The constant values of the above equations are presented in the following lines.

$KA_5 = 2.47663035 \times 10^{-17} \text{ [W m}^{-1} \text{ K}^{-6}\text{]}$	$KV_2 = 1.663336663 \times 10^{-7} \text{ [W m}^{-1} \text{ K}^{-3}\text{]}$
$KA_4 = -1.066657 \times 10^{-13} \text{ [W m}^{-1} \text{ K}^{-5}\text{]}$	$KV_1 = 5.558941059 \times 10^{-5} \text{ [W m}^{-1} \text{ K}^{-2}\text{]}$
$KA_3 = 1.73550646 \times 10^{-10} \text{ [W m}^{-1} \text{ K}^{-4}\text{]}$	$KV_0 = 0.061758242 \text{ [W m}^{-1} \text{ K}^{-1}\text{]}$
$KA_2 = -1.4815235 \times 10^{-7} \text{ [W m}^{-1} \text{ K}^{-3}\text{]}$	
$KA_1 = 1.2598485 \times 10^{-4} \text{ [W m}^{-1} \text{ K}^{-2}\text{]}$	
$KA_0 = -2.276501 \times 10^{-3} \text{ [W m}^{-1} \text{ K}^{-1}\text{]}$	

Appendix B – Dimensionless analysis

The dimensionless analysis for both modes were made by following the Buckingham Pi-Theorem.

DPEC model



From the above diagram, we have four dimensions: Distance (D), Mass (M), Time (T), and temperature (K). For each dimension, we select one variable which contain that dimension. Therefore, for Distance we select the Length variable (L), for Mass we select the density variable (ρ), for Time we select the inlet velocity variable (V_{in}) and for temperature we select the thermal conductivity variable (θ). From the variables of the problem, the humidity ratio (ω_{in}) is in terms of water mass divided by the air mass, hence is already a dimensionless number. Then, according to the Buckingham Pi Theorem, we will find the dimensionless groups on the remain unselected variables. All the variables included in the dimensionless analysis are described next.

Selected variables	Unselected variables
$n_1 = D \rightarrow L: [m] = [D]$	$\pi_0 \rightarrow \omega_{in}: [-] \equiv [-]$
$n_2 = M \rightarrow \rho: \left[\frac{kg}{m^3}\right] = [MD^{-3}]$	$\pi_1 \rightarrow T_{in}, T_{out}: [K] \equiv [K]$
$n_3 = T \rightarrow V_{in}: \left[\frac{m}{s}\right] = [DT^{-1}]$	$\pi_2 \rightarrow c_p: \left[\frac{m^2}{s^2 K}\right] \equiv [D^2 T^{-2} K^{-1}]$
$n_4 = K \rightarrow \theta: \left[\frac{W}{m K}\right] = [MDT^{-3} K^{-1}]$	$\pi_3 \rightarrow \mu: \left[\frac{kg}{m \cdot s}\right] \equiv [MD^{-1} T^{-1}]$

Pi-number 1

$$\omega_{in} \text{ or RH: } [\pi_0]$$

Pi-number 1

It is common to define the non-dimension temperature in terms of other temperature of reference (T). In this case, we will use two common relations in DPEC systems: wet-bulb effectiveness (ε_{wb}) and dew-point effectiveness (ε_{DP}).

$$\pi_{1,1} = \varepsilon_{wb} = \frac{T_{in} - T_{out}}{T_{in} - T_{wb,in}}, \quad \pi_{1,2} = \frac{T_{in} - T_{out}}{T_{in} - T_{DP,in}}$$

Pi-number 2

$$c_p: [\pi_2] = c_p(D_t)^{n_1}(\rho)^{n_2}(V_{in})^{n_3}(\theta)^{n_4}$$

$$[\pi_2] = [D^2 T^{-2} K^{-1}][D]^{n_1}[MD^{-3}]^{n_2}[DT^{-1}]^{n_3}[MDT^{-3}K^{-1}]^{n_4}$$

$$[\pi_1] = D(2 + n_1 - 3n_2 + n_3 + n_4) + T(-2 - n_3 - 3n_4) + K(-1 - n_4) + M(n_2 + n_4)$$

$$n_1 = 1, \quad n_2 = 1, \quad n_3 = 1, \quad n_4 = -1$$

$$\pi_2 = \frac{c_p D_t \rho V_{in}}{\theta} = RePr = Pr \cdot \pi_3^{-1}$$

Pi-number 3

$$\mu: [\pi_3] = \mu(L)^{n_1}(\rho)^{n_2}(V_{in})^{n_3}(\theta)^{n_4}$$

$$[\pi_3] = [MD^{-1}T^{-1}][D]^{n_1}[MD^{-3}]^{n_2}[DT^{-1}]^{n_3}[MDT^{-3}K^{-1}]^{n_4}$$

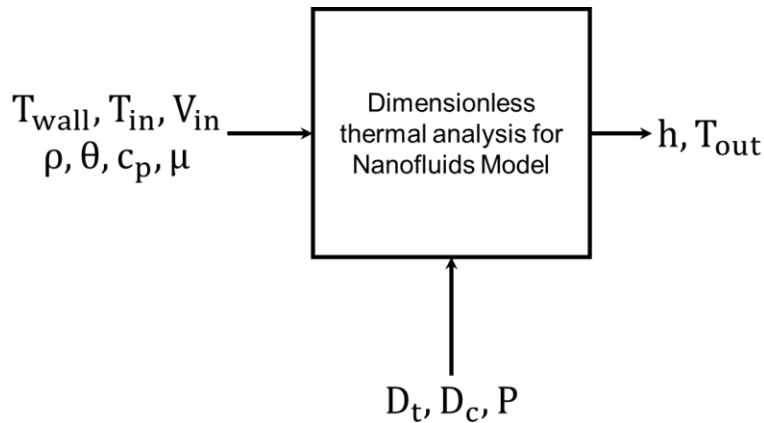
$$[\pi_3] = M(1 + n_2 + n_4) + D(-1 + n_1 - 3n_2 + n_3 + n_4) + T(-1 - n_3 - 3n_4) + K(-n_4)$$

$$n_1 = -1, \quad n_2 = -1, \quad n_3 = -1, \quad n_4 = 0$$

$$\pi_3 = \frac{\mu}{L\rho V_{in}} = Re^{-1}$$

Nanofluids model

Like the dimensionless analysis above, we develop a dimensionless thermal analysis for the Nanofluids model.



As the previous dimensionless analysis, we have four dimensions: Distance (D), Mass (M), Time (T), and temperature (K). The selected variables for each dimensions were: Distance we select the tube diameter (D_t), for Mass we select the density inlet variable (ρ_{in}), for Time we select the inlet velocity variable (V_{in}) and for temperature we select the thermal conductivity variable (θ). Then, we will find the

dimensionless groups on the remain unselected variables. All the variables included in the dimensionless analysis are described next.

Selected variables	Unselected variables
$n_1 \rightarrow D_t \rightarrow L: [m] = [D]$	$\pi_1 \rightarrow T: [K]$
$n_2 \rightarrow M \rightarrow \rho: \left[\frac{kg}{m^3}\right] = [MD^{-3}]$	$\pi_2 \rightarrow c_p: \left[\frac{m^2}{s^2 K}\right] \equiv [D^2 T^{-2} K^{-1}]$
$n_3 \rightarrow T \rightarrow V_{in}: \left[\frac{m}{s}\right] = [DT^{-1}]$	$\pi_3 \rightarrow D_c, P: [m] \equiv [D]$
$n_4 \rightarrow K \rightarrow \theta: \left[\frac{kg \cdot m}{s^3 K}\right] = [MDT^{-3} K^{-1}]$	$\pi_4 \rightarrow h: \left[\frac{kg}{s^3 K}\right] \equiv [ML^{-3} K^{-1}]$

Pi-number 1

$$\begin{aligned}
 T_{in}, T_{wall}, T_{out}: [\pi_1] &= T(D_t)^{n_1}(\rho)^{n_2}(V_{in})^{n_3}(\theta)^{n_4} \\
 [\pi_1] &= [K][D]^{n_1}[MD^{-3}]^{n_2}[DT^{-1}]^{n_3}[MDT^{-3}K^{-1}]^{n_4} \\
 [\pi_1] &= K(1 - n_4) + D(n_1 - 3n_2 + n_3 + n_4) + M(n_2 + n_4) + T(-3n_3 - n_4) \\
 n_1 &= -1, \quad n_2 = -1, \quad n_3 = -3, \quad n_4 = 1 \\
 \pi_1 &= \frac{T\theta}{D_t \rho V_{in}^3}
 \end{aligned}$$

Pi-number 2

$$\begin{aligned}
 c_p: [\pi_2] &= c_p(D_t)^{n_1}(\rho)^{n_2}(V_{in})^{n_3}(\theta)^{n_4} \\
 [\pi_2] &= [D^2 T^{-2} K^{-1}][D]^{n_1}[MD^{-3}]^{n_2}[DT^{-1}]^{n_3}[MDT^{-3}K^{-1}]^{n_4} \\
 [\pi_2] &= D(2 + n_1 - 3n_2 + n_3 + n_4) + T(-2 - n_3 - 3n_4) + K(-1 - n_4) + M(n_2 + n_4) \\
 n_1 &= 1, \quad n_2 = 1, \quad n_3 = 1, \quad n_4 = -1 \\
 \pi_2 &= \frac{c_p \rho D_t V_{in}}{\theta} = \frac{\mu c_p}{\theta} \frac{\rho D_t V_{in}}{\mu} = Pr \cdot Re
 \end{aligned}$$

Pi-number 3

$$\begin{aligned}
 D_c, P: [\pi_3] &= D_c(D_t)^{n_1}(\rho)^{n_2}(V_{in})^{n_3}(\theta)^{n_4} \\
 [\pi_3] &= [D][D]^{n_1}[MD^{-3}]^{n_2}[DT^{-1}]^{n_3}[MDT^{-3}K^{-1}]^{n_4} \\
 [\pi_3] &= D(1 + n_1 - 3n_2 + n_3 + n_4) + T(-n_3 - 3n_4) + K(-n_4) + M(n_2 + n_4) \\
 n_1 &= -1, \quad n_2 = 0, \quad n_3 = 0, \quad n_4 = 0 \\
 \pi_{3,D_c} &= \frac{D_c}{D_t} = \delta^{-1}, \quad \pi_{3,P} = \frac{P}{D_t}
 \end{aligned}$$

Pi-number 4

$$h: [\pi_4] = h(D_t)^{n_1}(\rho)^{n_2}(V_{in})^{n_3}(\theta)^{n_4}$$

$$[\pi_4] = MT^{-3}K^{-1}[D]^{n_1}[MD^{-3}]^{n_2}[DT^{-1}]^{n_3}[MDT^{-3}K^{-1}]^{n_4}$$

$$[\pi_4] = M(1 + n_2 + n_4) + T(-3 - n_3 - 3n_4) + K(-1 - n_4) + D(n_1 - 3n_2 + n_3 + n_4)$$

$$n_1=1,\qquad n_2=0,\qquad n_3=0,\qquad n_4=-1$$

$$\pi_4=\frac{hD_t}{\theta}=\text{Nu}$$

$$\pi_4=f(\pi_1,\pi_2,\pi_3,\pi_4)$$

$$\pi_4=\left(\frac{T\theta}{D_t\rho V_{\rm in}^3},\Pr\cdot\text{Re},\delta,\frac{P}{D_t}\right)$$

Appendix C – Coefficients for nanofluid thermophysical properties

Nanofluid	Conc	Prop	R2	A0	A1	A2
H2O/Al2O3	0.5%	ρ	1.0000	8.1776E+02	1.5837E+00	-3.0845E-03
		c_p	1.0000	4.8728E+03	-4.5192E+00	6.8675E-03
		θ	1.0000	-1.0313E+00	8.9460E-03	-1.1254E-05
		μ	1.0000	1.5955E-02	-8.4787E-05	1.1512E-07
	1.0%	ρ	1.0000	8.3360E+02	1.5758E+00	-3.0690E-03
		c_p	1.0000	4.7801E+03	-4.3272E+00	6.5323E-03
		θ	1.0000	-1.1968E+00	9.8695E-03	-1.2362E-05
		μ	1.0000	1.6747E-02	-8.8995E-05	1.2083E-07
	1.5%	ρ	1.0000	8.4944E+02	1.5678E+00	-3.0535E-03
		c_p	1.0000	4.6905E+03	-4.1448E+00	6.2147E-03
		θ	1.0000	-1.3217E+00	1.0566E-02	-1.3197E-05
		μ	1.0000	1.7635E-02	-9.3719E-05	1.2724E-07
	2.0%	ρ	1.0000	8.6528E+02	1.5599E+00	-3.0380E-03
		c_p	1.0000	4.6040E+03	-3.9714E+00	5.9134E-03
		θ	1.0000	-1.4257E+00	1.1146E-02	-1.3894E-05
		μ	1.0000	1.8635E-02	-9.9030E-05	1.3445E-07
H2O/CuO	1.0%	ρ	1.0000	8.5890E+02	1.5758E+00	-3.0690E-03
		c_p	1.0000	4.6512E+03	-4.0776E+00	6.0934E-03
		θ	1.0000	-1.1388E+00	9.5460E-03	-1.1974E-05
		μ	1.0000	1.7036E-02	-9.0532E-05	1.2292E-07
H2O_TiO2	1.0%	ρ	1.0000	8.3547E+02	1.5758E+00	-3.0690E-03
		c_p	1.0000	4.7689E+03	-4.3062E+00	6.4951E-03
		θ	1.0000	-1.1259E+00	9.4736E-03	-1.1887E-05
		μ	1.0000	1.7679E-02	-9.3951E-05	1.2756E-07
EG_Al2O3	1.0%	ρ	1.0000	1.0218E+03	9.8026E-01	-2.4073E-03
		c_p	1.0000	2.0839E+03	3.8601E+00	-2.9583E-04
		θ	1.0000	-5.8227E-01	5.3149E-03	-6.6268E-06
		μ	0.9993	1.6305E-01	-9.5725E-04	1.4196E-06
EG_CuO	1.0%	ρ	1.0000	1.0471E+03	9.8026E-01	-2.4073E-03
		c_p	1.0000	2.0309E+03	3.8678E+00	-4.9382E-04
		θ	1.0000	-5.4030E-01	5.0788E-03	-6.3388E-06
		μ	1.0000	1.6672E-01	-9.7877E-04	1.4516E-06

EG_TiO2	1.0%	ρ	1.0000	1.0237E+03	9.8026E-01	-2.4073E-03
		c_p	1.0000	2.0787E+03	3.8619E+00	-3.1373E-04

		θ	1.0000	-5.3090E-01	5.0259E-03	-6.2744E-06
		μ	0.9993	1.7501E-01	-1.0274E-03	1.5238E-06
Oil_Al2O3	1.0%	ρ	1.0000	1.0827E+03	-6.4350E-01	1.8976E-17
		c_p	1.0000	6.2895E+02	4.3961E+00	-1.7944E-04
		θ	0.9998	-5.8673E-02	1.1694E-03	-1.6052E-06
		μ	0.9989	8.7987E+00	-5.3236E-02	8.0743E-05
Oil_CuO	1.0%	ρ	1.0000	1.1080E+03	-6.4350E-01	1.8976E-17
		c_p	1.000	6.1663E+02	4.3064E+00	-2.8466E-04
		θ	0.9998	-3.7954E-02	1.0492E-03	-1.4497E-06
		μ	0.9988	9.2991E+00	-5.6264E-02	8.5335E-05
Oil_TiO2	1.0%	ρ	1.0000	1.0846E+03	-6.4350E-01	1.8976E-17
		c_p	1.000	6.2691E+02	4.3889E+00	-1.8841E-04
		θ	0.9998	-3.3317E-02	1.0223E-03	-1.4149E-06
		μ	0.9989	1.0566E+01	-6.3928E-02	9.6959E-05

Appendix D – DPEC model codes

In this section, the code implemented in MATLAB for solving the Ordinary Differential Equations (ODE) system of the Dew-Point Evaporative Cooling (DPEC) system is shown. A general scheme of the code is shown in Figure 49.

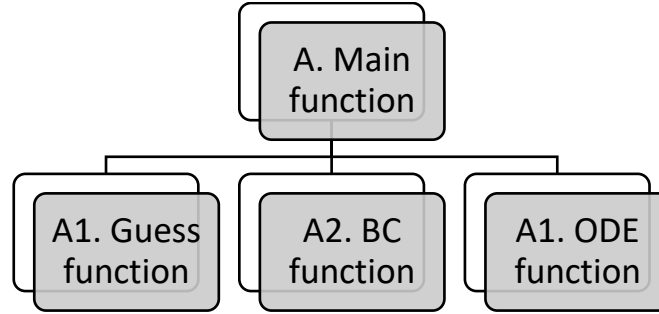


Figure 49. Structure of the code developed for the DPEC model.

The main program (A. Main) receive the input variables and define the problem. Then, 3 functions were developed: A1 regarding the guess function, A2 regarding the Boundary Condition function and A3 regarding the Ordinary Differential Equations or the initial values. The input vector x_0 is organized in the following form:

$$x_0 = \begin{bmatrix} \text{Dry mass flow } \left(\frac{\text{kg}}{\text{s}}\right) \\ \text{Wet mass flow } \left(\frac{\text{kg}}{\text{s}}\right) \\ \text{Inlet Temperature } (^{\circ}\text{C}) \\ \text{Inlet humidity ratio } \left(\frac{\text{kg}_{\text{water}}}{\text{kg}_{\text{air}}}\right) \\ \text{Atmospheric pressure (kPa)} \\ \text{Channel length (m)} \end{bmatrix}$$

Because mass flows are variable for each run and are not a differentiable variable of the ODE system, they must be passed to the solver from a nested function which is coded as `@(Xs, Ts)odefun(Xs,Ts,x0(1:2))` where the mass flows are in the vector $x_0(1:2)$ and Xs and Ts vectors are the inputs coded in *odefun* which will be solved in *bvp5c*. Similarly, the boundary conditions at the end of the domain depend on the outlet temperature reached, so they passed as variables in a nested function. And finally, the initial conditions are set-up from constant values, so they followed the same process from above.

A. Main program

```
function [y,Temp] = EC_ODEs_func3(x0)
% This function recieve as an input the values of
% x0(1): Mass flow in the dry channel
% x0(2): Mass flow in the wet channel
% x0(3): Inlet Dry Temperature
% x0(4): Inlet specific humidity

% Add path for extra equations
addpath([pwd,'\Extra']);

% ODE system variables are:
np = 51;
x = linspace(0,x0(6),np)'; % L = x0(6)
solinit = bvpinit(x,@(x)guess(x,x0(3:4)));
opts = bvpset('RelTol',1e-5,...
              'AbsTol',1e-6,...
              'Stats','on',...
              'NMax',np);

%% Solve ODE system
xin = [x0(1:2),x0(5),x0(4)];

T = bvp5c(@(Xs,Ts)odefun2(Xs,Ts,xin),...
          @(T0,TL)bcfun(T0,TL,x0(3:4)),solinit,opts);

%% Get results
% WB Effectiveness y Outlet temperature
% Tout, Toutw, wout
y = T.y(1,1);
Temp = T.y;
clear('T','np','x','solinit','opts','xin');
end
```

A1. Guess function

```
function Tinit = guess(x,x0)
%% Function to define inital guess values
% T(1) for Td
% T(2) for Tw
% T(3) for ww
% T(4) for Twf
% T(5) for dTwf

%% Initial values
```

```
% Values experimentally
omega_in = x0(2);
Td = x0(1);
```

```
%% Definition of values
Tinit(1) = Td;
Tinit(2) = Td;
Tinit(3) = omega_in;
Tinit(4) = Td;
Tinit(5) = 0*x;
```

```
end
```

BC function

```
function res = bcfun(T0,TL,x0)
%% Boundary condition functions
% T(1) for Td
% T(2) for Tw
% T(3) for ww
% T(4) for Twf
% T(5) for dTwf
res = [ T0(1)-T0(2)
        T0(3)-x0(2)
        T0(5)
        TL(1)-x0(1)
        TL(5)];
end
```

ODE function

```
function des = odefun2(x,T,v)
% This function calculate the ordinary
% differential equations system (ODE)
% that describes the heat exchange in a
% regenerative evaporative cooling system.
%addpath([pwd,'\Extra']);

%% Geometry & Materials
H = 0.3; %
%% Heat transfer parameters
k_p = 0.21; % W/mK Not significative
k_wf = 0.5449; % W/mK
Nu_d = 2.811; %[1]
Nu_w = 4; %[1]
```

```

%% Air properties
[~,k_d,cp_d,~] = propMoistAir(T(1),v(4),v(3));
[rho_w,k_w,cp_w,~] = propMoistAir(T(2),T(3),v(3));
D_va = (0.2178*(T(2)/273.15+1)^1.81)*1e-4; % Massman
cp_d = cp_d*1000;
cp_w = cp_w*1000;
% Le = 1;

%% Coefficients of heat and mass transfer
h_d = Nu_d*k_d/(2.4e-3);
h_w = Nu_w*k_w/(2.4e-3);
h_m = Nu_w*D_va/(2.4e-3);

%% Global coefficient of Heat Transfer
U = 1/(1/h_d + 0.0002/k_p + 0.00015/k_wf);

%% Auxiliary functions
psat = @(T) exp(1.2378847e-5*(T+273.15).^2 ...
    -1.9121316e-2*(T+273.15) ...
    + 33.93711047 ...
    -6.3431645e3./(T+273.15))*1e-3;
%Pg = @(Tw1) (0.61121*exp((18.678-Tw1/234.5)*(Tw1/(257.14+Tw1))));
f1 = @(Tw2) (0.622*psat(Tw2)/(v(3)-psat(Tw2)));
f2 = @(Twf1) (1000*(2501-2.369*Twf1));

%% Functions
% T for temperature
% T(1) for Td
% T(2) for Tw
% T(3) for ww
% T(4) for Twf
% T(5) for dTwf
des = zeros(5,1);
des(1) = -U*H/(v(1)*cp_d)*(T(4)-T(1));
des(2) = h_w*H/(v(2)*cp_w)*(T(4)-T(2));
des(3) = h_m*rho_w*H/v(2)*(f1(T(2))-T(3));
des(4) = T(5);
des(5) = (h_w*(T(2)-T(4))+U*(T(1)-T(4))+...
    f2(T(4))*h_m*rho_w*(T(3)-f1(T(2))))/...
    (-k_wf*0.0002);

end

```

Bibliography

- Akbaridoust, F., Rakhsha, M., Abbassi, A., & Saffar-Avval, M. (2013). Experimental and numerical investigation of nanofluid heat transfer in helically coiled tubes at constant wall temperature using dispersion model. *International Journal of Heat and Mass Transfer*, 58(1–2), 480–491. <https://doi.org/10.1016/j.ijheatmasstransfer.2012.11.064>
- Akhavan-Behabadi, M. A., Fakoor Pakdaman, M., & Ghazvini, M. (2012). Experimental investigation on the convective heat transfer of nano fluid flow inside vertical helically coiled tubes under uniform wall temperature condition. *International Communications in Heat and Mass Transfer*, 39, 556–564. <https://doi.org/10.1016/j.icheatmasstransfer.2012.02.008>
- Aly, W. I. A. (2014). Numerical study on turbulent heat transfer and pressure drop of nanofluid in coiled tube-in-tube heat exchangers. *Energy Conversion and Management*, 79, 304–316. <https://doi.org/10.1016/j.enconman.2013.12.031>
- Anderson, D. A., Tannehill, J. C., & Pletcher, R. H. (1997). *Computational Fluid Mechanics and Heat Transfer* (2nd ed.). Washington, DC: Taylor & Francis.
- Andersson, B., Andersson, R., Hakansson, L., Mortensen, M., Sudiyo, R., & Van-Wachem, B. (2012). *Computational Fluid Dynamics for Engineers*. Cambridge: Cambridge University Press. Retrieved from www.cambridge.org/9781107018952
- Anisimov, S., & Pandelidis, D. (2014). Numerical study of the Maisotsenko cycle heat and mass exchanger. *International Journal of Heat and Mass Transfer*, 75, 75–96. <https://doi.org/10.1016/j.ijheatmasstransfer.2014.03.050>
- Anisimov, S., & Pandelidis, D. (2015). Theoretical study of the basic cycles for indirect evaporative air cooling. *International Journal of Heat and Mass Transfer*, 84, 974–989. <https://doi.org/10.1016/j.ijheatmasstransfer.2015.01.087>
- Anisimov, S., Pandelidis, D., & Danielewicz, J. (2014). Numerical analysis of selected evaporative exchangers with the Maisotsenko cycle. *Energy Conversion and Management*, 88, 426–441. <https://doi.org/10.1016/j.enconman.2014.08.055>
- ANSYS. (2013). *ANSYS Fluent Theory Guide* (November). Canonsburg, PA.
- ASHRAE. (2001). Physical Properties of Secondary Coolants (Brines). In J. Baird, S. A. Zeh, N. F. Thysell, J. E. Jackson, & W. S. Comstock (Eds.), *HVAC Fundamentals Handbook* (p. 21.6-21.7). Atlanta, GA: ASHRAE.
- ASHRAE. (2016). *2016 ASHRAE Handbook—HVAC Systems and Equipment*. (M. S. Owen, Ed.), ASHRAE. Atlanta: Comstock, W. Stephen.
- Avila, E. (2018). Concluye exitosamente el programa ahorrate una luz. *Revista Del Fideicomiso Para El Ahorro de La Energía Eléctrica*, 5–12. Retrieved from http://www.fide.org.mx/wp-content/uploads/Revistas/REE_18_ALTA.PDF

- Aydın, O., & Avcı, M. (2006). Viscous-dissipation effects on the heat transfer in a Poiseuille flow. *Applied Energy*, 83(5), 495–512. <https://doi.org/10.1016/j.apenergy.2005.03.003>
- Barbir, F., Veziroğlu, T. N., & Plass, H. J. (1990). Environmental damage due to fossil fuels use. *International Journal of Hydrogen Energy*, 15(10), 739–749. [https://doi.org/10.1016/0360-3199\(90\)90005-J](https://doi.org/10.1016/0360-3199(90)90005-J)
- Bergman, T. L., Lavine, A. S., Incropera, F. P., & DeWitt, D. P. (2011). *Fundamentals of Heat and Mass Transfer* (7th ed.). Hoboken, NJ: John Wiley & Sons, Inc.
- Bizhaem, H. K., & Abbassi, A. (2017). Numerical study on heat transfer and entropy generation of developing laminar nanofluid flow in helical tube using two-phase mixture model. *Advanced Powder Technology*, 28(9), 2110–2125. <https://doi.org/10.1016/j.appt.2017.05.018>
- BP. (2019). *BP Statistical Review of World Energy 68th edition*. British Petroleum Co. London. Retrieved from <https://www.bp.com/content/dam/bp/business-sites/en/global/corporate/pdfs/energy-economics/statistical-review/bp-stats-review-2019-full-report.pdf>
- Bretado de los Rios, M. S., Rivera-Solorio, C. I., & García-Cuellar, A. J. (2018). Thermal performance of a parabolic trough linear collector using Al₂O₃ / H₂O nanofluids. *Renewable Energy*, 122, 665–673. <https://doi.org/10.1016/j.renene.2018.01.094>
- Burke, P. J., & Csereklyei, Z. (2016). Understanding the energy-GDP elasticity: A sectoral approach. *Energy Economics*, 58, 199–210. <https://doi.org/10.1016/j.eneco.2016.07.004>
- CEPAL. (2018). *Informe Nacional de Monitoreo de la Eficiencia Energética de México 2018*. Ciudad de Mexico. Retrieved from https://www.gob.mx/cms/uploads/attachment/file/331760/S1800496_es.pdf
- Choi, S. U. S., & Eastman, J. A. (1995). Enhancing thermal conductivity of fluids with nanoparticles. *Developments and Applications of Non-Newtonian Flows, FED-2*, 99–105.
- Corcione, M. (2011). Empirical correlating equations for predicting the effective thermal conductivity and dynamic viscosity of nanofluids. *Energy Conversion and Management*, 52, 789–793. <https://doi.org/10.1016/j.enconman.2010.06.072>
- Dean, W. R. (1927). XVI. Note on the Motion of Fluid in a Curved Pipe. *Philosophical Magazine and Journal of Science*, 4(20), 208–223. <https://doi.org/10.1080/14786440708564324>
- Diekmann, A., & Franzen, A. (2019). Environmental Concern: A Global Perspective. *Einstellungen Und Verhalten in Der Empirischen Sozialforschung*, 253–272. https://doi.org/10.1007/978-3-658-16348-8_11
- Doménech, J. L., Gil-Pérez, D., Gras-Martí, A., Guisasola, J., Martínez-Torregrosa,

- J., Salinas, J., et al. (2007). Teaching of energy issues: A debate proposal for a global reorientation. *Science and Education*, 16(1), 43–64. <https://doi.org/10.1007/s11191-005-5036-3>
- Eustice, J. (1910). Flow of Water in Curved Pipes. *Proceedings of the Royal Society A*, 84(568), 107–118. <https://doi.org/https://doi.org/10.1098/rspa.1910.0061>
- Fakoor-Pakdaman, M., Akhavan-Behabadi, M. A., & Razi, P. (2013). An empirical study on the pressure drop characteristics of nano fluid flow inside helically coiled tubes. *International Journal of Thermal Sciences*, 65, 206–213. <https://doi.org/10.1016/j.ijthermalsci.2012.10.014>
- Ferziger, J. H., & Peric, M. (2002). *Computational Methods for Fluid Dynamics* (3rd ed.). Berlin: Springer.
- García, E. (1998). *Climas*. Ciudad de México. Retrieved from <http://www.conabio.gob.mx/informacion/gis/maps/geo/clima1mgw.zip>
- García, E. (2004). *Modificaciones al Sistema de Clasificación Climática de Köppen* (5th ed.). Ciudad de México: Instituto de Geografía Universidad Nacional Autónoma de México.
- Germano, M. (1982). On the effect of torsion on a helical pipe flow. *Journal of Fluid Mechanics*, 125(7), 1–8. <https://doi.org/10.1017/S0022112082003206>
- Gnielinski, V. (1986). Heat transfer and pressure drop in helically coiled tubes. *Procedures 8th International Heat Transfer Conference*, 696.
- Gnielinski, V. (2009). Heat Transfer Coefficients for Turbulent Flow in Concentric Annular Ducts. *Heat Transfer Engineering*, 30(6), 431–436. <https://doi.org/10.1080/01457630802528661>
- Goetzler, W., Zogg, R., Young, J., & Johnson, C. (2014). Alternatives to Vapor-Compression HVAC Technology. *ASHRAE Journal*, (October), 12–23.
- Goetzler, W., Guernsey, M., & Young, J. (2014). *Research & Development Roadmap for Emerging HVAC Technologies*. Burlington, MA.
- Gupta, M., Singh, V., Kumar, R., & Said, Z. (2017). A review on thermophysical properties of nano fluids and heat transfer applications. *Renewable and Sustainable Energy Reviews*, 74, 638–670. <https://doi.org/10.1016/j.rser.2017.02.073>
- Hajatzadeh-Pordanjani, A., Aghakhani, S., Afrand, M., Mahmoudi, B., Mahian, O., & Wongwises, S. (2019). An updated review on application of nanofluids in heat exchangers for saving energy. *Energy Conversion and Management*, 198(15), 111886(39). <https://doi.org/10.1016/j.enconman.2019.111886>
- Hashemi, S. M., & Akhavan-Behabadi, M. A. (2012). An empirical study on heat transfer and pressure drop characteristics of CuO - base oil nano fluid flow in a horizontal helically coiled tube under constant heat flux. *International Communications in Heat and Mass Transfer*, 39, 144–151.

<https://doi.org/10.1016/j.icheatmasstransfer.2011.09.002>

- Hassani, S., Saidur, R., Mekhilef, S., & Hepbasli, A. (2015). A new correlation for predicting the thermal conductivity of nanofluids; using dimensional analysis. *International Journal of Heat and Mass Transfer*, 90, 121–130. <https://doi.org/10.1016/j.ijheatmasstransfer.2015.06.040>
- Heymans, A., Breadsell, J., Morrison, G. M., Byrne, J. J., & Eon, C. (2019). Ecological urban planning and design: A systematic literature review. *Sustainability (Switzerland)*, 11(13). <https://doi.org/10.3390/su11133723>
- Holdren, J. P. (1991). Population and the energy problem. *Population and Environment*, 12(3), 231–255. <https://doi.org/10.1007/BF01357916>
- Huminic, G., & Huminic, A. (2011). Heat transfer characteristics in double tube helical heat exchangers using nanofluids. *International Journal of Heat and Mass Transfer*, 54, 4280–4287. <https://doi.org/10.1016/j.ijheatmasstransfer.2011.05.017>
- Huminic, G., & Huminic, A. (2016). Heat transfer and flow characteristics of conventional fluids and nanofluids in curved tubes: A review. *Renewable and Sustainable Energy Reviews*, 58, 1327–1347. <https://doi.org/10.1016/j.rser.2015.12.230>
- IEI. (2012). *Recomendación estratégica sobre tecnologías y subsectores como orientación para sustentar acciones de eficiencia energética en el sector PyME. Programa de Energía Sustentable en México*. Mexico. Retrieved from https://energypedia.info/images/7/72/Recomendación_estratégica_eficiencia_energética_PyME_2012.pdf
- Jamshidi, N., Farhadi, M., Sedighi, K., & Ganji, D. D. (2012). Optimization of design parameters for nano fluids flowing inside helical coils ☆. *International Communications in Heat and Mass Transfer*, 39, 311–317. <https://doi.org/10.1016/j.icheatmasstransfer.2011.11.013>
- Jayakumar, J. S., Mahajani, S. M., Mandal, J. C., Vijayan, P. K., & Bhoi, R. (2008). Experimental and CFD estimation of heat transfer in helically coiled heat exchangers. *Chemical Engineering Research and Design*, 86(3), 221–232. <https://doi.org/10.1016/j.cherd.2007.10.021>
- Jayakumar, J. S., Mahajani, S. M., Mandal, J. C., Iyer, K. N., & Vijayan, P. K. (2010). CFD analysis of single-phase flows inside helically coiled tubes. *Computers and Chemical Engineering*, 34(4), 430–446. <https://doi.org/10.1016/j.compchemeng.2009.11.008>
- Kahani, M., Heris, S. Z., & Mousavi, S. M. (2013a). Comparative study between metal oxide nanopowders on thermal characteristics of nanofluid flow through helical coils. *Powder Technology*, 246, 82–92. <https://doi.org/10.1016/j.powtec.2013.05.010>
- Kahani, M., Heris, S. Z., & Mousavi, S. M. (2013b). Effects of Curvature Ratio and

- Coil Pitch Spacing on Heat Transfer Performance of Al₂O₃ / Water Nanofluid Laminar Flow through Helical Coils Effects of Curvature Ratio and Coil Pitch Spacing on Heat Transfer. *Journal of Dispersion Science and Technology*, 34(12), 1704–17012. <https://doi.org/10.1080/01932691.2013.764485>
- Kahani, M., Heris, S. Z., & Mousavi, S. M. (2013c). Multiwalled Carbon Nanotube / Water Nanofluid or Helical Coiling Technique, Which of Them Is More Effective ? *Industrial & Engineering Chemistry Research*, 52, 13183–13191. <https://doi.org/10.1021/ie4010942>
- Kannadasan, N., Ramanathan, K., & Suresh, S. (2012). Comparison of heat transfer and pressure drop in horizontal and vertical helically coiled heat exchanger with CuO / water based nano fluids. *Experimental Thermal and Fluid Science*, 42, 64–70. <https://doi.org/10.1016/j.expthermflusci.2012.03.031>
- Khairul, M. A., Saidur, R., Rahman, M. M., Alim, M. A., Hossain, A., & Abdin, Z. (2013). Heat transfer and thermodynamic analyses of a helically coiled heat exchanger using different types of nanofluids. *International Journal of Heat and Mass Transfer*, 67, 398–403. <https://doi.org/10.1016/j.ijheatmasstransfer.2013.08.030>
- Kim, D., Kwon, Y., Cho, Y., Li, C., Cheong, S., Hwang, Y., et al. (2009). Convective heat transfer characteristics of nanofluids under laminar and turbulent flow conditions. *Current Applied Physics*, 9(2), 119–123. <https://doi.org/10.1016/j.cap.2008.12.047>
- Kreider, J. F., Curtiss, P. S., & Rabl, A. (2010). *Heating and Cooling of Buildings: Design for Efficiency*. (F. Kreith & R. Mahajan, Eds.) (2nd ed.). Boca Raton, FL: CRC Press.
- Lee, J., & Lee, D.-Y. (2013). Experimental study of a counter flow regenerative evaporative cooler with finned channels. *International Journal of Heat and Mass Transfer*, 65, 173–179. <https://doi.org/10.1016/j.ijheatmasstransfer.2013.05.069>
- Lee, J., Choi, B., & Lee, D. Y. (2013). Comparison of configurations for a compact regenerative evaporative cooler. *International Journal of Heat and Mass Transfer*, 65, 173–179. <https://doi.org/10.1016/j.ijheatmasstransfer.2013.05.069>
- Lepure, A. (2018). Comparativo de eficiencia energética de sistemas de aire acondicionado. *Boletín de Eficiencia Energética*, (03), 10. Retrieved from https://www.gob.mx/cms/uploads/attachment/file/346457/Bolet_n_03_EE_Aire_Acondicionado.pdf
- Lin, J., Thu, K., Bui, T. D., Wang, R., Ng, K. C., & Chua, K. J. (2016). Study on dew point evaporative cooling system with counter-flow configuration. *Energy Conversion and Management*, 109, 153–165. <https://doi.org/10.1016/j.enconman.2015.11.059>
- Liu, Y., Li, J. M., Yang, X., & Zhao, X. (2019). Two-dimensional Numerical study of

- a Heat and Mass Exchanger for a Dew-point Evaporative Cooler. *Energy*, 168, 975–988. <https://doi.org/10.1016/j.energy.2018.11.135>
- Lu, Y., Wang, H., Wang, Q., Zhang, Y., Yu, Y., & Qian, Y. (2017). Global anthropogenic heat emissions from energy consumption, 1965–2100. *Climatic Change*, 145(3–4), 459–468. <https://doi.org/10.1007/s10584-017-2092-z>
- MacLaine-cross, I. L., & Banks, P. J. (1981). A General Theory of Wet Surface Heat Exchangers and its Application to Regenerative Evaporative Cooling. *Journal of Heat Transfer*, 103(3), 579. <https://doi.org/10.1115/1.3244505>
- Mahmood, M. H., Sultan, M., Miyazaki, T., Koyama, S., & Maisotsenko, V. S. (2016). Overview of the Maisotsenko cycle – A way towards dew point evaporative cooling. *Renewable and Sustainable Energy Reviews*, 66, 537–555. <https://doi.org/10.1016/j.rser.2016.08.022>
- Mahmoudi, M., Tavakoli, M. R., Mirsoleimani, M. A., Gholami, A., & Salimpour, M. R. (2017). Experimental and numerical investigation on forced convection heat transfer and pressure drop in helically coiled pipes using TiO₂/water nanofluid. *International Journal of Refrigeration*, 74, 627–643. <https://doi.org/10.1016/j.ijrefrig.2016.11.014>
- Massman, W. J. (1998). A review of the molecular diffusivities of H₂O, CO₂, CH₄, CO, O₃, SO₂, NH₃, N₂O, NO, and NO₂ in air, O₂ and N₂ near STP. *Atmospheric Environment*, 32(6), 1111–1127. [https://doi.org/10.1016/S1352-2310\(97\)00391-9](https://doi.org/10.1016/S1352-2310(97)00391-9)
- Menni, Y., Chamkha, A. J., Lorenzini, G., Kaid, N., Ameer, H., & Bensafi, M. (2019). Advances of Nanofluids in Solar Collectors - A Review of Numerical Studies. *Mathematical Modelling of Engineering Problems*, 6(3), 415–427. <https://doi.org/https://doi.org/10.18280/mmep.060313>
- Miller, J. G. (1975). The nature of living systems. *Behavioral Science*, 20(6), 343–365. <https://doi.org/10.1002/bs.3830200602>
- Mir M, A., & Aksamija, A. (2008). Toward a Better Urban Life: Integration of Cities and Tall Buildings. *The 4th Architectural Conference on High Rise Buildings, 9-11 June 2008, Amman – Jordan*, 11.
- Mishra, P., & Gupta, S. N. (1979). Momentum Transfer in Curved Pipes. 1. Newtonian Fluids. *Industrial & Engineering Chemistry Process Design and Development*, 18(1), 130–137. <https://doi.org/https://doi.org/10.1021/i260069a017>
- Mohammed, H. A., & Narrein, K. (2012). Thermal and hydraulic characteristics of nanofluid flow in a helically coiled tube heat exchanger. *International Communications in Heat and Mass Transfer*, 39, 1375–1383. <https://doi.org/10.1016/j.icheatmasstransfer.2012.07.019>
- Mokmeli, A., & Saffar-Avval, M. (2010). Prediction of nanofluid convective heat transfer using the dispersion model. *International Journal of Thermal Sciences*,

49(3), 471–478. <https://doi.org/10.1016/j.ijthermalsci.2009.09.005>

Mukesh Kumar, P. C., & Chandrasekar, M. (2019). CFD analysis on heat and flow characteristics of double helically coiled tube heat exchanger handling MWCNT/water nanofluids. *Heliyon*, 5(7), e02030. <https://doi.org/10.1016/j.heliyon.2019.e02030>

MultiTherm. (2018). *MultiTherm IG-4*. Devault, PA. Retrieved from https://www.multitherm.com/pdf/IG_4.PDF

Murshed, S. M. S. (2011). Determination of effective specific heat of nanofluids. *Journal of Experimental Nanoscience*, 6(5), 539–546. <https://doi.org/10.1080/17458080.2010.498838>

Narrein, K., & Mohammed, H. A. (2013). Influence of nanofluids and rotation on helically coiled tube heat exchanger performance. *Thermochimica Acta*, 564, 13–23.

Pakari, A., & Ghani, S. (2019). Comparison of 1D and 3D heat and mass transfer models of a counter flow dew point evaporative cooling system: Numerical and experimental study. *International Journal of Refrigeration*, 99, 114–125. <https://doi.org/10.1016/j.ijrefrig.2019.01.013>

Pakdaman, M. F., Akhavan-behabadi, M. A., & Razi, P. (2012). An experimental investigation on thermo-physical properties and overall performance of MWCNT / heat transfer oil nanofluid flow inside vertical helically coiled tubes. *Experimental Thermal and Fluid Science*, 40, 103–111. <https://doi.org/10.1016/j.expthermflusci.2012.02.005>

Pandelidis, D., & Anisimov, S. (2015). Numerical analysis of the heat and mass transfer processes in selected M-Cycle heat exchangers for the dew point evaporative cooling. *Energy Conversion and Management*, 90, 62–83. <https://doi.org/10.1016/j.enconman.2014.11.008>

Pandelidis, D., & Anisimov, S. (2016a). Application of a statistical design for analyzing basic performance characteristics of the cross-flow Maisotsenko cycle heat exchanger. *International Journal of Heat and Mass Transfer*, 95, 45–61. <https://doi.org/10.1016/j.ijheatmasstransfer.2015.11.060>

Pandelidis, D., & Anisimov, S. (2016b). Numerical study and optimization of the cross-flow Maisotsenko cycle indirect evaporative air cooler. *International Journal of Heat and Mass Transfer*, 103, 1029–1041. <https://doi.org/10.1016/j.ijheatmasstransfer.2016.08.014>

Pandelidis, D., Anisimov, S., Worek, W. M., & Drag, P. (2016). Numerical analysis of a desiccant system with cross-flow Maisotsenko cycle heat and mass exchanger. *Energy and Buildings*, 123, 136–150. <https://doi.org/10.1016/j.enbuild.2016.04.039>

Patel, H. E., Sundararajan, T., & Das, S. K. (2010). An experimental investigation into the thermal conductivity enhancement in oxide and metallic nanofluids.

- Journal of Nanoparticle Research*, 12, 1015–1031.
<https://doi.org/10.1007/s11051-009-9658-2>
- Pawar, S. S., & Sunnapwar, V. K. (2013). Experimental studies on heat transfer to Newtonian and non-Newtonian fluids in helical coils with laminar and turbulent flow. *Experimental Thermal and Fluid Science*, 44, 792–804.
<https://doi.org/10.1016/j.expthermflusci.2012.09.024>
- Pawar, S. S., & Sunnapwar, V. K. (2014). Experimental and CFD investigation of convective heat transfer in helically coiled tube heat exchanger. *Chemical Engineering Research and Design*, 92(11), 2294–2312.
<https://doi.org/10.1016/j.cherd.2014.01.016>
- Picard, A., Davis, R. S., Gläser, M., & Fujii, K. (2008). Revised formula for the density of moist air (CIPM-2007). *Metrologia*, 45(2), 149–155.
<https://doi.org/10.1088/0026-1394/45/2/004>
- Porumb, B., Ungureșan, P., Tutunaru, L. F., Șerban, A., & Bălan, M. (2016). A Review of Indirect Evaporative Cooling Technology. *Energy Procedia*, 85(November 2015), 461–471. <https://doi.org/10.1016/j.egypro.2015.12.228>
- Rakhsha, M., Akbaridoust, F., Abbassi, A., & Majid, S.-A. (2015). Experimental and numerical investigations of turbulent forced convection flow of nano-fluid in helical coiled tubes at constant surface temperature. *Powder Technology*, 283, 178–189. <https://doi.org/10.1016/j.powtec.2015.05.019>
- Rey-Martinez, F. J., Velasco-Gomez, E., Herrero-Martin, R., Martinez-Gutierrez, J., & Varela-Diez, F. (2004). Comparative study of two different evaporative systems: an indirect evaporative cooler and a semi-indirect ceramic evaporative cooler. *Energy and Buildings*, 36, 696–708.
<https://doi.org/10.1016/j.enbuild.2003.10.010>
- Reynolds, O. (1883). An Experimental Investigation of the Circumstances which Determine whether the Motion of Water shall be Direct or Sinuous, and of the Law of Resistance in Parallel Channels. *Proceedings of the Royal Society A*, 35(224–226), 84–99. <https://doi.org/https://doi.org/10.1098/rspl.1883.0018>
- Riangvilaikul, B., & Kumar, S. (2010a). An experimental study of a novel dew point evaporative cooling system. *Energy and Buildings*, 42(5), 637–644.
<https://doi.org/10.1016/j.enbuild.2009.10.034>
- Riangvilaikul, B., & Kumar, S. (2010b). Numerical study of a novel dew point evaporative cooling system. *Energy and Buildings*, 42(11), 2241–2250.
<https://doi.org/10.1016/j.enbuild.2010.07.020>
- Ruiz-Mirazo, K., Peretó, J., & Moreno, A. (2010). A universal definition of life: Autonomy and open-ended evolution. *The Nature of Life: Classical and Contemporary Perspectives from Philosophy and Science*, 310–325.
<https://doi.org/10.1017/CBO9780511730191.031>
- Sadighi-Dizaji, H., Hu, E. J., & Chen, L. (2018). A comprehensive review of the

- Maisotsenko-cycle based air conditioning systems. *Energy*, 156, 725–749. <https://doi.org/10.1016/j.energy.2018.05.086>
- SENER. (2018). *Balance Nacional de Energía 2018*. Secretaría de Energía. Mexico.
- SENER. (2020). Sistema de Información Energética. Retrieved from <http://sie.energia.gob.mx/>
- Srinivas, T., & Vinod, A. V. (2016). Heat transfer intensification in a shell and helical coil heat exchanger using water-based nanofluids. *Chemical Engineering & Processing: Process Intensification*, 102, 1–8. <https://doi.org/10.1016/j.cep.2016.01.005>
- Tsililingiris, P. T. (2008). Thermophysical and transport properties of humid air at temperature range between 0 and 100 ° C, 49, 1098–1110. <https://doi.org/10.1016/j.enconman.2007.09.015>
- UN Environment and International Energy Agency. (2017). *Towards a zero-emission, efficient, and resilient buildings and construction sector* (Global Sta). United Nations.
- Vajjha, R. S., & Das, D. K. (2009). Experimental determination of thermal conductivity of three nanofluids and development of new correlations. *International Journal of Heat and Mass Transfer*, 52(21–22), 4675–4682. <https://doi.org/10.1016/j.ijheatmasstransfer.2009.06.027>
- Vakiloroaya, V., Samali, B., Fakhar, A., & Pishghadam, K. (2014). A review of different strategies for HVAC energy saving. *Energy Conversion and Management*, 77, 738–754. <https://doi.org/10.1016/j.enconman.2013.10.023>
- Wang, C. Y. (1981). On the low-Reynolds-number flow in a helical pipe. *Journal of Fluid Mechanics*, 108(July), 185–194. <https://doi.org/https://doi.org/10.1017/S0022112081002073>
- Wang, X.-Q., & Mujumdar, A. S. (2008). A review on nanofluids - part I: theoretical and numerical investigations. *Brazilian Journal of Chemical Engineering*, 25(4), 613–630. <https://doi.org/10.1590/S0104-66322008000400001>
- Williams, G. S., Fenkell, G. H., & Hubbell, C. W. (1902). *Experiments at Detroit, Mich.: on the effect of curvature upon the flow of water in pipes*. New York: American Society of Civil Engineers. Retrieved from <https://catalog.hathitrust.org/Record/006559558>
- Wu, Z., Wang, L., & Sundén, B. (2013). Pressure drop and convective heat transfer of water and nanofluids in a double-pipe helical heat exchanger. *Applied Thermal Engineering*, 60, 266–274. <https://doi.org/10.1016/j.applthermaleng.2013.06.051>
- Zhan, C., Duan, Z., Zhao, X., Smith, S., Jin, H., & Riffat, S. (2011). Comparative study of the performance of the M-cycle counter-flow and cross-flow heat exchangers for indirect evaporative cooling - Paving the path toward sustainable cooling of buildings. *Energy*, 36(12), 6790–6805.

<https://doi.org/10.1016/j.energy.2011.10.019>

Zonouzi, S. A., Aminfar, H., & Mohammadpourfard, M. (2014). 3D Numerical Investigation of Thermal Characteristics of Nanofluid Flow through Helical Tubes Using Two- Phase Mixture Model. *International Journal for Computational Methods in Engineering Science and Mechanics*, 15, 512–521. <https://doi.org/10.1080/15502287.2014.952847>

Curriculum Vitae

Enrique Mitz Hernández was born in Ciudad de México, México, on November 16th, 1992. He earned the Renewable Energy Engineering degree from the *Universidad Autónoma de Yucatán*, in September 2016. He was accepted in the graduate programs in Energetic Engineering in August 2018.

This document was typed in using Microsoft Word by Enrique Mitz Hernández